On Acoustic Emission Condition Monitoring of Highly-loaded Low-speed Roller Bearings

- ON -
ACOUSTIC EMISSION CONDITION MONITORING
— OF —
HIGHLY-LOADED LOW-SPEED ROLLER BEARINGS

BART SCHEEREN

ON ACOUSTIC EMISSION CONDITION MONITORING OF HIGHLY-LOADED LOW-SPEED ROLLER BEARINGS

PROEFSCHRIFT

TER VERKRIJGING VAN DE GRAAD VAN DOCTOR AAN DE
TECHNISCHE UNIVERSITEIT DELFT,
OP GEZAG VAN DE RECTOR MAGNIFICUS
PROF.DR.IR. T.H.J.J. VAN DER HAGEN,
VOORZITTER VAN HET COLLEGE VOOR PROMOTIES,
IN HET OPENBAAR TE VERDEDIGEN OP
DONDERDAG, 15 JUNI 2023 OM 12:30 UUR

DOOR

Bart SCHEEREN

SCHEEPSBOUWKUNDIG INGENIEUR
TECHNISCHE UNIVERSITEIT DELFT, NEDERLAND
GEBOREN TE WIJCHEN, NEDERLAND

Dit proefschrift is goedgekeurd door de promotoren.

Samenstelling promotiecommissie bestaat uit:

voorzitter: Rector Magnificus
promotor: prof.em.dr.ir. M.L. Kaminski
copromotor: dr.   L. Pahlavan

onafhankelijke leden:

prof.dr.	D. Ozevin	University of Illinois Chicago
prof.dr.	Z. Sharif Khodaei	Imperial College London
prof.dr.	C. Kassapoglou	Technische Universiteit Delft
prof.dr.	Z. Li	Technische Universiteit Delft
prof.dr.	M.J. Santofimia Navarro	Technische Universiteit Delft

- ON -

ACOUSTIC EMISSION CONDITION MONITORING

— OF —

HIGHLY-LOADED LOW-SPEED ROLLER BEARINGS

BART

SCHEEREN

Εἰσιέναι εἰς τὸ ἡγεμονικὸν ἑκάστου, παρέχειν δὲ καὶ
ἑτέρῳ παντὶ εἰσιέναι εἰς τὸ ἑαυτοῦ ἡγεμονικόν.

To enter others' minds and let them enter yours.

from Meditations by Marcus Aurelius
as translated by Gregory Hays

SUMMARY

Highly-loaded low-speed roller bearings form crucial connections in offshore struc-tures, such as heavy-lifting vessels, single-point mooring systems, and wind turbines. In order to safeguard the integrity and reliability of these assets and their operations, a quantitative methodology for condition monitoring of the bearings can be of substantial value. To date, a number of assessment methods have been proposed to for this purpose, e.g. based on strain, vibration, lubrication, and acoustic emission (AE) monitoring. Despite their demonstrated potential for medium- and high-speed bearings (>600 rpm), no notable success has yet been reported in the assessment of low-speed bearings subjected to naturally-developing degradation. In this disser-tation, a novel methodology for the analysis of damage-induced AE and inferring the bearing condition has been proposed. Acoustic emissions in this context are ultrasonic signals generated by the release of elastic energy in a material. In solid media, these signals propagate as stress waves and can be recorded by dedicated transducers.

A mathematical framework to describe the generation, propagation, transmis-sion, and detection of transient ultrasonic waves in complex geometries has been presented. An assessment of inter-component stress-wave transmission has been performed utilising this framework. For a representative sheave bearing, results indicate that a transmission loss in the order of 15 dB is to be expected in the amp-litude of the AE waves for a single rolling contact arrangement. In conjunction with a preliminary field trial regarding the ultrasonic background noise in representative operational conditions, this evaluation has shown that it is feasible to detect damage initiated AE signals from each of the rolling elements upon field implementations.

A waveform-similarity based clustering algorithm has been proposed for the identification of damage-induced AE source mechanisms. Consistency in the source mechanism is theorised to indicate gradual progressive failure, such as crack growth. Through the descriptive framework, it has been shown that high similarity of the recorded signal must be the result of high similarity in the emitted source. Additional numerical verification of this assumptions on transfer path similarity has been performed, confirming the equivalence derived from the descriptive framework.

A low-speed run-to-failure test was performed with a purpose-built linear bearing segment, representative of the main bearing of a mooring turret, to assess the performance of the clustering algorithm. Intermediate and final visual inspections report the development of wear comprising erosion, surface roughening, pitting and surface initiated fatigue. In independent analysis of the recorded AE signals, several highly-consistent structures of clusters were identified over multiple measurement channels. The nose raceway could be identified as the source of these structures

of clusters, which matched the observed evolution of localised damage during the inspections.

Based on the source-identified AE activity, a novel quantitative indicator has been proposed to infer bearing condition. The bearing condition index (BCI) adopts a value of 1 when the bearing is in good condition. The BCI drops in value as the bearing degrades, as represented by a more significant detection of clusters of similar AE signals within the normalised period of a load cycle over a multitude of measurement frequencies.

Run-to-failure experiments have been conducted to assess the proposed BCI. Intermediate and final inspections report the progressive erosion and surface roughening. Additional lubrication samples collected during these inspections contained high levels of particle contamination. A direct correlation between the AE hit-rate and the particle contamination of the lubricant was observed. Utilising progressive scaling based on cluster size, the excessive influence of lubrication contamination-induced AE signals on the BCI could be reduced, while still providing a timely warning.

In review, it is concluded that the proposed methodology can effectively describe the complex generation and propagation of AE due to damage evolution in highly-loaded low-speed roller bearings. The developed clustering method has shown to effectively identify patterns and trends in the AE signals at different stages of degradation, and provide the basis for filtering out noise-related signals. The formulated BCI can subsequently provide an intuitive indication of the condition of a low-speed roller bearing in an in-situ non-intrusive manner. As such, the methodology is believed to offer promising potential to contribute to the safe and continued operation of the offshore energy infrastructure.

SAMENVATTING

Hoogbelaste langzaamdraaiende rollagers vormen cruciale verbindingen in afland-
ige constructies, zoals zware-last kraanschepen, enkelpunts-afmeersystemen, en
windturbines. Om de integriteit en betrouwbaarheid van deze objecten en hun
werkzaamheden te waarborgen, kan een kwantitatieve methodologie om de conditie
van deze lagers te bewaken van aanzienlijke waarde zijn. Tot op heden zijn verschil-
lende beoordelingsmethoden voorgesteld voor dit doel, bijvoorbeeld gebaseerd op
het bewaken belasting, trilling, smering en akoestische emissie (AE). Ondanks hun
aangetoonde potentieel voor gemiddeld- en sneldraaiende lagers (>600 rpm), is er
nog geen noemenswaardig succes gerapporteerd voor de beoordeling van langzaam-
draaiende lagers die onderhevig zijn aan natuurlijke degradatie. In dit proefschrift
is een nieuwe methodologie voor de analyse van door schade veroorzaakte AE en
het afleiden van de conditie van het lager voorgesteld. In deze context zijn akoes-
tische emissies ultrasone signalen die worden gegenereerd door het vrijkomen van
elastische energie in een materiaal. In vaste stoffen planten deze signalen zich voort
als spanningsgolven en kunnen zij worden opgevangen door speciale opnemers.

Een wiskundig kader om de opwekking, voortplanting, transmissie, en detectie
van lopende ultrasone golven in complexe geometrieën te beschrijven is gepresent-
eerd. Gebruikmakend van dit kader is een beschouwing van spanningsgolftrans-
missie tussen componenten uitgevoerd. Voor representatieve schijflagers wijzen de
resultaten erop dat een transmissieverlies in de orde van 15 dB te verwachten is
in de amplitude van de AE golven in een opstelling met een enkelvoudig rollend
contact. In samenhang met een inleidende veldproef aangaande de ultrasone achter-
grondruis in representatieve operationele omstandigheden, heeft deze beschouwing
aangetoond dat het haalbaar is om door schade opgewekte AE signalen uit elk van
de rollende elementen te detecteren bij toepassing in het veld.

Een algoritme voor clustervorming gebaseerd op golfvormgelijkenis is voorgesteld
om door schade opgewerkte AE bronmechanismen te identificeren. De consistentie
van het bronmechanisme wordt verondersteld te wijzen op geleidelijk toenemende
schade, zoals scheurgroei. Met behulp van het beschrijvende kader is er aangetoond
dat hoge gelijkenis van de opgenomen signalen het gevolg moet zijn van hoge
gelijkenis in de uitgezonden bron. Aanvullende numerieke verificaties van deze
aannames over de gelijkenis van het overdrachtspad zijn uitgevoerd, welke de uit
het beschrijvende kader afgeleide gelijkwaardigheid bevestigen.

Een duurtest tot falen is uitgevoerd op lage snelheid met een voor deze toepassing
gemaakt rechtvormig lagersegment, representatief voor het hoofdlager van een
afmeertoren, om de prestaties van het clustervormingsalgoritme te beoordelen. Bij
visuele inspecties, zowel tussentijds als achteraf, zijn de ontwikkeling van slijtage

waargenomen, bestaande uit erosie, toename van oppervlakteruwheid, putvorming, en vermoeiing van het oppervlak. Bij onafhankelijke analyse van de opgenomen AE-signalen zijn enkele sterk overeenkomende structuren van clusters geïdentificeerd over meerdere meetkanalen. De dynamische loopbaan van het lager kon worden geïdentificeerd als de bron van deze structuren van clusters, welke verband houden met de waargenomen toename van plaatselijke schade tijdens de inspecties.

Op basis van de AE activiteit waarvan de bron geïdentificeerd is, is een nieuwe kwantitatieve indicator voorgesteld om de staat van het lager uit af te leiden. De lagerconditie-index (BCI) neemt de waarde 1 aan als het lager in goede staat verkeert. De BCI daalt in waarde naarmate het lager degradeert, wat wordt weerspiegeld in een aanzienlijkere waarneming van groepen van gelijkende AE signalen binnen de genormaliseerde periode van een belastingcyclus over een veelheid van meetfrequenties.

Duurtesten tot falen zijn uitgevoerd om de voorgestelde BCI te beoordelen. Bij tussentijdse en eindinspecties werden toenemende erosie en oppervlakteruwheid waargenomen. Aanvullende smeermonsters die tijdens deze inspecties werden verzameld, bevatten hoge niveaus van deeltjesverontreiniging. Een direct verband tussen het AE-detectietempo en deeltjesverontreiniging van het smeermiddel is waargenomen. Door gebruik te maken van progressieve schaling op basis van clusteromvang kon de overmatige invloed van AE-signalen veroorzaakt door smeermiddelverontreiniging op de BCI worden verminderd, terwijl nog steeds tijdige waarschuwingen werden gegeven.

Resumerend wordt geconcludeerd dat de voorgestelde methodologie de complexe generatie en voortplanting van AE als gevolg van schade-ontwikkeling in hoogbelaste traagdraaiende lagers effectief kan beschrijven. De ontwikkelde clusteringmethode heeft aangetoond dat het patronen en tendensen in de AE-signalen effectief kan identificeren tijdens verschillende degradatiestadia en de basis kan vormen voor het filteren van signalen gerelateerd aan ruis. De geformuleerde BCI kan vervolgens op een intuïtieve manier een indicatie geven van de conditie van een traagdraaiend lager op locatie zonder ingreep. Hierdoor wordt verwacht dat de methode een veelbelovend potentieel biedt om bij te dragen aan de veilige en voortdurende werking van de aflandige energie-infrastructuur.

CONTENTS

LIST OF FIGURES

LIST OF TABLES

LATIN

$\hat{A}_R$	relative amplitude
$a_{\beta,\gamma}$	Morse wavelet normalising constant
C_B	bearing condition index (BCI)
C_{min}	target minimum cluster size
c	number of signals in cluster
$c_{k,q}$	number of source identified AE signals
D_R	degradation rate index (DRI)
$\hat{D}_A$	coupling transfer function of receiver on support substructure
$\hat{D}_B$	coupling transfer function of receiver on nose substructure
$\hat{D}_I$	coupling transfer function of receiver on inner raceway
$\hat{D}_L$	coupling transfer function of receiver on nose raceway
$\hat{D}_O$	coupling transfer function of receiver on outer raceway
$\hat{D}_U$	coupling transfer function of receiver on support raceway
d_C	roller clearance distance
d_R	roller diameter
e	Euler's number
F	force applied through bearing
K	number of source mechanisms
k	source mechanism index
N	load cycles
n	bearing rotations
$\hat{P}_i, \hat{P}_j$	recorded response (generic representations)
$\hat{P}_{AC}$	recorded response on support substructure from roller-raceway contact interface source
$\hat{P}_{AL}$	recorded response on support substructure from nose raceway source
$\hat{P}_{AR}$	recorded response on support substructure from roller source
$\hat{P}_{BC}$	recorded response on nose substructure from roller-raceway contact interface source
$\hat{P}_{BL}$	recorded response on nose substructure from nose raceway source
$\hat{P}_{BR}$	recorded response on nose substructure from roller source

$\hat{P}_{II}$	recorded response on inner raceway from inner raceway source
$\hat{P}_{LC}$	recorded response on nose raceway from roller-raceway contact interface source
$\hat{P}_{LL}$	recorded response on nose raceway from nose raceway source
$\hat{P}_{LR}$	recorded response on nose raceway from roller source
$\hat{P}_{N}$	neglected paths, mode conversions, scattering, and background noise
$\hat{P}_{UC}$	recorded response on support raceway from roller-raceway contact interface source
$\hat{P}_{OI}$	recorded response on outer raceway from inner raceway source
$\hat{P}_{UL}$	recorded response on support raceway from nose raceway source
$\hat{P}_{UR}$	recorded response on support raceway from roller source
p_i, p_j	recorded waveform (generic representations)
Q	number of sensor types
q	sensor type index
r_I	inner raceway radius
r_O	outer raceway radius
$\hat{S}_i, \hat{S}_j$	source function (generic representations)
$\hat{S}_C$	source function on roller-raceway contact interface
$\hat{S}_I$	source function on inner raceway
$\hat{S}_L$	source function on nose raceway
$\hat{S}_R$	source function on roller
s	wavelet scale
s_i, s_j	source signal (generic representations)
$\mathbf{s}_{CI}$	location of inner raceway-roller contact
$\mathbf{s}_{CO}$	location of outer raceway-roller contact
$\mathbf{s}_{D}$	location of receiver (generic representation)
$\mathbf{s}_{DA}$	location of support substructure receiver
$\mathbf{s}_{DB}$	location of nose substructure receiver
$\mathbf{s}_{DI}$	location of inner raceway receiver
$\mathbf{s}_{DL}$	location of nose raceway receiver
$\mathbf{s}_{DO}$	location of outer raceway receiver
$\mathbf{s}_{DU}$	location of support raceway receiver
$\mathbf{s}_{S}$	location of source (generic representation)
$\mathbf{s}_{SC}$	location of source at contact interface
$\mathbf{s}_{SI}$	location of inner raceway source
$\mathbf{s}_{SL}$	location of source at nose raceway
$\mathbf{s}_{SR}$	location of source at roller
$\hat{T}_{IL}$	interface transmission function for contact interface source to nose raceway

$\hat{T}_{IR}$	interface transmission function between inner raceway and roller
$\hat{T}_{IR}$	interface transmission function for contact interface source to roller
$\hat{T}_{LB}$	interface transmission function between nose raceway and nose substructure
$\hat{T}_{LR}$	interface transmission function between nose raceway and roller
$\hat{T}_{RL}$	interface transmission function between roller and nose raceway
$\hat{T}_{RO}$	interface transmission function between roller and outer raceway
$\hat{T}_{RU}$	interface transmission function between roller and support raceway
$\hat{T}_{UA}$	interface transmission function between support raceway and support substructure
t	time
t_τ	time (time-frequency domain)
$\hat{W}_A$	propagation function of support substructure
$\hat{W}_B$	propagation function of nose substructure
$\hat{W}_I$	propagation function of inner raceway
$\hat{W}_L$	propagation function of nose raceway
$\hat{W}_O$	propagation function of outer raceway
$\hat{W}_R$	propagation function of roller
$\hat{W}_U$	propagation function of support raceway
w_i	dissimilarity weight factor for signal i
w_ψ	wavelet transform (generic representation)
x	generic signal
$\hat{Z}_i, \hat{Z}_j$	consolidated propagation, transmission and coupling function (generic representations)

GREEK

α_k	source mechanism scaling
$\alpha_{k,\infty}$	target source mechanism scaling for fully developed cluster
$\alpha_{k,GL}$	generalised logistic function for source mechanism scaling
α_q	sensor type scaling
β	wavelet order
Γ_{LB}	interface boundary between nose raceway and nose substructure
Γ_{LR}	interface boundary between nose raceway and roller
Γ_{UA}	interface boundary between support raceway and support substructure
Γ_{UR}	interface boundary between support raceway and roller
γ	wavelet family
$\delta_{i,j}$	dissimilarity between signals i and j
δ_j^c	dissimilarity between signal j and cluster c
$\varsigma_{i,j}$	similarity between signals i and j

τ	time shift
ϕ_R	load pass arc length
$\hat{\Psi}_{\beta,\gamma}$	Morse wavelet in frequency domain
ψ	wavelet function in time domain (generic representation)
$\psi_{\beta,\gamma}$	Morse wavelet in time domain
ω	frequency
ω_s	scale frequency (time-frequency domain)
$\omega_{\beta,\gamma}$	Morse wavelet peak frequency

ACRONYMS

AE	Acoustic Emission
AHC	Agglomerative Hierarchical Clustering
ASTM	American Society for Testing and Materials
BCI	Bearing Condition Index
DRI	Degradation Rate Index
FPSO	Floating Production Storage and Offloading
HiTeAM	High Tech Acoustic Monitoring
ISO	International Organization for Standardization
JIP	Joint Industry Programme
PTFE	Polytetrafluoroethylene
RVM	Relevance Vector Machine
SEM	Spectral Element Method
SNR	Signal-to-noise Ratio
SVM	Support Vector Machine
TKI	Top consortium for Knowledge and Innovation
WPI	Wear Particle Index

INTRODUCTION

The integrity of highly-loaded low-speed roller bearings is essential to the safe and continued operation of the offshore energy infrastructure and its associated activities. Notable applications of these bearings include slew bearings of heavy-lifting cranes (Figure 1.1a), turntables in single-point mooring systems (Figure 1.1b), and nacelle-slew or blade-pitch bearings in wind turbines, and as such comprise both installations for the oil and gas and renewables industry, as well as equipment supporting the energy transition. In these offshore applications, bearings are subjected to an unpredictable interaction of operational and motion-induced loading while also suffering from the harsh seawater environment. This combination of high loads and intermittent movement are generally unfavourable operational conditions from the perspective of lubrication, as they may lead to a reduced or broken lubrication

Figure 1.1: Typical examples of highly-loaded low-speed roller bearings in the offshore industry; (a) the offshore mast crane on deepwater construction vessel "Aegir" containing a slew bearing to yaw the boom and sheave bearings to guide the hoisting wire ropes, and (b) the single point mooring turret of "Aoka Mizu" FPSO containing a toothless slew bearing to allow for rotation of the vessel around the seafloor-fixed mooring chains. Courtesy of (a) Heerema Marine Contractors, and (b) Bluewater Energy Services.

film, which has a significant impact on wear. Since these structures are held to the highest standards of safety and reliability, due to the remote nature of the offshore environment, assurance of the integrity of those critical roller bearings is of special concern. Manufacturers' standards prescribe regular inspections, typically on a yearly basis or every few thousands running hours. Though only a limited range of methods are defined to perform said inspections [1], [2]. For slew bearings for example, these are lubrication sampling and analysis, tilting clearance measurement, and visual inspection through endoscopy. For other bearings, these methods may be expanded to full internal inspection, that requires disassembly of bearing in part or in full. Other than in-line grease analysis, no monitoring methods are currently recommended for low-speed roller bearings. In order to assure the integrity of these large-scale low-speed roller bearings, more robust methodologies for their condition monitoring are required.

1.1 FAILURE MODES IN BEARINGS

Development of wear in rolling element bearings is a complex process of multiple interconnected degradation mechanisms [3]. These may generally be grouped into fatigue cracking, adhesive wear, and abrasive wear. Rolling elements that are starved of lubrication, either due to improper maintenance or unfavourable operation, operate in a regime of high friction, and are thus particularly susceptible to adhesive wear. The resulting surface degradation induces stress concentrations, which could lead to pitting and micro-cracking. In contrast, sufficient lubrication provides a regime of low friction, which under repeated loading inevitably leads to subsurface crack initiation and the eventual development of spalls. In particular case-hardened raceways are susceptible to subsurface damage on the interface between the hardened material and the softer substrate [4]. All of these degradation mechanisms eventually produce debris particles, and together with particles that may be introduced through improper maintenance, these act as the asperities that initiate abrasive wear.

Regarding wear, in a critique on common experimental practice, Bhadeshia [4] remarks that increasing contact stresses as a means to accelerate wear, likely influences the interaction of the interconnected degradation mechanisms, resulting in a different damage evolution process compared to the nominal design life. A similar remark may be extended to the common practice in bearing condition monitoring research of introducing artificial damage, as such simulated damage does not cover the interconnected nature of wear in rolling element bearings.

1.2 STATE-OF-THE-ART METHODS FOR CONDITION MONITORING OF LOW-SPEED ROLLER BEARINGS

To monitor degradation in rolling element bearings, several techniques have been suggested to date such as strain and vibration monitoring, lubrication analysis, electrostatic monitoring, temperature monitoring, and acoustic emission monitoring [5]–[8]. These techniques are reviewed for their potential to assess rolling element bearings under the particular operational conditions of the considered applications.

Most conventional in both research and practice are strain and vibration monitoring [9]–[11], which aim at detecting changes in the dynamic structural response of the bearing due to possible defects or imbalance. Analysis focuses on detecting cyclostationary frequencies, i.e. particular predefined frequencies associated with damages in particular components of the bearing [12], [13]. As such, vibration and strain monitoring are highly suitable for high-speed bearings with a consistent operational profile. More complex methods to account for variable speeds have been proposed [14], however, due to the limited change in the structural response associated with defects in low-speed bearings, these methods suffer from severely decreased detectability for the considered applications.

Lubrication analysis refers to a variety of techniques aiming to quantify the composition of the lubricant, in particular with regards to solid contaminants, i.e. wear debris. Typical means of analysis include spectroscopy, magnetic field detection, or filtration. Regarding effectiveness, a distinction is made between oil- and grease-based lubrication. Successful implementations of lubrication monitoring have been reported for oil-based systems [15]–[17], which may be attributed to the high flow-rate in such systems, stimulating homogeneous distribution of contaminants throughout the lubrication. For grease-based lubrication, i.e. the type of lubrication in the considered applications, due to the higher viscosity and the associated presence of partially stagnant pockets of lubrication in between the different components of a bearing, a more uneven distribution of the contaminants is encountered. As such, the performance of lubrication analysis is considered strongly dependent on the sampling quality [17], [18]. A final general critique with lubrication analysis is the delay that exists between the formation of degradation, and the detection of the resulting wear particles, giving rise to a period of increased abrasive wear and unmitigated risks to structural integrity. In a monitoring strategy, lubrication analysis seems to be most suited to the role of a complementary confirmation technique.

Electrostatic monitoring refers to techniques aiming to detect electric charge differences associated with surface interaction (e.g. contact charging), chemistry (e.g. oxidation), and topology alteration (e.g. caused by cracking and wear debris) [19]. A strong correlation to on-line lubrication monitoring is observed [20], [21]. The directional sensitivity of the sensor is strongly dependent on the distance to the charged particles [22], limiting the detection of charged particles to a localised zone directly in front of the sensor. The extension of these insights to possible implementation in a low-speed grease-lubricated roller bearing suggests that electrostatic monitoring provides limited advantage over lubrication analysis. Furthermore, when an integrated electrostatic monitoring system is considered, selection of the right instrumentation points in a low flow-rate environment remains challenging.

Temperature monitoring refers to techniques aiming to detect variation in the temperature of the different components of a bearing that may result from imbalance, friction, or other damage mechanisms. While it requires relatively simple instrumentation, common critiques with temperature monitoring concern the difficulty of interpreting changes for broadly varying operational conditions [23] and late detection – typically demonstrated in comparison to vibration monitoring [20], [24]. Hence, the method is not considered suitable for assessment of low-speed bearings in variable operational conditions.

Passively generated acoustic emissions (AE) have been investigated for their potential to detect early-stage degradation. AE refers to sudden release of energy in a material when the microstructure of said material is irreversibly altered due to damage (e.g. crack growth, or dislocation movement). The principle is graphically represented in Figure 1.2. Various applications of AE for monitoring damage in different fields have been reported so far, e.g. for the detection of fatigue cracks in steel bridges [25]–[27], cracking and rebar corrosion in concrete structures [28]–[31], and various degradation mechanisms in composite laminates [32]–[34]. This broad-scope experience with AE techniques in other domains demonstrates a general lower susceptibility of AE to operational and environmental conditions, high sensitivity to different degradation mechanisms from early stages of development, and a typical non-requirement of a baseline response. While these features are missing in the state-of-the-art for non-destructive evaluation of low-speed roller bearings, herein, AE offers the potential to bridge the gaps.

In roller bearings, AE signals radiate from the source event inside or on the interfaces of rolling elements, propagate through the bearing components and interfaces, e.g. between the rollers and raceways, and also partly through the lubricant. They get reflected, scattered, and diffracted, and finally, if the waves retain sufficient energy, they can be detected and measured on a surface that is accessible for instrumentation. All while the local geometry of the rolling elements, and possibly the attached sensors system, continuously shift in the operation of the bearing, imposing a dynamic transmission path between the source signal and detection thereof. This makes the analysis of AE signals in a roller bearing a non-trivial challenge [35].

A comprehensive review of the state-of-the-art on condition monitoring of roller bearings utilising AE methodologies is provided in the next section.

1.3 ACOUSTIC EMISSION MONITORING FOR CONDITION ASSESSMENT OF LOW-SPEED ROLLER BEARINGS

The prior art on the application of AE techniques for bearing condition monitoring seems to originate in 1969 with Balderston [36], who successfully demonstrated the potential for detecting defects prior to failure in a laboratory environment. A decade later, Rogers [37] pioneered the application of the technique on an asset in the field – on the slew bearing of an offshore crane. In his paper, Rogers discusses one of the primary challenges of interpreting field measurements; detecting no damage when there most likely is none, defining the crucial intersection between a false alarm and a missed detection.

In the subsequent decades other investigations have been reported, describing experimental studies of AE bearing condition monitoring, each within their own niche of operational conditions and targeted defect. Amongst these, of primary interest is the combination of naturally-introduced damage and very-low speed (<20 rpm), for which literature is limited due to the practical challenges associated with developing the degradation. In some early studies, this problem is mitigated by performing in-situ tests [37], [38], or by evaluating naturally pre-worn bearings from industry applications in the lab [39]. A downside of these approaches, is the loss of information on the progression on the damage, however, these studies
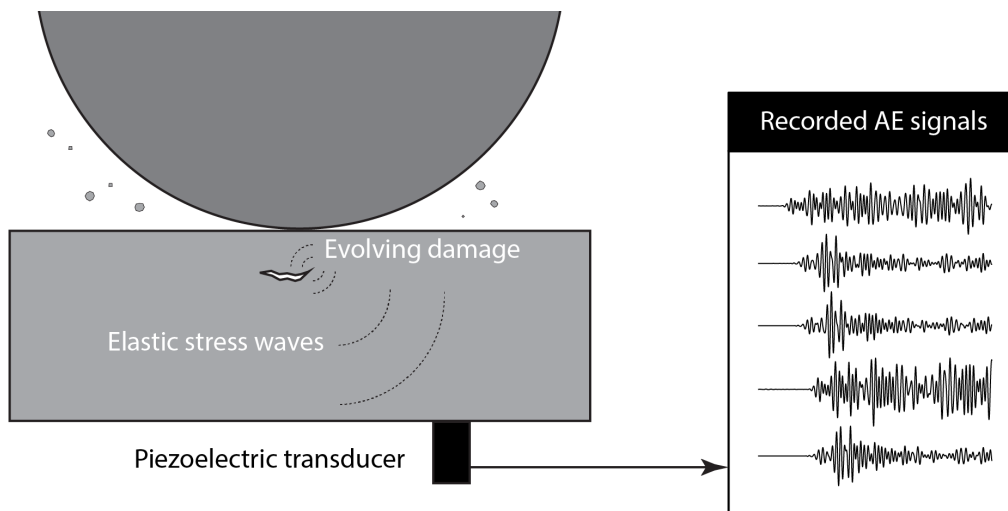
Figure 1.2: Illustration of the acoustic emission phenomenon.

have successfully demonstrated a greater sensitivity of AE compared to vibration monitoring at low speeds. In a field study, Mba et al. [38] observed that the recorded waveforms are specific to the propagation path between source and receiver. And Sako and Yoshie [40] identified naturally-developed flaking in a small-scale bearing at speeds between 1–10 rpm. However, the induced damage was the result of running for 98% of the lifetime at 400 rpm while overloading the bearing in the range of plastic deformation. Liu et al. [41] applied cyclostationary frequencies to evaluate a naturally worn bearing from a 15 year-old wind turbine at speeds ranging 0.5–5 rpm, while using discrete/random separation-based cepstrum editing liftering to amplify weak fault features from the AE signal. Finally, Caesarendra et al. [42] studied the development of degradation in a run-to-failure experiment lasting nearly 300 days, and identified a significant change in the bearing condition through conventional AE features.

Regarding studies on naturally-induced damage at higher speeds (>60 rpm), Li et al. [43] successfully differentiated between minor and major wear through evaluation of waveform features. Elforjani and Mba observed a correlation between increasing AE energy and the evolution of cracks and spalls in bearings [44]–[49] and made an attempt to estimate the size of surface defects from the AE signal duration [50]. Elforjani also applied artificial neural networks to predict the remaining useful life of a grease-starved bearing [51]. With further increasing speed, studies on applications of cyclostationary techniques become of note [52]–[55], which also propose downsampling of continuous AE data to ease data handling [56]. The correlation between AE energy and damage evolution and severity is further explored [57], [58]. Hidle et al. propose a detector for subsurface cracks based on the pulse integration method [59]. And in comparative studies also involving vibration monitoring, AE demonstrates earlier damage detection [60] – particularly when combined with spectral kurtosis [55], [61] – and fusion of vibration and AE data has shown to increase the reliability with respect to either method separately [62]. Besides these, k-means clustering of AE waveform features has been applied to identify crack

initiation and propagation [63], a correlation has been observed between lubrication film thickness and AE energy [64], [65]. Furthermore, in a fundamental study on rolling contacts, a correlation has been reported between evolving surface damage and the AE hit-rate [66].

Although experiments involving artificially-introduced damage are not considered representative of those involving naturally-developed degradation, these studies may still provide informative insights regarding the effectiveness of the explored signal processing techniques. Broad speed-range (10–1800 rpm) assessments have been performed by Smith [10] and McFadden and Smith [67]. For very-low speeds (~1 rpm), later studies implemented classification through autoregressive coefficients to differentiate between the unique transmission paths of several artificially-introduced damages [68], and ensemble empirical mode decomposition with multiscale principle component analysis [69] or multiscale wavelet decomposition [70] to identify the damaged component through characteristic frequencies. The applicability of multiscale wavelet decomposition was also demonstrated at a somewhat higher speed representative of the main bearing of a wind turbine [71]. For a similar speed-range (20–80 rpm), in comparisons between relevance vector machine (RVM) and support vector machine (SVM), RVM was demonstrated to be effective at classifying several damages in different components [72], [73]. In high-noise environments, both artificial surface and sub-surface defects were identified by applying probabilistic techniques (Gaussian mixture model) to differentiate between damage-initiated energy and background noise [74].

With further increasing speed, again cyclostationary techniques are explored for localised defects [75]–[77], with studies reporting improved early detection through the application of short-time techniques [78], [79], spectral correlation [80], and spectral kurtosis [81], and studies reporting improved performance in a high-noise environment by applying self-adaptive noise cancellation [82], least mean squares filtering [83]–[85], or wavelet based filtering [86]–[88]. Additionally, machine learning techniques, such as neural networks, have been suggested and implemented to identify characteristic defect frequencies from spectrograms [89], [90]. Alternative to cyclostationary techniques, time-of-arrival-based localisation is demonstrated for the detection of localised defects in static raceways [91], and the fusion of AE and vibration based multi-feature entropy distance is proposed for damaged-component identification [92]. In the same context the sensitivity of several AE features to various operational conditions has been evaluated [93]–[96]. Also a correlation between defect size and the AE burst duration and amplitude is reported [97]–[100]. Synonymous to the burst duration, this correlation has been observed for ringdown counts [101], and the time difference between double bursts as well [87], [102]. Concluding, material protrusions above the mean surface roughness were identified as the AE source mechanism of artificially-introduced defects [103].

Regarding lubrication contamination, literature typically describes experiments involving highly-controlled contaminated lubrication samples, which should be classified as artificial damage. However, the processes that generates the stress waves from the presence of the contaminated particles may remain comparable to the one for naturally-contaminated lubrication, provided that the contaminated samples are sufficiently representative of actual contamination. Studies have shown that the size, weight, and hardness of the particles are correlated to the amplitude of

AE signals [98], [104]–[107]. Also, the number of particles seems to correlate to the hit-rate of the contamination initiated signals [98], [104]. Besides these conventional characterisation approaches, machine learning algorithms – such as sparse dictionary learning [108] and a convolutional neural network [109] – have also been applied in early-stage studies to differentiate between contaminated and uncontaminated lubrication.

The prior art on AE bearing condition monitoring predominantly focuses on mid- and high-speed bearings. Furthermore, naturally-developed degradation also seems under-investigated. Particularly for this cumbersome combination, a framework aimed at proper description and interpretation of the propagation and transmission of AE source signals from different degradation types is needed and yet to be proposed.

1.4 RESEARCH OBJECTIVES

This dissertation presents a quantitative methodology for condition monitoring of highly-loaded low-speed roller bearings through passively generated acoustic emissions, with a particular focus of such bearings that are commonly used in the offshore industry. Specifically sheave bearings of heavy-lifting cranes and turret bearings in the single point mooring systems of floating production storage and offloading (FPSO) units are mentioned (Figure 1.1), which are illustrative for the size and speed range under consideration. Sheave bearings are radial bearings with a typical diameter in the order of half a metre, depending on the load they may run at up to 40 rpm. Their operational profile consists of intermittent periods of multiple rotations with varying speed in either direction. Turret bearings are three-race bearings restricting both radial and axial loads. Their sizes vary within a typical range of 8–30 metres, while they operate at a speed so low it is not effectively communicated in revolutions per minute. Referring to the relative movement of the outer ring compared to the inner ring, turrets bearings operate below speeds of 1 m·s⁻¹, gradually moving in either direction to mitigate the tides and wind, with irregularities in those events superimposing a two-directional flutter.

From the review of the literature, it is clear that the combination of low-speed and varying operation poses a challenge for the commonly applied techniques. Therefore, an alternative is proposed that utilises two basic principles of acoustic emission; (i) if consistently evolving damage is present, stress waves will be consistently emitted, and (ii) the generation, propagation and transmission of stress waves are governed by deterministic processes.

It is hypothesised that consistency in detection of similar AE signals indicates consistency in an AE source mechanism, and that consistency in an AE source mechanism indicates evolving degradation, such as crack growth. And also that the shape of the recorded AE signal may be used to determine the approximate origin of the signal. A first challenge for this approach may be the inter-component transmissibility of the ultrasonic stress waves, as it governs whether AE sources may be detectable at particular sensor locations. A second challenge for this approach may be the presence of equally consistent sources of noise, which may obfuscate the identification of degradation induced AE signals.

Towards the development of the aforementioned methodology, the following objectives are addressed in this dissertation:

1. Development of a framework to describe and analyse the propagation and transmission of ultrasonic stress waves in bearing geometries.

2. Quantification of inter-component transmission of ultrasonic stress waves in low-speed roller bearings.

3. Development of a framework to identify similarity in acoustic emission source mechanisms.

4. Identification of probable degradation-induced acoustic emission signals in a low-speed run-to-failure experiments at representative scales.

5. Development of a robust condition indicator for low-speed roller bearings.

1.5   STRUCTURE OF THE THESIS

The remainder of this dissertation is structured around three main chapters that address the four objectives listed in the previous section. Chapter 2 introduces the descriptive framework (Objective 1) and utilises it to assess the transmissibility of ultrasonic signals in an unloaded static bearing (Objective 2) through an experiment involving simulated AE signals. Chapter 3 expands on the descriptive framework (Objective 1) and utilises it to propose the identification framework (Objective 3). Subsequently the framework is applied to a run-to-failure experiment performed with a turret bearing mock-up (Objective 4). Chapter 4 proposes the bearing condition index (BCI) as an indicator (Objective 5), and applies this indicator to a run-to-failure experiment performed with a pre-worn bogie wheel bearing from the industry (Objective 4). Finally, Chapter 5 unites the separate parts in a review to conclude on the progress made towards the goal of this dissertation, also denoting recommendations for further research.

2

TRANSMISSION OF ULTRASONIC STRESS WAVES IN ROLLING ELEMENTS

This chapter is reproduced from [110]:

ABSTRACT

This chapter presents an approach to experimentally evaluate transmission in low-speed roller bearings for application in passive ultrasound monitoring. The results suggest that low- to mid-frequency signals (<200 kHz), when passing through the rollers and their interfaces from one raceway to the other, can retain enough energy to be potentially detected.

In condition monitoring of bearings using acoustic emission (AE), the restriction to solely instrument one of the two rings is generally considered a limitation for detecting signals originating from defects on the opposing non-instrumented ring or its interface with the rollers due to the particular balance between transmission and reflection of the signals [35]. In the present chapter, an analytical framework to describe transmission and propagation of ultrasonic waves through the geometry and interfaces of a roller bearing is introduced. Using this framework, stress wave transmission in a sheave bearing – from one raceway through the rollers to the other raceway – is experimentally investigated, making use of simulated sources. Transmission coefficients are extracted from time-frequency representations of the recorded waveforms. Tests are performed with a static bearing, as the dynamic state of the considered bearings (<20 rpm) is quasi-static from the perspective of stress wave propagation. Through these results, the feasibility of passive ultrasonic condition monitoring of low-speed roller bearings by single ring instrumentation is quantitatively evaluated.

2.1   A FRAMEWORK TO DESCRIBE ULTRASONIC STRESS WAVE TRANSMISSION

The detectability of developing degradation on different components of a bearing is governed by the transmission of elastic stress waves across the interfaces and through the components of that bearing. To describe and quantify this transmission, a framework is proposed to analyse the propagation of elastic stress waves in complex geometries. This framework approaches propagation, transmission, and detection of a signal as a series of transformations applied to the emitted source signal. The notation is motivated by the work of Berkhout [111] and Pahlavan et al. [112], [113].

Limited by the geometry of the assembled bearing and non-technical constraints for possible consideration of disassembly, the simulated stress waves could not be generated at internal locations, where degradation would be occurring in practice (illustrated in Figure 2.1a). Instead, the proposed framework allows for extraction of the transmission coefficients using simulated sources on the external surfaces of the bearing (illustrated in Figure 2.1b). These coefficients are expected to provide a conservative estimate of the feasibility.

(a)   (b)
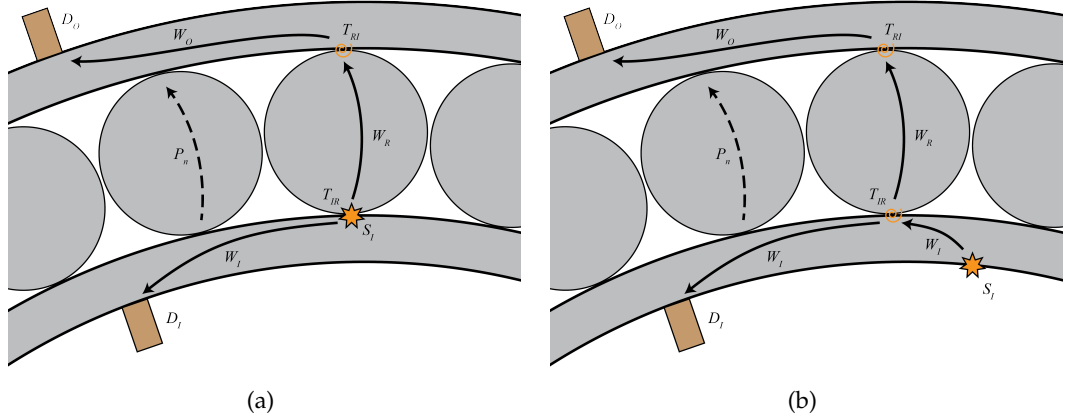
Figure 2.1: Representation of the wave propagation paths, showing: (a) The propagation paths associated with a natural sub-surface defect originating on the inner raceway, and (b) the propagation paths as simulated in the experiment. In both, the primary path is represented by a continuous line, and an alternative path as a dashed line.

For stress waves propagating directly from the source on the inner raceway to the receiver on that same inner raceway, the transmitted signal may be described in the frequency domain as

$$\hat{P}_{II}(\mathbf{s}_{DI}, \mathbf{s}_{SI}, \omega) = \hat{D}_I(\omega)\hat{W}_I(\mathbf{s}_{DI}, \mathbf{s}_{CI}, \omega)\hat{W}_I(\mathbf{s}_{CI}, \mathbf{s}_{SI}, \omega)\hat{S}_I(\omega) + \hat{P}_N. \qquad (2.1)$$

Wherein, $\hat{P}_{II}$ represents the response recorded at the receiver located on the inner raceway of the source emitted on the inner raceway, $\hat{D}_I$ the coupling transfer function of the receiver on the inner raceway, $\hat{W}_I$ the wave propagation function of the inner raceway, $\hat{S}_I$ the source function on the inner raceway, and $\hat{P}_N$ all neglected paths, mode conversions, and scattering of the transmitted response, and the background noise. Furthermore, $\mathbf{s}$ denotes a spatial location, e.g. the position of a receiver on

the inner raceway ($\mathbf{s}_{DI}$), a source on the inner raceway ($\mathbf{s}_{SI}$), and the contact point between the roller and inner raceway ($\mathbf{s}_{CI}$). Finally, ω denotes the angular frequency.

In this formulation, wave propagation inside of the raceway is split into two contributions, a part from the source to the roller-raceway contact spot $\mathbf{s}_{CI}$, and the continuation from that spot to the receiver. Note that the wavelengths of the dominant wave modes are generally larger than (or comparable to) the thickness of the raceway, hence they are expected to propagate as guided waves. With wave propagation only taking place along the raceway, the propagation function in the raceway can be expressed as:

$$\hat{W}_I(\mathbf{s}_{DI}, \mathbf{s}_{SI}) \approx \hat{W}_I(\mathbf{s}_{DI}, \mathbf{s}_{CI})\hat{W}_I(\mathbf{s}_{CI}, \mathbf{s}_{SI}). \tag{2.2}$$

Stress waves propagating from the same source on the inner raceway to a receiver on the opposing outer raceway may be described by

$$\hat{P}_{OI}(\mathbf{s}_{DO}, \mathbf{s}_{SI}, \omega) = \hat{D}_O(\omega)\hat{W}_O(\mathbf{s}_{DO}, \mathbf{s}_{CO}, \omega)\hat{T}_{RO}(F, \omega)\hat{W}_R(\mathbf{s}_{CO}, \mathbf{s}_{CI}, \omega)$$
$$\hat{T}_{IR}(F, \omega)\hat{W}_I(\mathbf{s}_{CI}, \mathbf{s}_{SI}, \omega)\hat{S}_I(\omega) + \hat{P}_N. \tag{2.3}$$

Wherein, $\hat{P}_{OI}$ represents the response recorded at the receiver located on the outer raceway of the source emitted on the inner raceway, $\hat{D}_O$ the coupling transfer function of the receiver on the outer raceway, $\hat{T}_{IR}$, and $\hat{T}_{RO}$ the transmission functions for the interfaces between the inner raceway and roller, and the roller and outer raceway respectively, and $\hat{W}_R$, and $\hat{W}_O$ the wave propagation functions of the roller, and outer raceway respectively. Furthermore, additional points in space are defined, which denote the position of a receiver on the outer raceway ($\mathbf{s}_{DO}$), and the contact point between the roller and outer raceway ($\mathbf{s}_{CO}$). Finally F denotes the contact force between the roller and raceways.

This formulation uses a similar structure to Equation (2.1), for describing wave propagation from source to contact point and from contact point to receiver. The major difference in Equation (2.3) with respect to Equation (2.1) is the inclusion of the transmission into, propagation over, and transmission out of the roller. Using the similarity between Equations (2.1) and (2.3), a formulation may be established that expresses the recording on the outer raceway as a transformation of the recording on the inner raceway. For this, it is assumed that the receivers have similar transfer functions, and that coupling variation is either negligible or accounted for in pre-processing, such that $\hat{D}_O \approx \hat{D}_I$. Additionally, wave propagation in the raceways is assumed to be comparable, i.e. $\hat{W}_I(\mathbf{s}_{DI}, \mathbf{s}_{CI}) \approx \hat{W}_O(\mathbf{s}_{DO}, \mathbf{s}_{CO})$. Then transmission from one raceway to the other is given by

$$\hat{P}_{OI}(\mathbf{s}_{DO}, \mathbf{s}_{SI}, F, \omega) = \underbrace{\hat{T}_{RO}(F, \omega)\hat{W}_R(\mathbf{s}_{CO}, \mathbf{s}_{CI}, \omega)\hat{T}_{IR}(F, \omega)}_{\hat{A}_R} \hat{P}_{II}(\mathbf{s}_{DI}, \mathbf{s}_{SI}, \omega). \tag{2.4}$$

It shows that the relative amplitude $\hat{A}_R$ is composed of transmission functions $\hat{T}_{IR}$ and $\hat{T}_{RO}$, and propagation through the roller $\hat{W}_R$.

If attenuation of waves in the roller is considered to be reasonably small due to the relatively short propagation path with respect to the wavelength ($|\hat{W}_R(\mathbf{s}_{CO}, \mathbf{s}_{CI})| \approx 1$), under the assumption of negligible phase shift, and transmission over the interfaces is assumed to be independent of the propagation direction ($\hat{T}_{RO} \approx \hat{T}_{IR}$), then represents about twice the value for transmission over a single interface in the dB-scale. This quantity may be experimentally investigated.

2.1.1   *Simulated Acoustic Emissions in a Sheave Bearing*

A cylindrical roller bearing of type F 566437.NNT by MTK Bearings was instrumented on the exterior of the inner and outer ring with standard piezoelectric AE sensors. The bearing had been in service in a sheave of a 4,000 mT heavy-lifting crane on a deep-water construction vessel. During the tests, the bearing was positioned horizontally to omit self-loading with no external loads applied. These conditions were used to obtain a conservative estimate of the worst transfer characteristics. A picture and an illustration of the set-up are shown in Figure 2.2.

(a)   (b)
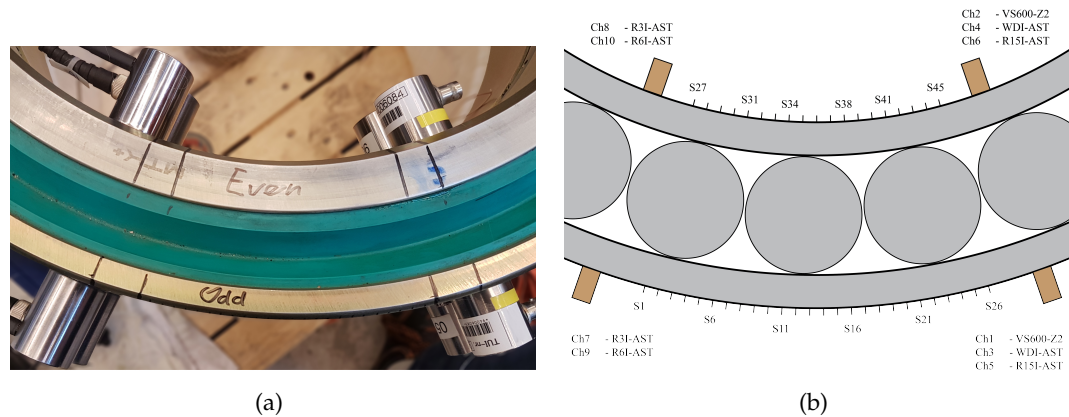
Figure 2.2: The top view of the transmission test set-up, showing: (a) A picture of the instrumented bearing, and (b) a to-scale illustration indicating the sensor and source positions. Note that the roller positions in the illustration are purely indicative, and unknown in the actual experiment.

The utilised type F 566437.NNT of MTK Bearings is a double row full complement cylindrical roller bearing. It has an outer diameter of 500 mm, an inner diameter of 360 mm, and a width of 175 mm. The inner ring is split in two segments of half width. Both inner rings and the outer ring act as raceways. The two rows each contain a compliment of 30 rollers with a diameter of 44.8 mm and a width of 55 mm. The rings and raceways are all made out of GCr15 bearing steel. It has the respective static and dynamic load ratings of 6,200 kN and 2,800 kN.

A bearing segment of 30 degrees had been selected for source excitation to guarantee the presence of at least two rollers within the segment. Pencil lead breaks were performed in 45 regularly-spaced source locations on the inner and outer raceway to excite stress waves. In accordance with ASTM-E976 [114], 10 Hsu-Nielsen excitations were performed at each 5 mm spaced source location using 0.5 mm 2H pencil leads.

Transmission of the excited waves through the bearing components has been recorded in the frequency range of 30–650 kHz. For this purpose, five types of commercial piezoelectric AE sensor were used, i.e. (i) 30 kHz resonant R3I-AST, (ii) 60 kHz resonant R6I-AST, (iii) 150 kHz resonant R15I-AST, (iv) wideband WDI-AST, and (v) 600 kHz resonant VS600-Z2. The first four (i–iv) have been sourced from Physical Acoustics Corporation, and contain an integral pre-amplifier with a gain of 40 dB. The fifth (v) has been sourced from Vallen Systeme, and was amplified using an external AEP5H pre amplifier set to the same gain of 40 dB. A Vallen Systeme

AMSY-6 system was used to sample the detected waveforms with 40 MHz for both feature- and transient-data whenever a 40 dB threshold was crossed. This sample includes a 200 μs pre-trigger recording before the threshold crossing. No additional digital band-pass filters were applied prior to storing the waveforms.

2.1.2 *The Wavelet Transform*

In order to estimate the frequency-dependent characteristics of wave propagation of roller bearings, the recorded time-series were converted to the time-frequency domain using the wavelet transform. The procedure for this transform can be described as a series of cross-correlations with rescaled and translated versions of a reference signal, i.e. the wavelet function. In the time domain this transformation is defined as

$$w_\psi(\tau, s) \equiv \int_{-\infty}^{\infty} \frac{1}{s} \psi^* \left(\frac{t - \tau}{s} \right) x(t) dt. \tag{2.5}$$

Wherein, w_ψ represents the wavelet transform of signal $x(t)$ with wavelet function $\psi(t)$, and ψ^* denotes the complex conjugate of the wavelet ψ. Furthermore, τ denotes the translation of the wavelet function in time, and s the scale of the wavelet. In this study a Morse wavelet is used [115]–[118], which is defined in the frequency domain. The time domain representation of this wavelet is obtained using the inverse Fourier transform,

$$\psi_{\beta,\gamma}(t) = \frac{1}{2\pi} \int_{-\infty}^{\infty} \hat{\Psi}_{\beta,\gamma} e^{i\omega t} d\omega, \tag{2.6}$$

with the Morse wavelet defined as

$$\hat{\Psi}_{\beta,\gamma}(\omega) \equiv a_{\beta,\gamma} \omega^\beta e^{-\omega^\gamma} \times \begin{cases} 1 & \omega > 0, \\ \frac{1}{2} & \omega = 0, \\ 0 & \omega < 0, \end{cases} \tag{2.7}$$

wherein

$$a_{\beta,\gamma} \equiv 2 \left(\frac{e\gamma}{\beta} \right)^{\beta/\gamma}. \tag{2.8}$$

In Equations (2.6), (2.7), and (2.8), $\hat{\Psi}_{\beta,\gamma}$ and $\psi_{\beta,\gamma}$ denote the respective frequency and time domain representations of the Morse wavelet, with $a_{\beta,\gamma}$ representing a normalising constant. Furthermore, e is Euler's number, and β and γ denote the respective order and family of the wavelet, which control the low-frequency behaviour and high-frequency decay.

This procedure transforms the time domain signal into the translation-scale domain, which is synonymous with the time-frequency domain. To express the former in the latter, one must first consider that translation space is representative of the temporal space, such that $t_\tau = \tau$. Then, to express scale in terms of frequency, one must consider that three meaningful frequencies may be defined for a wavelet; (i) the peak frequency, where the wavelet amplitude is maximised, (ii) the energy frequency,

where the centroid of the wavelet energy is situated, and (iii) the instantaneous frequency evaluated at the centre of the wavelet, where $t = 0$.

Since each of these frequencies is considered to be a valid interpretation of the frequency of the wavelet, a definite mapping of scale to frequency can only be obtained if these three frequencies coincide. This is nearly the case for a Morse wavelet with $\gamma = 3$ [115]. As this is the family of Morse wavelet used in this study, the wavelet frequency is approximated using the peak frequency, which is given by

$$\omega_{\beta,\gamma} \equiv \left(\frac{\beta}{\gamma}\right)^{1/\gamma}, \tag{2.9}$$

in which $\omega_{\beta,\gamma}$ denotes the peak frequency. Subsequently, the scale frequency is linked to the peak frequency through the scale, as

$$\omega_s = \frac{\omega_{\beta,\gamma}}{s}, \tag{2.10}$$

wherein ω_s denotes the scale frequency.

For each sensor type a frequency window has been selected for which Equation (2.4) is evaluated. Making reference to the same numbering as used before for the sensor types, these window are (i) 30–55 kHz, (ii) 55–80 kHz, (iii) 80–180 kHz, (iv) 180–550 kHz, (v) 550–650 kHz. For each sensor pair on the opposing raceways, the experimental relative amplitude is determined as the difference between the logarithmic peak value of the first arrival of the windowed wavelet transformed signals.

2.1.3   Correction for Coupling Variation

In pre-processing, a procedure for coupling variation correction has been implemented to compensate for possible differences in the coupling between receiver pairs (as discussed with the assumptions under which Equation (2.4) holds). For each receiver pair, assuming that the coupling variation predominantly manifest itself in signal amplification variation (and not phase), a scaling factor has been applied to the signals recorded on the inner raceway.

The scaling factors have been determined by comparing direct recordings at fixed distances from each sensor on the outer raceway, to the corresponding direct recordings on the inner raceway. The mean difference in logarithmic peak amplitudes of the frequency-windowed time frequency representation of the signals determines the correction factor.

Since only the relative amplitudes for each receiver pair are used throughout the analysis, the signal amplitudes do not need to be corrected individually to obtain absolute values.

2.1.4   Overview of Transmission Processing Approach

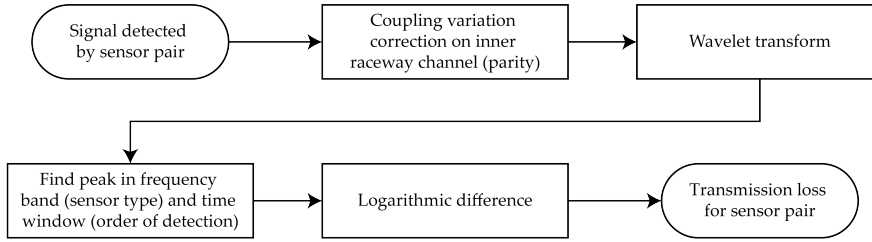An overview of the full processing procedure is included in Figure 2.3.

Figure 2.3: Overview of the procedure for transmission data processing.

2.2 STRESS WAVE TRANSMISSION RESULTS & DISCUSSION

For the combined 45 source locations, a total of 475 events have been recorded that surpass the minimal requirement of being detected by at least three of the five sensor pairs, each with a threshold of 40 dB. Out of these 475 events, 419 contain recordings for all channels. The events that are not recorded by all channels, typically originate from an outer raceway source, and miss a recording for one of the R15I-AST sensors, due to an insufficiently low threshold for some of the weaker source excitations. An overview of several recorded waveforms for a select few source locations is presented in Figure 2.4 for outer raceway sources and Figure 2.5 for inner raceway sources.

Time-frequency representations of the recorded waveforms are obtained through the continuous wavelet transform. Herein, the used wavelet is a Morse wavelet with $\gamma = 3$ (family) and $\beta = 20$ (order). The family has been selected to obtain a unambiguous wavelet frequency, whereas the order has been tuned to obtain sufficiently narrow frequency-localisation, while retaining ample time-localisation. Slight adjustments to these empirically-tuned values are not expected to influence the results of this study.

A randomly-selected event is illustrated in more detail to better explain the processing procedure. This event originated from source location S22 on the outer ring (indicated in Figure 2.2b by the mark directly right of S21). The time traces and time-frequency representations for all five sensor pairs of this randomly selected event are shown in Figure 2.6 (VS600-Z2), Figure 2.7 (WDI-AST), Figure 2.8 (R15I-AST), Figure 2.9 (R3I-AST), and Figure 2.10 (R6I-AST). For the rest of this section when the subfigures are mentioned, it is meant to refer back to those figures collectively.
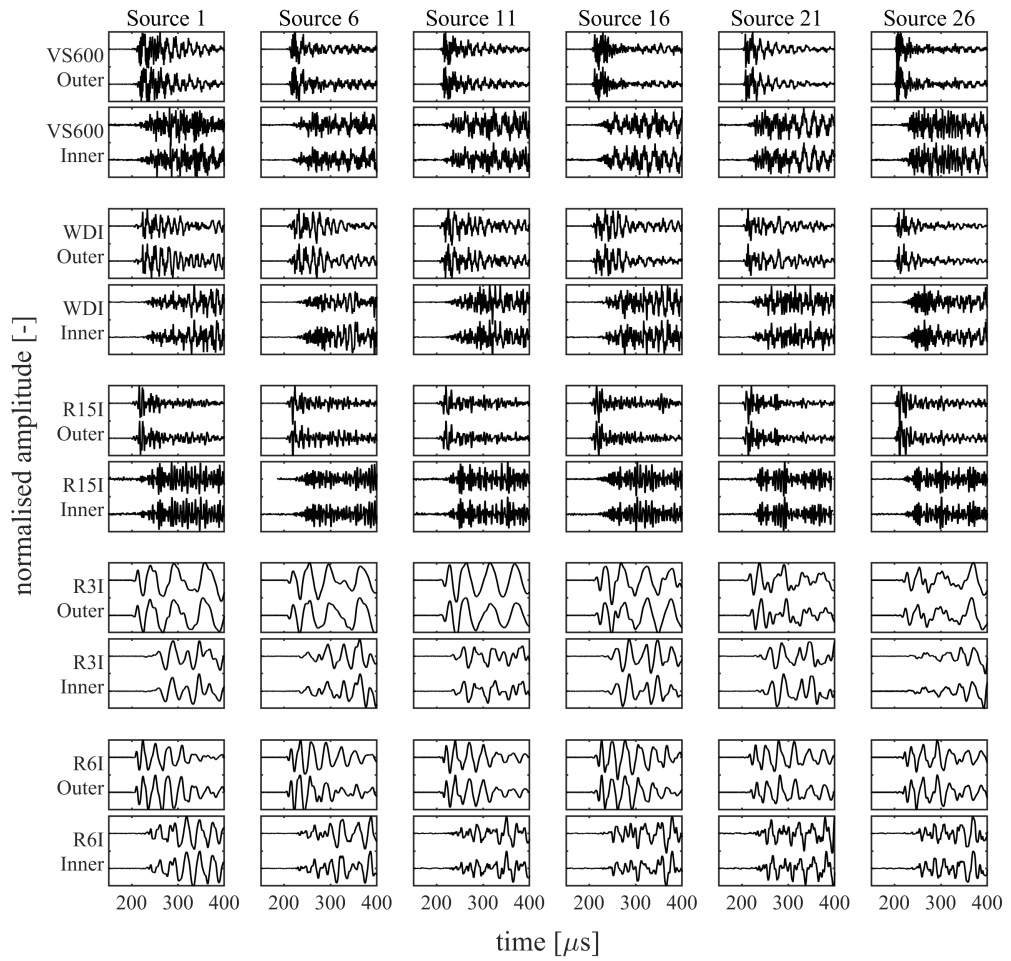
Figure 2.4: Overview of recorded waveforms for several outer raceway sources. Each block depicts a 250 μs sample of two waveforms that have been normalised with their respective peak amplitudes.
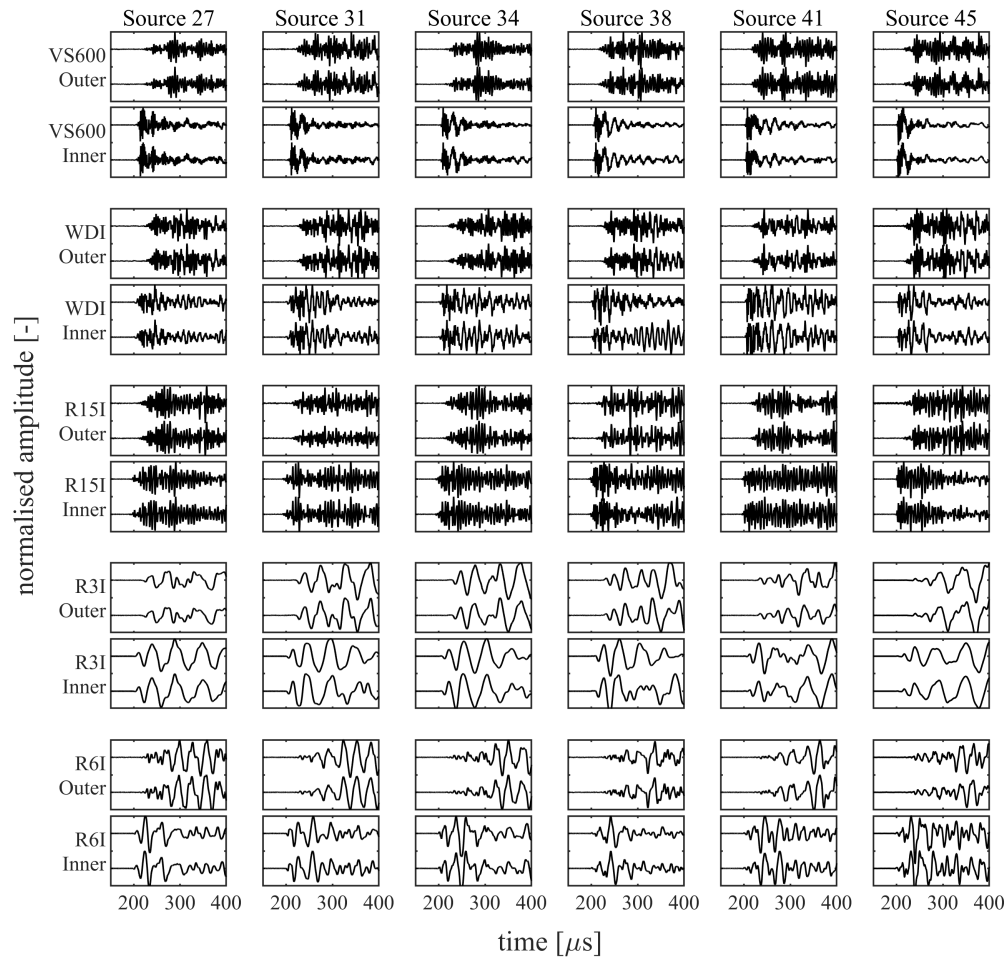
Figure 2.5: Overview of recorded waveforms for several inner raceway sources. Each block depicts a 250 µs sample of two waveforms that have been normalised with their respective peak amplitudes.

Figure 2.6: Randomly selected event recorded by VS600-Z2 sensors, originating from a source location S22, showing: the time traces recorded on the outer raceway (ch1, top left) and on the inner raceway (ch2, top right), and the time-frequency representation of the recorded signals on the outer (bottom left) and the inner (bottom right) raceways. The detected magnitude in the time-frequency representations of the signals are indicated by the intersection of the dotted lines, the dashed lines indicate the frequency range of interest (550–650 kHz).
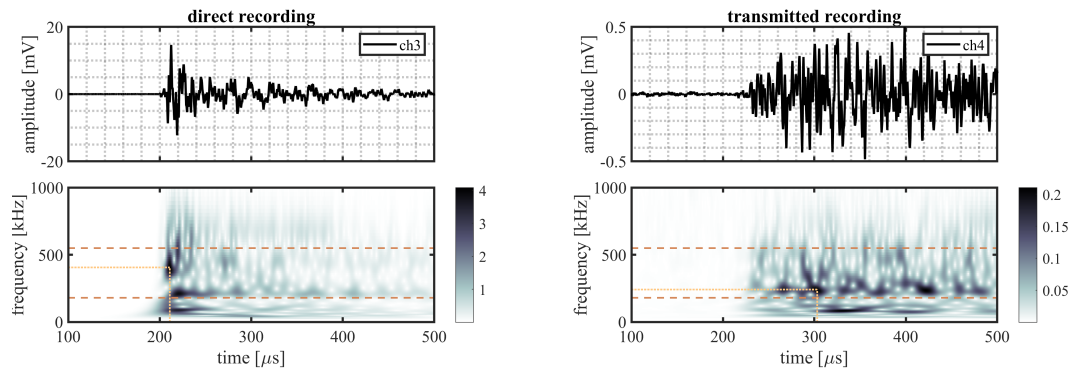
Figure 2.7: Randomly selected event recorded by WDI-AST sensors, originating from a source location S22, showing: the time traces recorded on the outer raceway (ch3, top left) and on the inner raceway (ch4, top right), and the time-frequency representation of the recorded signals on the outer (bottom left) and the inner (bottom right) raceways. The detected magnitude in the time-frequency representations of the signals are indicated by the intersection of the dotted lines, the dashed lines indicate the frequency range of interest (180–550 kHz).
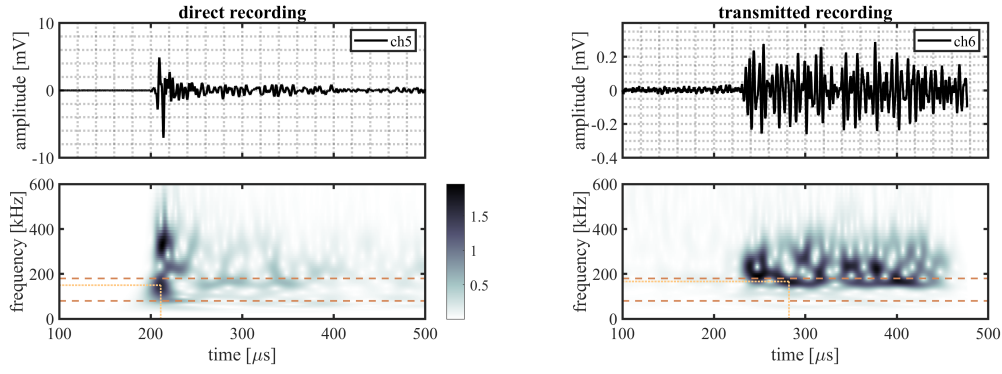
Figure 2.8: Randomly selected event recorded by R15I-AST sensors, originating from a source location S22, showing: the time traces recorded on the outer raceway (ch5, top left) and on the inner raceway (ch6, top right), and the time-frequency representation of the recorded signals on the outer (bottom left) and the inner (bottom right) raceways. The detected magnitude in the time-frequency representations of the signals are indicated by the intersection of the dotted lines, the dashed lines indicate the frequency range of interest (80–180 kHz).
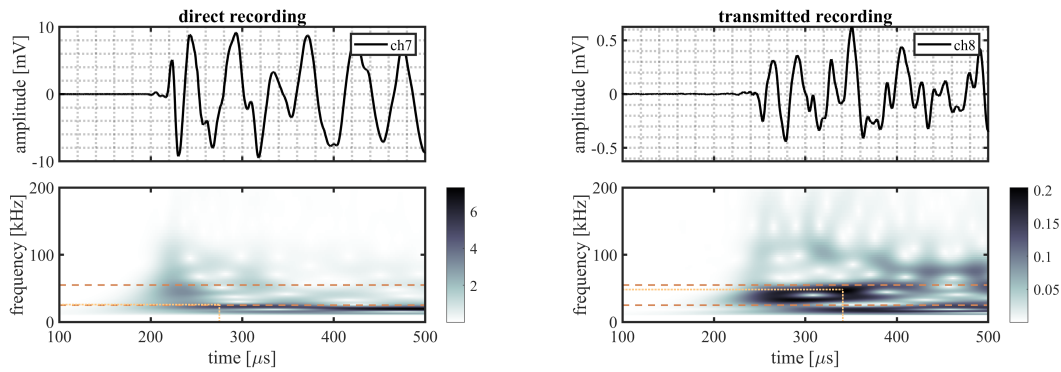
Figure 2.9: Randomly selected event recorded by R3I-AST sensors, originating from a source location S22, showing: the time traces recorded on the outer raceway (ch7, top left) and on the inner raceway (ch8, top right), and the time-frequency representation of the recorded signals on the outer (bottom left) and the inner (bottom right) raceways. The detected magnitude in the time-frequency representations of the signals are indicated by the intersection of the dotted lines, the dashed lines indicate the frequency range of interest (30–60 kHz).
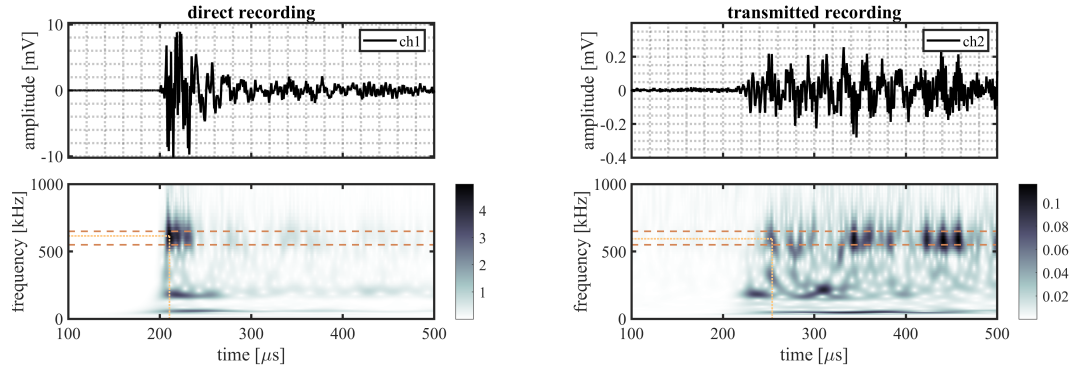
Figure 2.10: Randomly selected event recorded by R6I-AST sensors, originating from a source location S22, showing: the time traces recorded on the outer raceway (ch9, top left) and on the inner raceway (ch10, top right), and the time-frequency representation of the recorded signals on the outer (bottom left) and the inner (bottom right) raceways. The detected magnitude in the time-frequency representations of the signals are indicated by the intersection of the dotted lines, the dashed lines indicate the frequency range of interest (55–80 kHz).
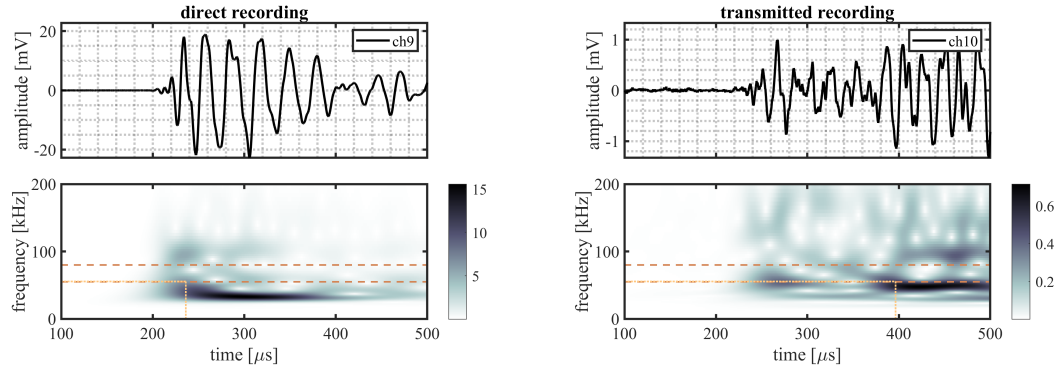
Initial observation of the time traces in the top subfigures show the odd channels to detect the signal earlier and with higher peak-amplitude. These observations indicate the source signal originates from the same ring the odd numbered channels are located on, i.e. the outer raceway. As such, this event evaluates transmission from the outer raceway to the inner raceway. It must be noted that this propagation direction is opposing to the transmission explicitly denoted in Equation (2.4).

For the time-frequency representations of the signal recorded on the source side, shown in the bottom left subfigure, the peak magnitude of the wavelet transform within the considered frequency range is selected as the reference magnitude of the source signal. This peak is indicated by the intersection of the dotted lines.

On the opposing raceway, shown in the bottom right subfigure, the reference magnitude for the transmitted signal is obtained by selecting the peak magnitude within the considered frequency band that occurs in the range of 50–250 µs following on the selected reference magnitude of the source signal. This selection is made to avoid picking a maximum resulting from interacting reflections. This approach, however, is not fault proof, as it may be susceptible to interacting arrivals from different transfer paths of similar length. This effect is partly mitigated by averaging over multiple source locations.

From the two selected reference magnitudes, the relative amplitude of the transmitted signal is obtained by determining the difference between their logarithmic-scale values.

A noteworthy observation may be that the detection of the peak magnitudes for the WDI-AST type sensors, as shown in Figure 2.7, occurred at the lower end of the selected frequency range. This may place the results for this sensor type closer to the mid-frequency range, than the high-frequency range.

For each source excitation, on each source location, the same procedure is applied for each sensor type. An overview of all relative amplitudes is shown in Figure 2.11. In this figure the relative amplitude for each sensor type and transmission direction

is depicted as an individual boxplot. Signal transmission from the outer to the inner raceway, i.e. the direction of the selected example event, is indicated by the label O-I, and presented on the right side for each sensor group. Signal transmission from the inner to the outer raceway, i.e. the direction for which Equations (2.1), (2.3), and (2.4) have been established, is indicated by the label I-O, and presented on the left side for each sensor group.
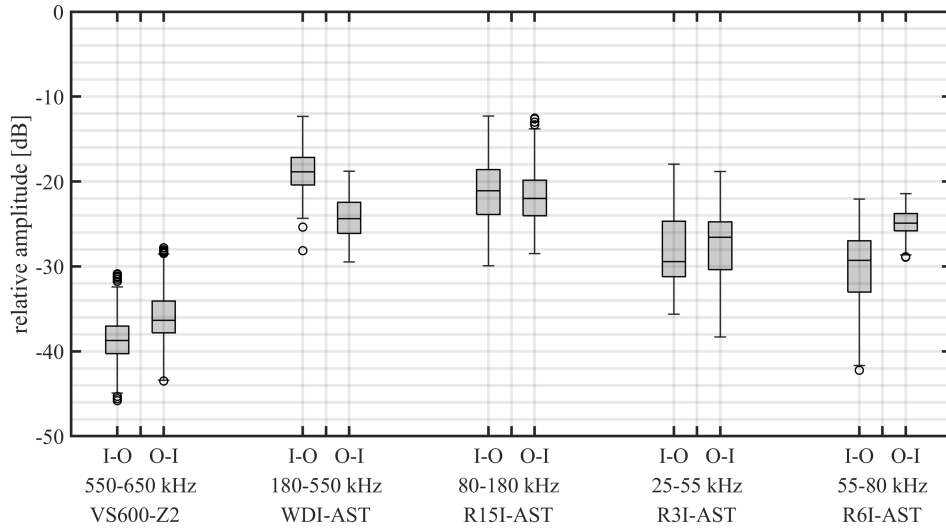
Figure 2.11: Overview of relative amplitudes for different frequency ranges and transmission directions, where I-O refers to transmission from the inner ring to the outer ring, and O-I to transmission from the outer ring to the inner ring. The shaded box denotes the median and the range between the lower and the upper quartile, the circles represent outliers, and the whiskers indicate the non-outlier minima and maxima.

The results indicate that (i) transmission is most favourable in the range of 80–180 kHz (as recorded by R15I-AST), (ii) for this frequency range, a mean amplitude drop of 20–25 dB is to be expected, (iii) the general performance of WDI-AST resembles R15I-AST, indicating consistent near mid-frequency selection from the broadband window, (iv) for lower frequencies, mean transmission losses are slightly higher, ranging between 25–30 dB, and (v) higher frequencies suffer from significant mean transmission losses (>35 dB).

Increased transmission losses at higher frequencies are expected to be partly related to non-negligible attenuation in the roller. For a frequency of 600 kHz the wavelength is notably smaller than the diameter of the roller, which could give rise to spreading and increased attenuation. Mid- and low-frequency results show that the assumption of negligible attenuation is reasonable for this geometry below 200 kHz, representing wavelengths in the same order of magnitude as the diameter of the roller.

Note that the presented transmission losses are in terms of the relative amplitude $\hat{A}_R$ as defined by Equation (2.4), and thus include transmission into, through, and out of the roller. Considering the aforementioned assumptions of negligible attenuation inside rollers and directional independence, it may generally be stated

the transmission loss for a single interface at mid-frequency is in the order of 10–13 dB.

Also, the presented relative amplitude has been obtained for a bearing in horizontal position, thus without applied loading or self-weight. It is assumed that this position provides a conservative estimate on transmission, when compared to a loaded bearing in operation.

2.3   CONCLUSIONS

A framework to describe and assess the transmission of ultrasonic waves through the geometry and interfaces of a roller bearing is presented. Combined with experimental data, this framework is used to quantify stress wave transmission from one raceway, through a roller, to the other raceway. The experiments make use of a statistically large sample of Hsu-Nielsen sources, and multiple AE sensors to cover a frequency range from 30–650 kHz. Quantitative analysis of the recorded signals suggests that (i) the transmission of AE signals through rollers and their interfaces is potentially of sufficient strength to be recorded and distinguished from the background noise, (ii) transmission is most favourable in the mid-frequency range (80–180 kHz), (iii) for mid frequencies, a transmission loss of 10–13 dB is to be expected per interface, (iv) for lower frequencies, transmission is slightly less favourable (12–15 dB per interface), and (v) for higher frequencies, transmission degrades significantly (17–20 dB per interface).

The presented study demonstrates the principle feasibility of single ring instrumentation in bearing condition monitoring, when rotation may be considered quasi-static relative to stress wave propagation. However, since only static tests have been performed, influences of dynamic effects on the ultrasonic noise are to be assessed and quantified.

3

ASSESSMENT OF ACOUSTIC EMISSIONS DUE TO NATURALLY-DEVELOPING DEGRADATION IN A LOW-SPEED ROLLER BEARING

This chapter is reproduced from [119]:

ABSTRACT

This chapter presents an approach to identify naturally-developed degradation in low-speed roller bearings using waveform-similarity-based clustering of acoustic emissions under fatigue loading. The results highlight that the proposed cross-correlation-based clustering of AE waveforms and identification of multi-channel formations in said clusters compose a suitable methodology for assessment of damage in low-speed roller bearings.

In the present chapter, detection and identification of degradation-induced ultrasonic signals in low-speed roller bearings have been experimentally investigated. A similarity-based clustering approach for the identification of consistent AE sources is implemented for detection of consistent degradation modes (e.g. crack growth). This approach is motivated by the notation that each recorded AE signal from a particular degradation is defined by the convolution of the source signal, transfer function of the propagation path, and transfer function of the utilised sensor, and may thusly be used to identify consistent AE sources. It is applied to an experimental evaluation of naturally developing degradation in a large-scale highly-loaded low-speed roller bearing. First the framework and identification approach are discussed. Subsequently, the test set-up, instrumentation and experimental procedures are described. Through a discussion of the results of the run-to-failure experiment, the framework and identification approach are evaluated. Finally the last section provides the conclusions of this study.

3.1   THE IDENTIFICATION OF CONSISTENCY IN ACOUSTIC EMISSION SOURCE MECHANISMS

Identification of developing degradation in rolling elements may follow directly from the identification of AE source signals. In an idealised situation, instrumentation is situated close to the source of emission, i.e. where damage is evolving. There, the recorded signal is nearest in form to the original source signal, and therefore, the task of identifying the mechanism of emission is most apparent. In practice, instrumentation on the raceway can typically not be realised, and therefore generalisation to the external surface of a bearing – or the substructure – is necessary. This generalisation is demonstrated analytically in this work. Experimentally, the concept is applied to identify naturally-evolving damage in a bearing. A purpose-built linear bearing is used in the experiment, as depicted in Figure 3.1, which is designed to provide the ability to instrument both the raceways and substructure, to assess the identification procedure for both instrumentation scenarios. Dimensions used in this research are given in Table 3.1.

(a)

(b)

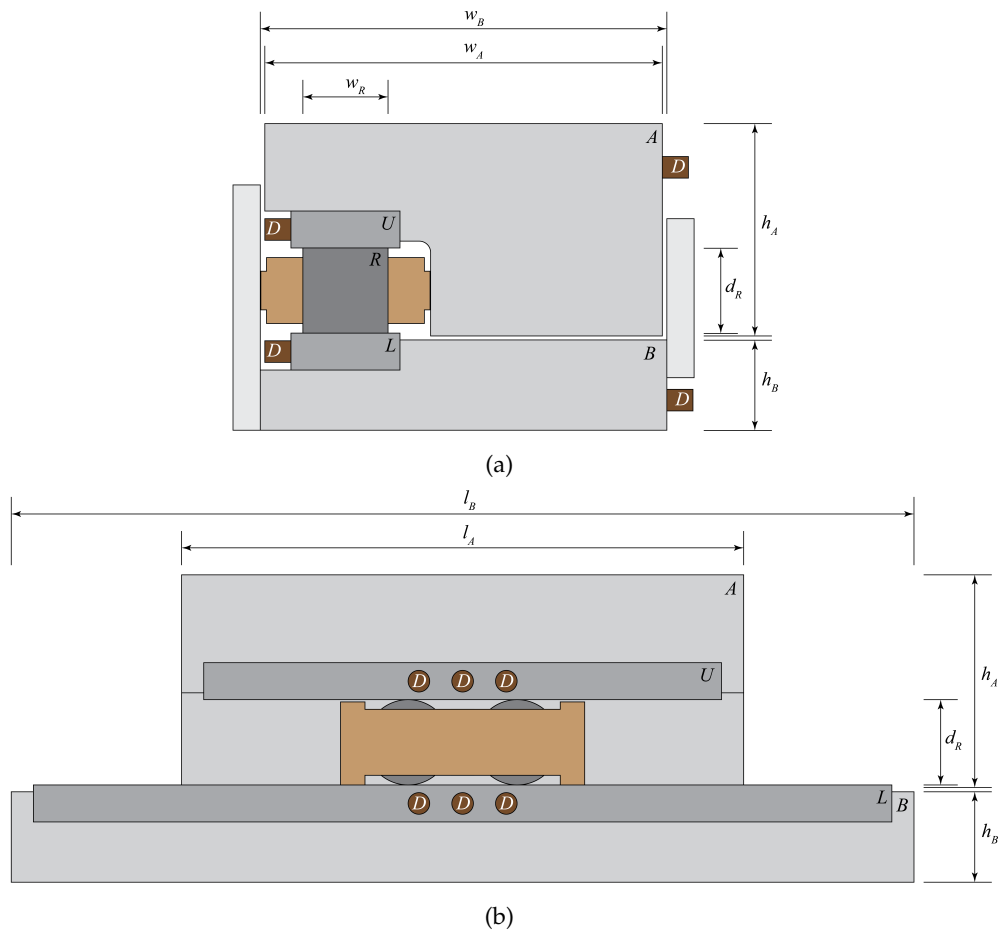Figure 3.1: Illustrations of the turret bearing test set-up (to scale, top section), showing; (a) a cross-section of the bearing with component identifiers, and (b) a front view of the bearing without the cover-plate. Indicated components are the roller (R), the nose raceway (L), the support raceway (U), the nose substructure (B), the support substructure (A), and the sensor arrays (D).

For the rolling elements of a bearing, three main regions may be considered for degradation-induced sources. Figure 3.2 illustrates these, which are, (a) subsurface in the raceway, (b) subsurface in the roller, and (c) the interface of roller and raceway. Evading the challenges of instrumenting a roller, the closest instrumentation could at best be situated directly on the raceway. However, in practice instrumentation on the raceway is often not feasible, and therefore sensors are often situated on the support structure – further away from the source. The effect of this extra distance on the transformation on the source signal, is discussed in detail for the three identified cases. Herein the notation proposed in Chapter 2 is used, which was inspired by work of Berkhout [111] and Pahlavan et al. [112], [113].
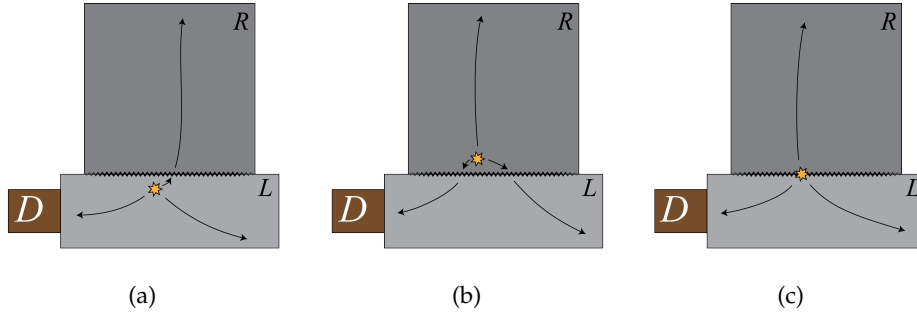
Figure 3.2: Three alternative source configurations with primary transfer paths, showing; (a) a subsurface source in the raceway, (b) a subsurface source in the roller, and (c) a source on the interface between roller and raceway.

Considering a subsurface-crack that is propagating in the nose raceway, as illustrated by Figure 3.2a, a recording from a receiver on that same raceway may be described in the frequency domain as

$$\hat{P}_{LL}(\mathbf{s}_{DL}, \mathbf{s}_{SL}) = \hat{D}_L \hat{W}_L(\mathbf{s}_{DL}, \mathbf{s}_{SL})\hat{S}_L + \hat{P}_N. \tag{3.1}$$

Herein, $\hat{P}_{LL}$ represents the recorded response at a receiver on the nose raceway (L in Figure 3.1) of a source signal originating from the nose raceway, $\hat{D}_L$ the coupling transfer function of the receiver on the nose raceway, $\hat{W}_L$ the propagation function of the nose raceway, $\hat{S}_L$ the source function on the nose raceway, and $\hat{P}_N$ all neglected paths, mode conversions and scattering of the transmitted response, and the background noise. Furthermore, $\mathbf{s}_{SL}$, and $\mathbf{s}_{DL}$ denote points in space where the respective source and receiver – both on the nose raceway – are located. Note that in this chapter the denotion of the angular frequency (ω) is omitted for conciseness.

That same source signal will also be transmitted over the interfaces, through the roller, into the opposing raceway. If in transmission it retains sufficient energy to surpass the ultrasonic background noise, and to be detectable by a receiver on that opposing raceway, the recorded signal may be described by

$$\hat{P}_{UL}(\mathbf{s}_{DU}, \mathbf{s}_{SL}, F) = \hat{D}_U \hat{W}_U(\mathbf{s}_{DU}, \Gamma_{UR})\hat{T}_{RU}(F)\hat{W}_R(\Gamma_{UR}, \Gamma_{LR})\hat{T}_{LR}(F)\hat{W}_L(\Gamma_{LR}, \mathbf{s}_{SL})\hat{S}_L$$
$$+ \hat{P}_N. \tag{3.2}$$

Herein, $\hat{P}_{UL}$ represents the recorded response at a receiver on the support raceway (U in Figure 3.1) of a source signal originating from the nose raceway, $\hat{D}_U$ the

coupling transfer function of the receiver on the support raceway, $\hat{W}_R$, and $\hat{W}_U$ the propagation functions of the respective roller, and support raceway, and $\hat{T}_{LR}$, and $\hat{T}_{RU}$ the transmission functions for the interfaces between the nose raceway and roller, and between the roller and support raceway respectively. Note that for the transmission function the order of the subscripted domains implies directionality. Furthermore, the additional point in space $\mathbf{s}_{DU}$ indicates the location of a receiver on the support raceway, while Γ_{LR}, and Γ_{UR} denote the boundaries that describes the interface between the nose raceway and roller, and support raceway and roller, respectively. Finally, F denotes the external force applied through the bearing.

The propagation and transmission captured in Equations (3.1) and (3.2) describe cases where instrumentation may be realised close to the expected source location. If this is not the case, sensors might be situated further away, and as in this case, possibly on a substructure. Herein, a recorded signal on the substructure of the nose ring essentially represents an extension of Equation (3.1), and may be characterised by

$$\hat{P}_{BL}(\mathbf{s}_{DB},\mathbf{s}_{SL},F) = \hat{D}_B\hat{W}_B(\mathbf{s}_{DB},\Gamma_{LB})\hat{T}_{LB}(F)\hat{W}_L(\Gamma_{LB},\mathbf{s}_{SL})\hat{S}_L + \hat{P}_N. \qquad (3.3)$$

Herein, $\hat{P}_{BL}$ represents the recorded response at a receiver on the nose substructure (B in Figure 3.1) of a source signal originating from the nose raceway, $\hat{D}_B$ the coupling transfer function of the receiver on the nose substructure, $\hat{W}_B$ the propagation function of the nose substructure, and $\hat{T}_{LB}$ the transmission function for the interface between the nose raceway and nose substructure. Furthermore, additional point in space $\mathbf{s}_{DB}$ indicates the location of a receiver on the nose substructure, while Γ_{LB} denotes the boundary that describes the interface between the nose raceway and nose substructure.

Similarly, a recording on the substructure of the support ring essentially represents an extension of Equation (3.2), and this signal may be characterised by

$$\begin{aligned}\hat{P}_{AL}(\mathbf{s}_{DA},\mathbf{s}_{SL},F) =& \hat{D}_A\hat{W}_A(\mathbf{s}_{DA},\Gamma_{UA})\hat{T}_{UA}(F)\hat{W}_U(\Gamma_{UA},\Gamma_{UR})\hat{T}_{RU}(F)\\ & \hat{W}_R(\Gamma_{UR},\Gamma_{LR})\hat{T}_{LR}(F)\hat{W}_L(\Gamma_{LR},\mathbf{s}_{SL})\hat{S}_L + \hat{P}_N.\end{aligned} \qquad (3.4)$$

Herein, $\hat{P}_{AL}$ represents the recorded response at a receiver on the support substructure (A in Figure 3.1) of a source signal originating from the nose raceway, $\hat{D}_A$ the coupling transfer function of the receiver on the support substructure, $\hat{W}_A$ the propagation function of the support substructure, and $\hat{T}_{UA}$ the transmission function for the interface between the support raceway and support substructure. Furthermore, additional point in space $\mathbf{s}_{DA}$ indicates the location of a receiver on the support substructure, while Γ_{UA} denotes the boundary that describes the interface between the support raceway and support substructure.

When comparing the signals on both raceways, it may be noted the relative difference between these signals is primarily the result of transmission through the roller, as long as the propagation functions for the raceways may be considered similar ($\hat{W}_L \approx \hat{W}_U$). The same holds for the relative difference between the signals recorded on the substructures. The similarity of transmission into the substructure ($\hat{T}_{LB} \approx \hat{T}_{UA}$) results from geometrical similarity of the interface. Furthermore, propagation in the substructure is characterised by bulk waves, as for mid- to high-frequency signals the wavelength is relatively short in comparison to the dimensions

of the nose and support substructures. Therefore, assuming that the reflections do not significantly interfere with the primary wave path, and excluding low-frequency signals, propagation in the substructures could be considered similar ($\hat{W}_B \approx \hat{W}_A$).

Under these assumptions, it is expected that the relative difference in the energy retained by the signal when comparing Equations (3.1) and (3.2) is in the same order as the loss for Equations (3.3) and (3.4), and for both this difference is primarily characterised by the transmission through the roller. This specific pattern may be used to identify the raceway as the origin of a source signal.

Alternatively, a sub-surface crack may be propagating in the roller, as depicted in Figure 3.2b. For this source mechanism, the detected signals at the same four sensor locations may be described as

$$\hat{P}_{LR}(\mathbf{s}_{DL}, \mathbf{s}_{SR}, F) = \hat{D}_L \hat{W}_L(\mathbf{s}_{DL}, \Gamma_{LR}) \hat{T}_{RL}(F) \hat{W}_R(\Gamma_{LR}, \mathbf{s}_{SR}) \hat{S}_R + \hat{P}_N, \tag{3.5}$$

$$\hat{P}_{UR}(\mathbf{s}_{DU}, \mathbf{s}_{SR}, F) = \hat{D}_U \hat{W}_U(\mathbf{s}_{DU}, \Gamma_{UR}) \hat{T}_{RU}(F) \hat{W}_R(\Gamma_{UR}, \mathbf{s}_{SR}) \hat{S}_R + \hat{P}_N, \tag{3.6}$$

$$\hat{P}_{BR}(\mathbf{s}_{DB}, \mathbf{s}_{SR}, F) = \hat{D}_B \hat{W}_B(\mathbf{s}_{DB}, \Gamma_{LB}) \hat{T}_{LB}(F) \hat{W}_L(\Gamma_{LB}, \Gamma_{LR}) \hat{T}_{RL}(F) \hat{W}_R(\Gamma_{LR}, \mathbf{s}_{SR}) \hat{S}_R + \hat{P}_N, \text{ and} \tag{3.7}$$

$$\hat{P}_{AR}(\mathbf{s}_{DA}, \mathbf{s}_{SR}, F) = \hat{D}_A \hat{W}_A(\mathbf{s}_{DA}, \Gamma_{UA}) \hat{T}_{UA}(F) \hat{W}_U(\Gamma_{UA}, \Gamma_{UR}) \hat{T}_{RU}(F) \hat{W}_R(\Gamma_{UR}, \mathbf{s}_{SR}) \hat{S}_R + \hat{P}_N. \tag{3.8}$$

Herein, $\hat{P}_{LR}$, $\hat{P}_{UR}$, $\hat{P}_{BR}$, and $\hat{P}_{AR}$ represent the recorded responses at receivers on the components identified by their first subscripts in Figure 3.1 of a source function on the roller, denoted by $\hat{S}_R$. Note $\hat{T}_{RL}$ represents the reverse directional form of $\hat{T}_{LR}$. Furthermore $\mathbf{s}_{SR}$ indicates the location of the source signal.

Apparent for this source is the shift towards a more symmetrical set of equations, in comparison to those for the source in the raceway. Regarding the transformations that make up the primary transmission path, Equations (3.5) and (3.6), and Equations (3.7) and (3.8) show resemblance. The geometry contains a similar symmetry in dimensioning, as depicted to-scale in Figure 3.1. This symmetry in primary transmission paths is expected to provide a basis for identifying degradation in rollers.

Lastly, for a source on the contact interface between the roller and raceway, as illustrated in Figure 3.2c, that may be due to contamination of the lubricant, the recorded signals may be described as

$$\hat{P}_{LC}(\mathbf{s}_{DL}, \mathbf{s}_{SC}, F) = \hat{D}_L \hat{W}_L(\mathbf{s}_{DL}, \mathbf{s}_{SC}) \hat{T}_{IL}(F) \hat{S}_C + \hat{P}_N, \tag{3.9}$$

$$\hat{P}_{UC}(\mathbf{s}_{DU}, \mathbf{s}_{SC}, F) = \hat{D}_U \hat{W}_U(\mathbf{s}_{DU}, \Gamma_{UR}) \hat{T}_{RU}(F) \hat{W}_R(\Gamma_{UR}, \mathbf{s}_{SC}) \hat{T}_{IR}(F) \hat{S}_C + \hat{P}_N, \tag{3.10}$$

$$\hat{P}_{BC}(\mathbf{s}_{DB}, \mathbf{s}_{SC}, F) = \hat{D}_B \hat{W}_B(\mathbf{s}_{DB}, \Gamma_{LB}) \hat{T}_{LB}(F) \hat{W}_L(\Gamma_{LB}, \mathbf{s}_{SC}) \hat{T}_{IL}(F) \hat{S}_C + \hat{P}_N, \text{ and} \tag{3.11}$$

$$\hat{P}_{AC}(\mathbf{s}_{DA}, \mathbf{s}_{SC}, F) = \hat{D}_A \hat{W}_A(\mathbf{s}_{DA}, \Gamma_{UA}) \hat{T}_{UA}(F) \hat{W}_U(\Gamma_{UA}, \Gamma_{UR}) \hat{T}_{RU}(F) \hat{W}_R(\Gamma_{UR}, \mathbf{s}_{SC}) \hat{T}_{IR}(F) \hat{S}_C + \hat{P}_N. \tag{3.12}$$

Herein, $\hat{P}_{LC}$, $\hat{P}_{UC}$, $\hat{P}_{BC}$, and $\hat{P}_{AC}$ represent the recorded responses at receivers on the components identified by their first subscripts in Figure 3.1 of a source function, denoted by $\hat{S}_C$, on the interface between the roller and nose raceway. Note $\hat{T}_{IL}$ and $\hat{T}_{IR}$ represent the transmission functions for the interface source to the respective nose raceway and roller. Furthermore $\mathbf{s}_{SC}$ indicates the location of the source signal.

The resulting set of equations is characterised as being in between the sets with the source signal in the roller or raceway, with the difference being how it incorporates transmission through the roller.

These three systems of equation show that from a combination of recordings from two sensors, of which one on the nose ring and one of the support ring, the component where the source signal originates from may be identified.

3.1.1   *Sequential Waveform-similarity Clustering*

To identify mechanisms that consistently emit elastic stress waves, such as crack growth, consistency in the source signals must be sought for. Implementation of this procedure is based on clustering signals by cross-correlation, which is defined in the time domain as

$$(s_i \star s_j)(\tau) \equiv \int_{-\infty}^{\infty} s_i^*(t)s_j(t-\tau)dt. \tag{3.13}$$

Wherein, $(s_i \star s_j)(\tau)$ represents the cross-correlation of generic source signals $s_i(t)$ and $s_j(t)$ for a specific time shift τ. Note that s^* denotes the complex conjugate of s.

The similarity index may be obtained by taking the normalised absolute maximum of the cross-correlation, i.e.

$$\varsigma_{i,j} = \max \left(\left| \frac{(s_i \star s_j)(\tau)}{\sqrt{(s_i \star s_i)(0)(s_j \star s_j)(0)}} \right| \right). \tag{3.14}$$

Herein, $\varsigma_{i,j}$ denotes the similarity between source signals $s_i(t)$ and $s_j(t)$. Note that the denominator of the fraction is composed of the product of the autocorrelations of the individual signals evaluated at $\tau = 0$, and that the autocorrelation at zero time shift is essentially the energy of the signal. The latter may also be expressed as

$$(s_i \star s_i)(0) = \int_{-\infty}^{\infty} |s_i(t)|^2 \, dt. \tag{3.15}$$

The result of Equation (3.14) is a similarity value that is contained within the closed interval $[0, 1]$, where the extreme values represent the cases of exactly identical or polar opposite signals ($\varsigma_{i,j} = 1$), or no similarity at all ($\varsigma_{i,j} = 0$).

In line with Equations (3.1)–(3.12), the procedure for cross-correlation may also be expressed in the frequency domain as

$$\mathcal{F}\left[(s_i \star s_j)(\tau) \right] = \hat{S}_i \hat{S}_j^*, \tag{3.16}$$

with $\mathcal{F}[...]$ denoting the Fourier transform.

This cross-correlation is determined based on the emitted source signals, whereas in monitoring, the recorded response at locations other than the source is obtained. The source signal is the deconvolution from the recorded response, and may be represented as

$$\hat{S}_i = \hat{Z}_i^{-1}(\mathbf{s}_D, \mathbf{s}_S, F)\hat{P}_i(\mathbf{s}_D, \mathbf{s}_S, F). \tag{3.17}$$

Wherein $\hat{Z}$ denotes the consolidation of all propagation, transmission and coupling transfer functions on the primary path from generic source location $\mathbf{s}_S$ to generic receiver location $\mathbf{s}_D$, and $\hat{Z}^{-1}$ indicates its inverse. For a consistent source location,

variation in transfer path $\hat{Z}$ can be assumed negligible for consecutive source signal emissions.

Using this, the cross-correlation of source signals may also be expressed as

$$\hat{S}_i\hat{S}_j^* = \hat{Z}_i^{-1}\hat{P}_i\left(\hat{Z}_j^{-1}\hat{P}_j\right)^* = \hat{Z}_i^{-1}\left(\hat{Z}_j^{-1}\right)^*\hat{P}_i\hat{P}_j^*. \tag{3.18}$$

Here the distributive property in convolution of the complex conjugate, and the associative and commutative properties of the convolution, allow for reorganisation of the cross-correlation into the convolution of the individual cross-correlations of the inverse transfer paths and the recorded responses.

Also considering associativity with scalar multiplication, and Plancherel's theorem on the equivalence of the integral of a function's squared modulus in the time- and frequency-domain, the normalisation may be expressed by

$$\frac{\hat{S}_i\hat{S}_j^*}{\sqrt{\int_{-\infty}^{\infty}\left|\hat{S}_i\right|^2 d\omega \int_{-\infty}^{\infty}\left|\hat{S}_j\right|^2 d\omega}}$$

$$= \frac{\hat{Z}_i^{-1}\left(\hat{Z}_j^{-1}\right)^*}{\sqrt{\int_{-\infty}^{\infty}\left|\hat{Z}_i^{-1}\right|^2 d\omega \int_{-\infty}^{\infty}\left|\hat{Z}_j^{-1}\right|^2 d\omega}} \frac{\hat{P}_i\hat{P}_j^*}{\sqrt{\int_{-\infty}^{\infty}\left|\hat{P}_i\right|^2 d\omega \int_{-\infty}^{\infty}\left|\hat{P}_j\right|^2 d\omega}}. \tag{3.19}$$

The similarity is defined as the absolute maximum of the normalised cross-correlation in the time domain. Therefore the inverse Fourier transform is used to return to the time-domain. Herein, the convolution theorem allows for the separation of the $\hat{Z}$ and $\hat{P}$ terms in separate inverse transformations, as

$$\mathcal{F}^{-1}\left[\frac{\hat{S}_i\hat{S}_j^*}{\sqrt{\int_{-\infty}^{\infty}\left|\hat{S}_i\right|^2 d\omega \int_{-\infty}^{\infty}\left|\hat{S}_j\right|^2 d\omega}}\right]$$

$$= \mathcal{F}^{-1}\left[\frac{\hat{Z}_i^{-1}\left(\hat{Z}_j^{-1}\right)^*}{\sqrt{\int_{-\infty}^{\infty}\left|Z_i^{-1}\right|^2 d\omega \int_{-\infty}^{\infty}\left|Z_j^{-1}\right|^2 d\omega}}\right]$$

$$* \mathcal{F}^{-1}\left[\frac{\hat{P}_i\hat{P}_j^*}{\sqrt{\int_{-\infty}^{\infty}\left|\hat{P}_i\right|^2 d\omega \int_{-\infty}^{\infty}\left|\hat{P}_j\right|^2 d\omega}}\right], \tag{3.20}$$

with $*$ denoting the convolution operator.

Under the assumption of near-identical transfer paths ($\hat{Z}_i^{-1} \approx \hat{Z}_j^{-1}$), causality imposes that the argument of the maximum cross/auto-correlation (i.e. the time shift) of the inverse transfer paths is the same as the argument of the maximum cross-correlation of the source signals and as the argument of the maximum cross-correlation of the recorded signals. Since only the maximum is of concern for the similarity index, the cross-correlation of the transfer paths may be omitted from the equation, as the maximum of its normalised cross-correlation is equal to one,

due to it being an auto-correlation in case of near identical transfer paths. Then the similarity index may be expressed as

$$
\begin{aligned}
\varsigma_{i,j} &= \max \left(\left| \mathcal{F}^{-1} \left[\frac{\hat{S}_i \hat{S}_j^*}{\sqrt{\int_{-\infty}^{\infty} \left|\hat{S}_i\right|^2 d\omega \int_{-\infty}^{\infty} \left|\hat{S}_j\right|^2 d\omega}} \right] \right| \right) \\
&\approx \max \left(\left| \mathcal{F}^{-1} \left[\frac{\hat{P}_i \hat{P}_j^*}{\sqrt{\int_{-\infty}^{\infty} \left|\hat{P}_i\right|^2 d\omega \int_{-\infty}^{\infty} \left|\hat{P}_j\right|^2 d\omega}} \right] \right| \right).
\end{aligned}
\tag{3.21}
$$

From the similarity between signals, the dissimilarity may be defined as

$$
\delta_{i,j} = 1 - \varsigma_{i,j}.
\tag{3.22}
$$

This dissimilarity $\delta_{i,j}$ represents the virtual distance in the clustering algorithm.

To identify structure in signal (dis)similarity, a particularly suitable approach is agglomerative hierarchical clustering (AHC), of which implementations by Van Steen et al. [29] and Huijer et al. [34] are illustrative. This bottom-up approach links signals by increasing dissimilarity, to generate a dendrogram that shows the connectivity of all elements of the dataset. From the dendrogram, clusters may be obtained – amongst other procedures – by cutting the branches at a certain dissimilarity threshold.

A downside of AHC – and many other clustering approaches – is the requirement to have all of the data known at the beginning of the procedure, hindering on-line implementation. Also the requirement to know the distances between all data points, makes it less suitable for large data-sets. Alternative sequential, or incremental, algorithms have been proposed, for which the general procedure is to compare each new signal to the already formed clusters, and to assign said signal to either one of those clusters or assign it as a new cluster [120]–[123].

A basic sequential clustering algorithm is implemented that is particularly aimed at clustering highly-similar signals. The following procedure is adopted: In order of detection, each signal is first compared to all already identified clusters – in case there are none yet, this step is omitted. If the dissimilarity between the evaluated waveform and any existing cluster is lower than a predetermined threshold, the waveforms gets associated with the cluster of lowest dissimilarity. If no cluster of sufficiently-low dissimilarity is identified, a second comparison to the sample of other non-clustered waveforms takes place. If in this second comparison a sufficiently low dissimilarity is observed, the waveforms with the lowest similarity will together form a new cluster. If in no comparison the dissimilarity threshold is met, the evaluated waveform gets assigned to the sample of non-clustered waveforms. This procedure is graphically illustrated in Figure 3.3.

To reduce the computational burden, only a limited sample of waveforms is compared for each cluster and for the non-clustered waveforms. In case of the latter, a moving window is utilised that only considers the last 250 signals that were assigned non-clustered. The reasoning being that more recent signals are more likely to meaningfully correlate to each other. The same reasoning has also been used to implement a procedure that declares clusters as dormant after 250 consecutive unsuccessful comparisons, to eliminate needless comparisons to a significant portion
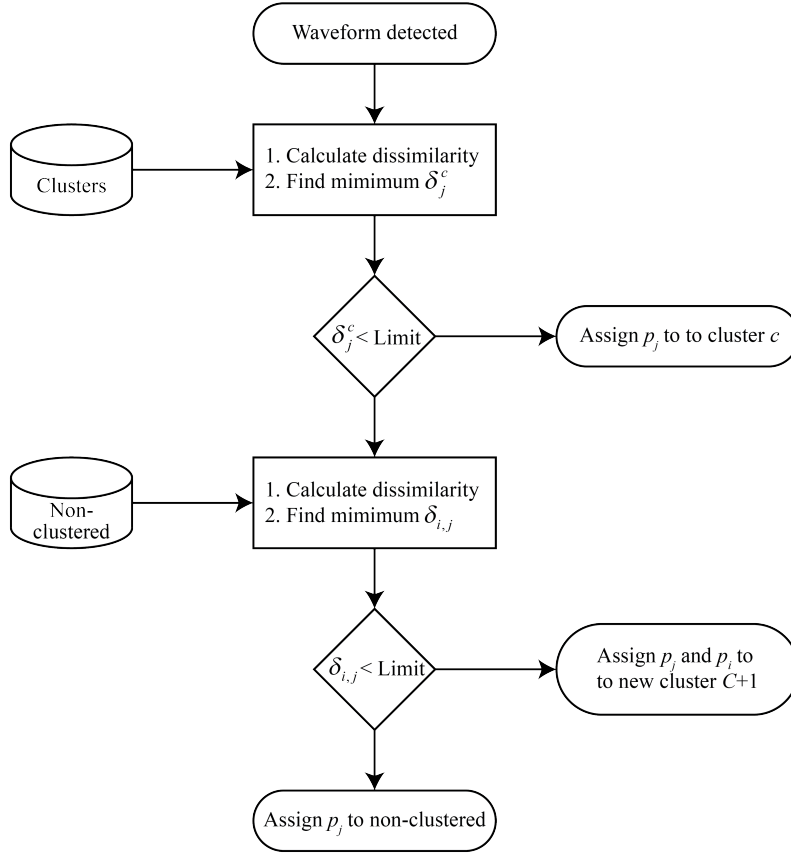
Figure 3.3: Overview of the procedure for AE signal clustering.

of insignificant clusters composed of only a few hits. Clusters larger than 50 hits are excluded from the dormancy check. For each cluster, a sample of up to nine waveforms is selected. To suitably represent the cluster as a whole, the sample contains some of the very first, some of the very last, and some arbitrary signals from the cluster. Due to the use of a low dissimilarity threshold, the high similarity within the cluster assures any selection from the cluster represents the cluster as a whole.

For the comparison of waveforms to clusters, a weighted average dissimilarity measure is used. Weighing is applied to increase the importance of newer additions to the cluster, and decrease the importance of the original waveforms. This improves the resilience of the clustering approach to slight and gradual changes of the clustered signals, which may occur due to the influence that the degrading geometry might have on the transmission of the source signal. To determine the weighted average the approach uses

$$\delta_j^c = \frac{\sum\limits_{i=1}^{N} w_i \delta_{i,j}}{\sum\limits_{i=1}^{N} w_i}, \tag{3.23}$$

wherein δ_j^c indicates the average dissimilarity between waveform p_j and cluster c, and w_i the weight factor associated with waveform p_i. The summation is performed over N waveforms p_i, that are elements of cluster c.

3.2   RUN-TO-FAILURE EXPERIMENT ON A TURRET BEARING MOCK-UP

A test set-up that is representative of a segment of a large-scale slew or turret bearing has been utilised. It consists of a double linear bearing, which, under vertical load applied through the support rings, allows for cyclic horizontal movement of the nose ring. The illustrations in Figure 3.1 show the top half of the designed set-up. The bottom half is an exact vertically-mirrored copy of the top half, with both halves separated by a fibre-reinforced composite panel for improved ultrasonic isolation. A picture of the set up with a three-roller configuration prior to the application of grease is shown in Figure 3.4. Note that the same set-up has also been used in Scheeren and Pahlavan [124] for different experiments on low-speed roller bearings.

Figure 3.4: Picture of turret bearing test set-up with cover plates removed.

The raceways, rollers, and cages are all modular components. The experiment described in this work uses in each half of the setup two raceways with a thickness of 32.5 mm made out of Hardox 600, two rollers with diameter of 69 mm made out of 100Cr6 through hardened bearing steel, and a cage made out of CuSn12C tin bronze. Out of the notable permanent components, the nose and support substructures are all made out of S355J2 structural steel. The main dimensions of the set-up, as indicated in Figure 3.1, are given in Table 3.1.
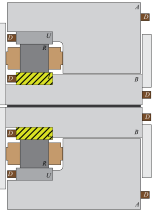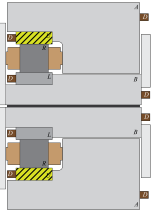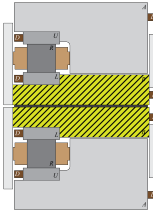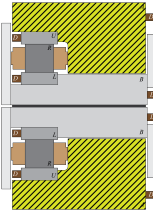
Table 3.1: Main dimensions of the turret bearing test set-up. Reference for dimensions is made to Figure 3.1.

Quantity	d_R	h_A	h_B	l_A	l_B	w_A	w_B	w_R
Dimension [mm]	69	187	97.5	495	795	350	358	69

3.2.1 *Acoustic Emission Instrumentation*

Ultrasonic signals generated over the course of the natural degradation test have been recorded in the frequency range of 40–580 kHz. To achieve this, the set-up has been instrumented on eight locations with three types of commercial piezoelectric AE transducers. An overview of the locations and sensor types of all measurement channels is given in Table 3.2.

Table 3.2: Overview of turret bearing test set-up measurement channels.

T - Top half B - Bottom half	Nose Raceway	Support Raceway	Nose Substructure	Support Substructure
Low-frequency 40–100 kHz	T-Ch. 20 B-Ch. 2	T-Ch. 19 B-Ch. 1	T-Ch. 14 B-Ch. 8	T-Ch. 13 B-Ch. 7
Mid-frequency 95–180 kHz	T-Ch. 22 B-Ch. 4	T-Ch. 21 B-Ch. 3	T-Ch. 16 B-Ch. 10	T-Ch. 15 B-Ch. 9
High-frequency 180–580 kHz	T-Ch. 24 B-Ch. 6	T-Ch. 23 B-Ch. 5	T-Ch. 18 B-Ch. 12	T-Ch. 17 B-Ch. 11
Graphical representation of measurement location (indicated by hatching pattern)				

The eight measurement locations are split between the two mirrored test chambers. The isolation in the middle of the nose ring allows for these to be considered acoustically independent from one another. Within the sphere of influence of each chamber, the measurement locations can be identified by a combination of two binary groups. Each array is situated either on the raceway, or the substructure, and that component is part of either the nose ring, or the support ring. The illustrations in Figure 3.1 is representative of the measurement locations for the top chamber, while for the bottom chamber the locations are vertically mirrored.

The eight measurement locations all represent arrays of three sensors – each of which sensitive to a specific part of the considered frequency range. Low frequencies are covered by a 60 kHz resonant R6α, mid frequencies by a 150 kHz resonant R15α, and high frequencies by a broadband WSα – all manufactured by Physical Acoustics Corporation. All of the sensors are amplified by external AEP5H pre-amplifiers set to a gain of 40 dB, before being connected to a 24 channel AMSY-6 acoustic emission measurement system fitted with ASIP-2/A signal processing cards – both

manufactured by Vallen Systeme. Digital band-pass filters are applied for each sensor type individually to separate low-, mid- and high-frequency content. For the low-frequency measurement channels a band-pass filter from 40–100 kHz is set, for the mid-frequency 95–180 kHz, and for the high-frequency 180–580 kHz.

Whenever a 50 dB threshold was crossed – set to accommodate the ultrasonic background encountered in the set-up in operation – a transient recording of 812 µs sampled at 5 MHz and the extracted feature-data are stored. The transient-data contains a 200 µs pre-trigger recording to capture the onset of the detected signal prior to crossing the threshold.

3.2.2   *Experimental procedure*

An arrangement of two rollers is subjected to a vertical load of 1215 kN, while a horizontal stroke of 70 mm is cycled through every 12 s for a linear speed of about 0.012 m·s⁻¹. The test is expected to continue for 230,000 cycles (approximately 770 hours). During the test, the set-up is lubricated daily with Interflon LS1/2 heavy duty grease. To compensate for slipping, the rollers and cages in the set-up are repositioned whenever they have travelled more than 45 mm from the centred position.

Over the course of the test six inspections are performed at (i) ~51,000 cycles, (ii) ~138,000 cycles, (iii) ~166,000 cycles, (iv) ~196,000 cycles, (v) ~211,000 cycles, and (vi) ~225,000 cycles (end of test). Inspections primarily constituted visual observation, additionally wear depth, roughness (for rollers and raceways), and roundness (for rollers) were measured.

3.2.3   *Noise Filtering*

In pre-processing, two additional procedures for filtering are implemented. These are a signal-to-noise ratio (SNR) filter and a position filter.

Noisy signals are less likely to be clustered when a low dissimilarity threshold is set. Therefore, to remove these noisy signals, an SNR-based filter is implemented. This filter compares the peak amplitude in a 100 µs window before detection to the peak amplitude of the signal. A minimum SNR of 10 (20 dB) is imposed.

To mitigate for signals generated by collisions related to the small gaps between components while cycling, and in particular when reversing the direction, a position based filter is implement. This filter separates all signals that occur within 2.5% of the start or the end of the horizontal stroke.

3.3   TURRET BEARING MOCK-UP RUN-TO-FAILURE RESULTS AND DISCUSSION

A total of approximately 225,000 cycles were performed under a load of 1215 kN. After the test, severe wear of the raceways in both the top and bottom chamber were observed. This wear is primarily present in the form of increased surface roughness and grooving, while additionally some slight pitting is observed. Both top and bottom chambers (Figure 3.4 for reference) generally show a similar severity of wear, however, in each chamber the lower raceway was worn significantly more than the

upper raceway. The rollers generally show wear that is comparable in severity to the upper raceways. Five additional inspections have been performed over the course of the experiment, these observations will be discussed in parallel to the hit-rate observed over the course of the experiment.

An extensive number of ultrasonic signals have been recorded during the experiment. Some damages were also incurred by the sensor system. These damages were primarily sustained in the bottom chamber, where the mid-frequency and broadband sensor were broken off the raceway.

In extension and retraction the valve system of the horizontal cylinder emits a continuous low-frequency noise, that could be detected by the low-frequency receiver on the support substructure of the bottom half of the set-up. The recorded signals for this receiver show a continuous consistent alternation between six seconds of increased noise, and a short period of reduced noise. This patterns has been used identify movement of the nose ring, and subsequently filter for 2.5% of the nominal stroke in time. About 98.5% of the cycles could be detected using this procedure. In further processing, the valve-initiated signals are rejected by the SNR filter.

Limiting the analysis to the top chamber, a total of ~2,300,000 AE signals have been detected that pass through the SNR and start-stop filters. The ultrasonic activity, represented in form of hit-rate per cycle (i.e. extension and retraction of the horizontal cylinder), is shown in Figure 3.5, of which the middle two graphs display the channels on the raceways, and the outer graphs display the channels on the substructure. Note that channel 14 detected no signals (that are not removed by the filters) over the course of the experiment. An arbitrary selection of three waveforms from each of the measurement channels on the top chamber of the set-up is depicted in Figure 3.6.
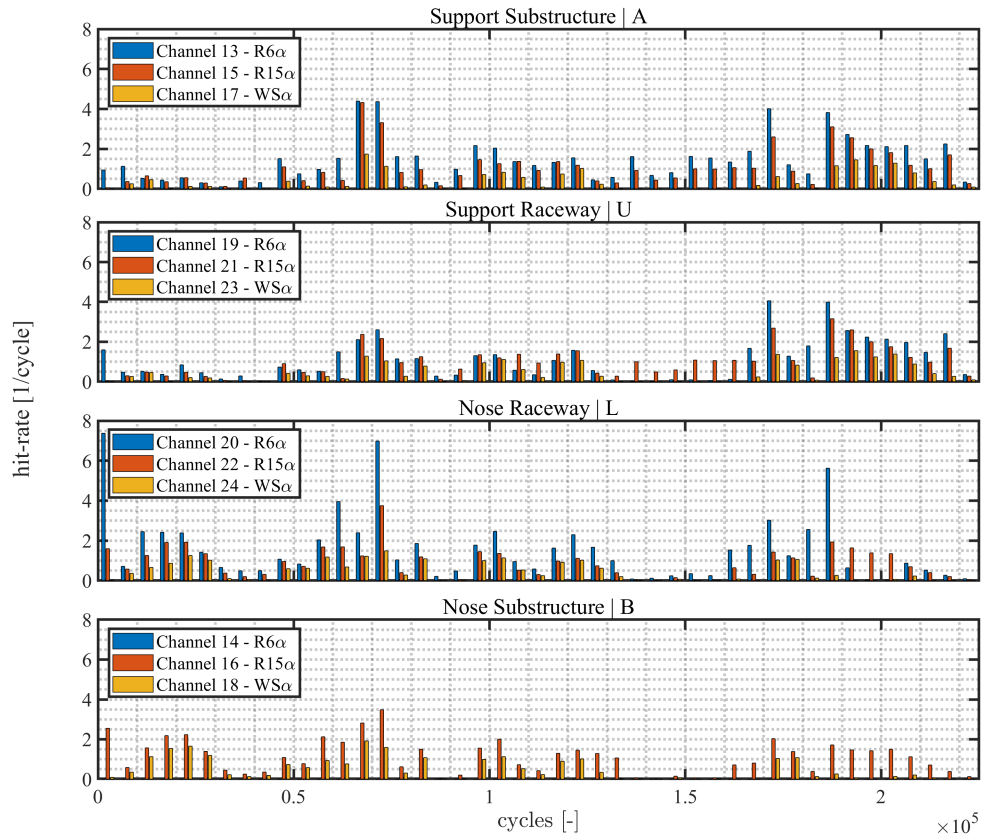
Figure 3.5: Ultrasonic activity in the top chamber separated in graphs per location: support substructure (top), support raceway (upper-middle), nose raceway (lower-middle), and nose substructure (bottom).
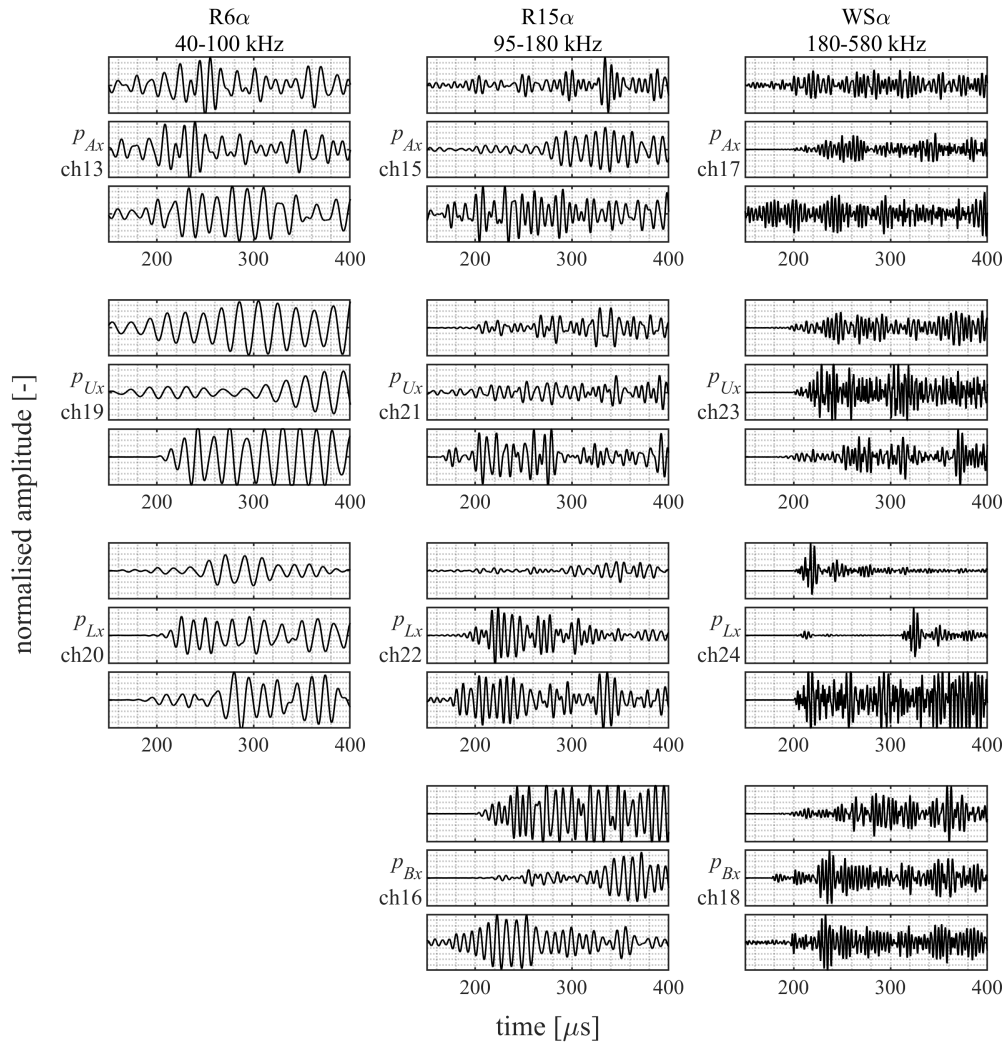
Figure 3.6: Overview of an arbitrary selection of waveforms recorded on the top chamber.

Considering Figure 3.5, it seems that from around 70,000 cycles the activity on both raceways increases, possibly related to some form of more significant degradation. A comparable trend can also be observed in the substructure channels. Later on, another significant rise in activity is observed at around 170,000 cycles.

Also of note is an earlier increase in activity around 20,000 cycles on the nose raceway and substructure. Contrasting the later observations of increased hit-rate, this increase is not detected on both of the raceways. As such it either originates from a weak source mechanism, or from an external source of noise. Based on a comparison between the detection on the raceway and substructure, it is expected to be the latter.[1]

These crude observations in the hit-rates are complemented by intrusive inspections. At 51,000 cycles, the first inspection suggested no significant damage and only

---

1 The bearing condition index (BCI) introduced in Chapter 4 has been applied to the data presented in this chapter. The results presented in Appendix D further support this conclusion.

slight contamination of the grease was present. For the second inspection at 138,000 cycles – after the first significant increase in hit-rate – wear particles were observed throughout the set-up, and the raceways showed excessive wear at the contact area. These observations together with the detected ultrasonic activity suggest that the onset of this wear took place at around 70,000 cycles.

During the third inspection at 165,800 cycles, an increase in the surface roughness of the raceways was observed. Shortly after this observation, AE activity peaked with hit-rates reaching up to 5 detected signals per cycle. Just before the next inspection at 196,300 cycles, activity peaked yet again, with hit-rates again reaching up to 5 hits per cycle. During this inspection, light pitting was observed on the rollers, and the roughness had increased further for both rollers and raceways. For the fifth inspection, around 211,000 cycles, further development of the wear was reported. And the final inspection, at the end of the 225,000 cycles, reported no significant changes compared to the fifth inspection. Several pictures of the resulting degradation of the nose raceway at the end of the experiment are included in Figure 3.7.

Figure 3.7: Pictures of the post-experiment inspection of the nose raceway, showing; (a) overall wear pattern comprising increased surface roughness (discolouration), pitting, and grooving, (b) close-up of grooving and surface deterioration at the lower edge in (a), and (c) close-up of grooving and surface deterioration at the upper edge in (a).

Overall, it can be concluded that the biggest changes in the observed damage during the inspections match the significance of ultrasonic activity that has been detected. Notable though is that the reported contamination does not seem to cause excessive AE activity.

To identify possible patterns in the ultrasonic activity, the clustering procedures described in Section 3.1.1 have been implemented in in-house code developed for MATLAB R2022a. For each of the measurement channels, the 100 largest clusters have been evaluated, and based on common trends among different channels, two structures of significant clusters have been identified. These structures of clusters are shown in Figure 3.8 and Figure 3.10, and seem to be related to the significant increase in activity that is observed in Figure 3.5 at around 170,000 cycles and 190,000 cycles.

The largest structure of clusters is the one that was encountered between 170,000 cycles and 180,000 cycles, as shown in Figure 3.8. An arbitrary selection of three illustrative waveforms from each of the measurement channels comprising this structure of clusters is depicted in Figure 3.9. The structure is composed of about 77,000 AE hits that are detected by 11 of the 12 sensors present on that half of the set-up. The average similarity of each waveform to its respective cluster is 0.93, highlighting the concept of consistent signal generation and propagation. The most noticeable averaged activity reaches up to 2 hits per cycle in the mid-frequency range. Comparing this to the hit-rates shown in Figure 3.5, suggests that the clusters in the structure make up about half of the activity for the hit-rate peak between 170,000 cycles and 180,000 cycles. The rest of the activity is likely to be attributed to less consistent degradation mechanisms, such as wear and contamination.

For some of the measurement channels, the structure is split between multiple clusters. Notable examples – that are also elucidated in Figure 3.9 – are the selected clusters for channels 19 and 20. In Figure 3.8 the amplitude trends of the individual hits composing these clusters clearly match the overarching trend, however, in Figure 3.9 the waveforms are shown to contain some minor differences – in particular near the onset – which have likely resulted in a close-miss for the clustering approach. Eventual fine-tuning of the dissimilarity threshold could alleviate this occurrence, however, for the purpose of this study this is omitted.
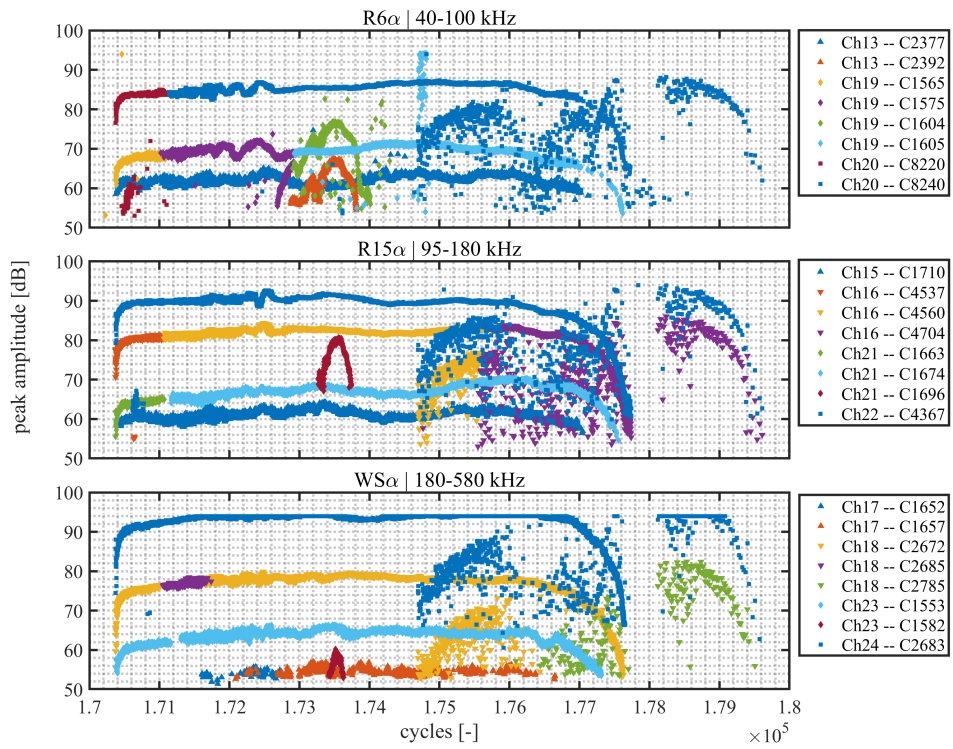
Figure 3.8: Primary structure of selected clusters from low- (top), mid- (middle), and high-frequency (bottom) measurement channels.
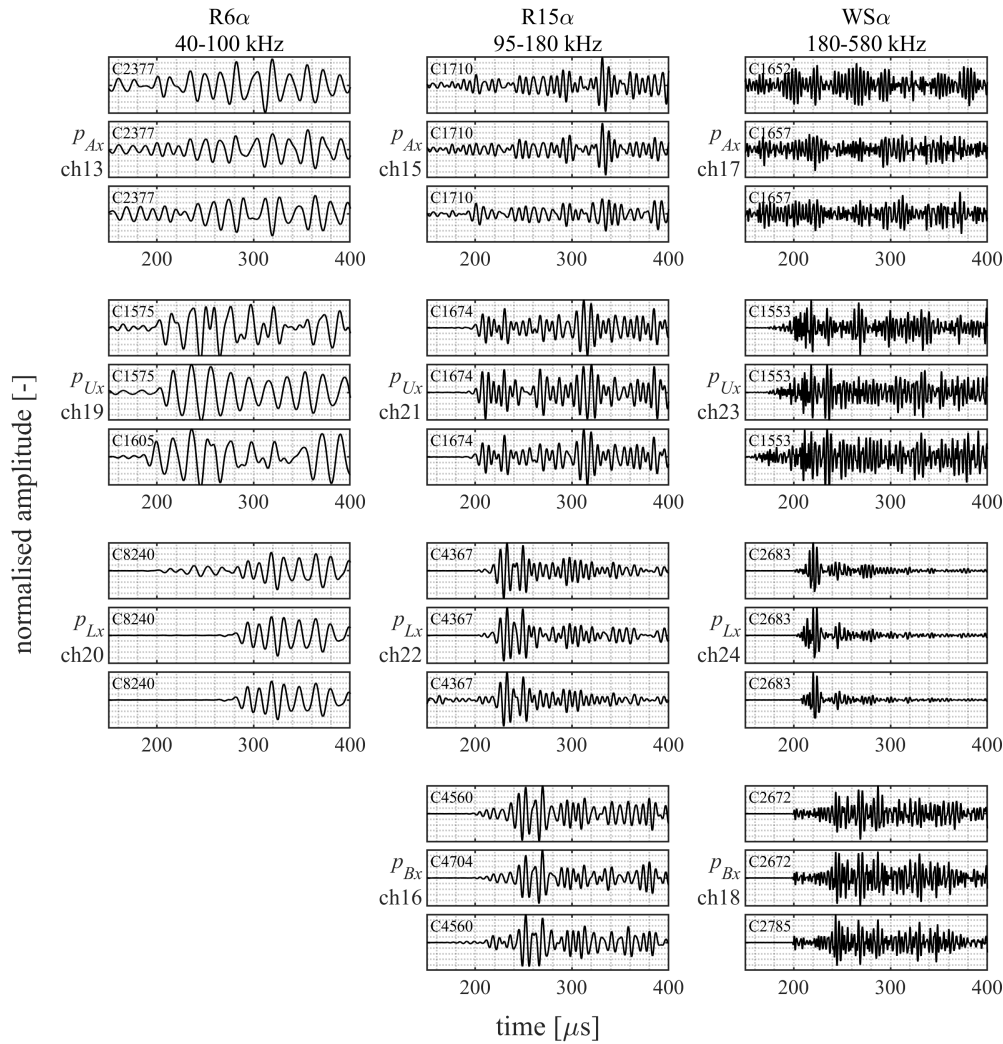
Figure 3.9: Overview of an arbitrary selection of waveforms associated with the primary structure of clusters.

In general, the primary structure of clusters seems to comprise two trends. There is a clear line of highly-similar hits with amplitudes near equal to the neighbouring hits. This trend seems to be present for a duration of 7,500 cycles, and is detected and clustered for nearly all of the measurement channels. The second trend shows a more cloudy behaviour, with greater variance in the detected peak amplitudes, though waveforms remain highly-similar. Overall, amplitudes for the second trend seem less pronounced, and therefore it is detected and clustered to a lesser extend in comparison to the first trend. The second trend is present for a duration of 5,000 cycles, with the onset just before 175,000 cycles.

Focussing on the highly-consistent line-shaped trend, the source of the signals and thus the location of the degradation can be derived. The basis for this derivation is the systems of transformations described in Equations (3.1)–(3.12). Taking the mid-frequency graph as an example, the greatest amplitudes are detected on the

nose raceway (channel 22, cluster 4367) at around 90 dB. On the opposing raceway (channel 21, clusters 1663 and 1674), an amplitude of about 65 70 dB is detected. The difference between these locations is a drop in amplitude of 20–25 dB, that matches the results obtained in Chapter 2 on the relative drop in amplitude for a signal propagating from one raceway to another through a roller. Similarly, the differences between the raceway and substructure channels are shown to be in the order of 5–10 dB. These numbers are slightly better than predicted in the previous chapter for a single interface transmission, however, it must be noted those experiments assumed a line contact, whereas the interface between raceway and substructure is a surface.

Comparable differences in amplitudes can also be observed in the low- and high-frequency graphs in Figure 3.8, however, the roller transmission for the low-frequencies seems a bit stronger, at about 20 dB amplitude loss. While the high-frequencies show a slightly weaker transmission, at about 30 dB amplitude loss.

Regarding the cloud-like trend observed around 175,000 cycles, it must first be stated that these are the same clusters that comprise the line-shaped trend. This is most obvious when looking at the cluster for channel 22 (cluster 4367 in the middle graph of Figure 3.8), which contains both the line-shaped trend with the greatest amplitudes among the line-shaped trends, and the cloud-shaped trend with generally the greater amplitudes among the cloud-shaped trends. These being in the same cluster indicates that these seemingly separate trends share highly-consistent waveforms, with the only significant difference between them being the consistency of the amplitude. The signals in the line-shaped trend show a minimal and gradual variation in the amplitudes, indicating that the emission mechanism consistently releases similar amounts of energy into the material with each hit. Contrasting to this is the cloud-shaped trend, where the variation in amplitude between the signals indicates a varying amount of energy released into the material for each hit.

Concluding, all of the identified clusters in the largest structure of clusters seem to indicate that degradation is developing in the nose raceway of the top chamber. This degradation is mostly of a highly-consistent nature, which might indicate some form of crack propagation.

The secondary structure of clusters, shown in Figure 3.10, is encountered between 184,400 cycles and 186,400 cycles. An arbitrary selection of three illustrative waveforms from each of the measurement channels comprising this structure of clusters is depicted in Figure 3.11. The structure is composed of about 13,500 AE hits that are detected by 9 of the 12 sensors. The average similarity of each waveform to its respective cluster is 0.94. The most noticeable averaged activity reaches just upwards of 1 hit per cycle. Comparing this to the hit rates shown in Figure 3.5, the clusters in the structure make up about a quarter of the activity during its duration of some 2,000 cycles. As was the case with the other structure of clusters, residual activity is likely related to mechanisms emitting less consistent waves.
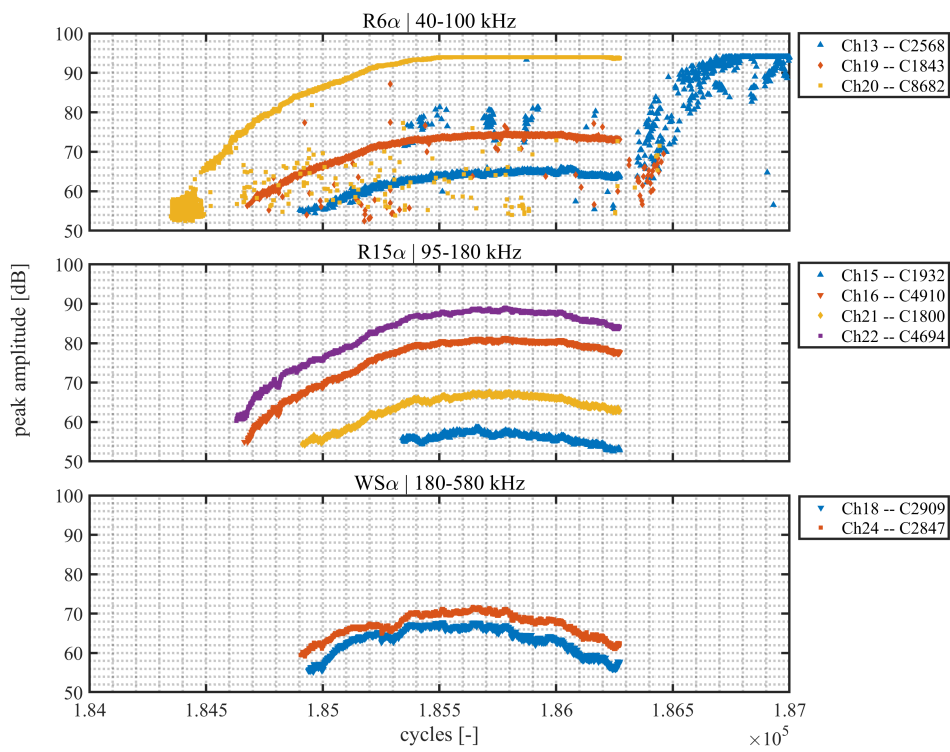
Figure 3.10: Secondary structure of selected clusters from low- (top), mid- (middle), and high-frequency (bottom) measurement channels.
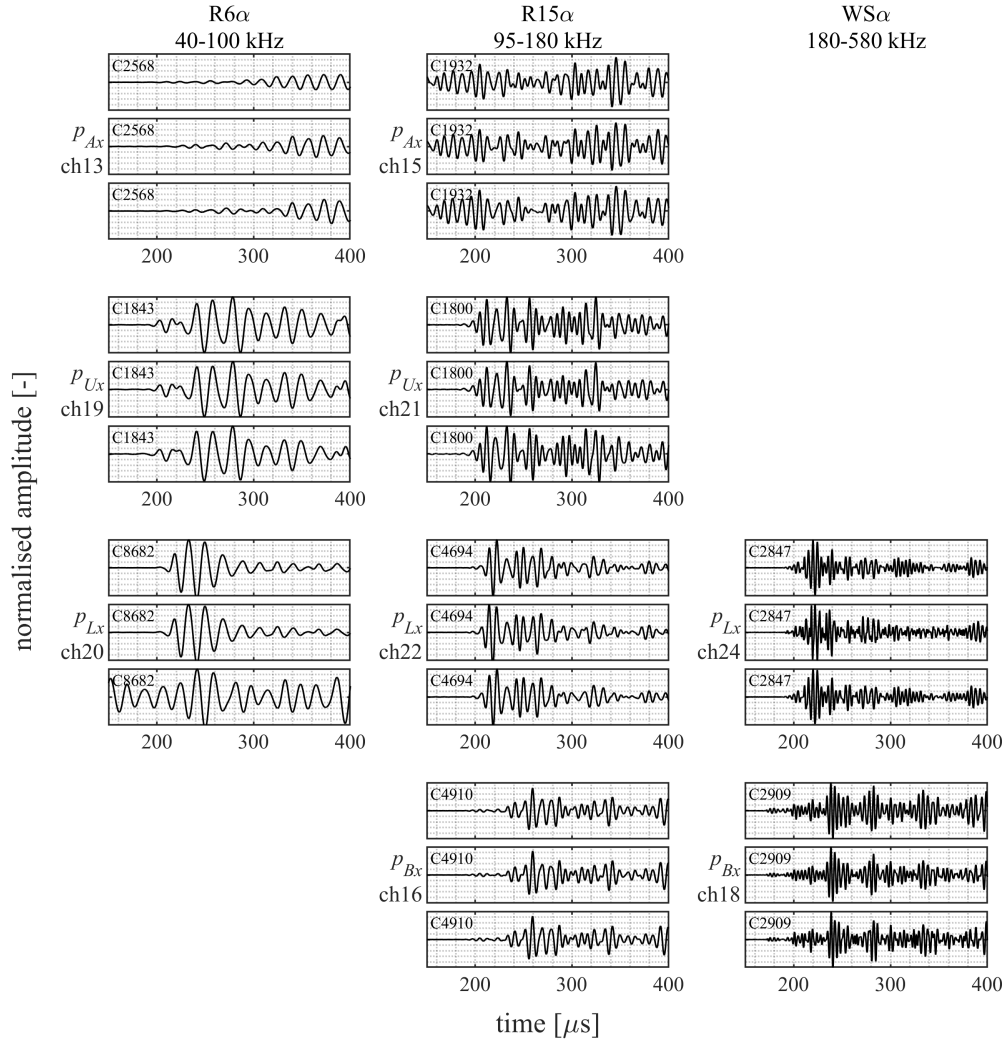
Figure 3.11: Overview of an arbitrary selection of waveforms associated with the secondary structure of clusters.

The individual clusters, that have been selected to compose this structure, all show a clear trend of hits with a consistently increasing and subsequently decreasing amplitude. Using the reasoning introduced earlier regarding interfaces and transmission losses, it is expected that the secondary structure of clusters comprises signals that were generated in the nose raceway, as was the case with the primary structure of clusters. These observations, the similar trend in emission behaviour and the same source component, imply that the degradation responsible for both structures of clusters might be of similar character. Seemingly contradicting is the notion that the separate clustering of the individual hits in both structures of clusters, is the result of dissimilarity between the clusters within the structures. However, progressive failure of the rolling elements alters transfer paths and transmission surfaces, and as such deviation of the long-term similarity is expected with increasing damage, while the short-term similarity is retained. Note that separation of larger clusters into several

smaller ones may obfuscate the identification of particular types of degradation and is to be further investigated in the future research regarding long-term tracking of particular clusters.

Manual identification of structures in the obtained clusters, as performed prior, is a laborious process. The visualisation of clusters in Figures 3.8 and 3.10 has been limited to the largest 100 clusters for this reason. To improve the efficiency and minimize the risk of data misinterpretation, common techniques for structuring multi-channel AE data, such as event-building, may be implemented. A basic implementation of this combined event and cluster-based filtering is presented in Figure 3.12. Therein the global cumulative hit-count is shown for all hits that meet the criteria of being associated with (i) a cluster containing at least 100 elements, and (ii) an event that has been detected by all of the sensor types and on at least two of the measurement locations individually.

Figure 3.12 shows four graphs, each representing the three sensor types on a particular measurement location. The visual similarity in the trends is obvious, indicating that most commonly the identified clusters are detectable on all measurement
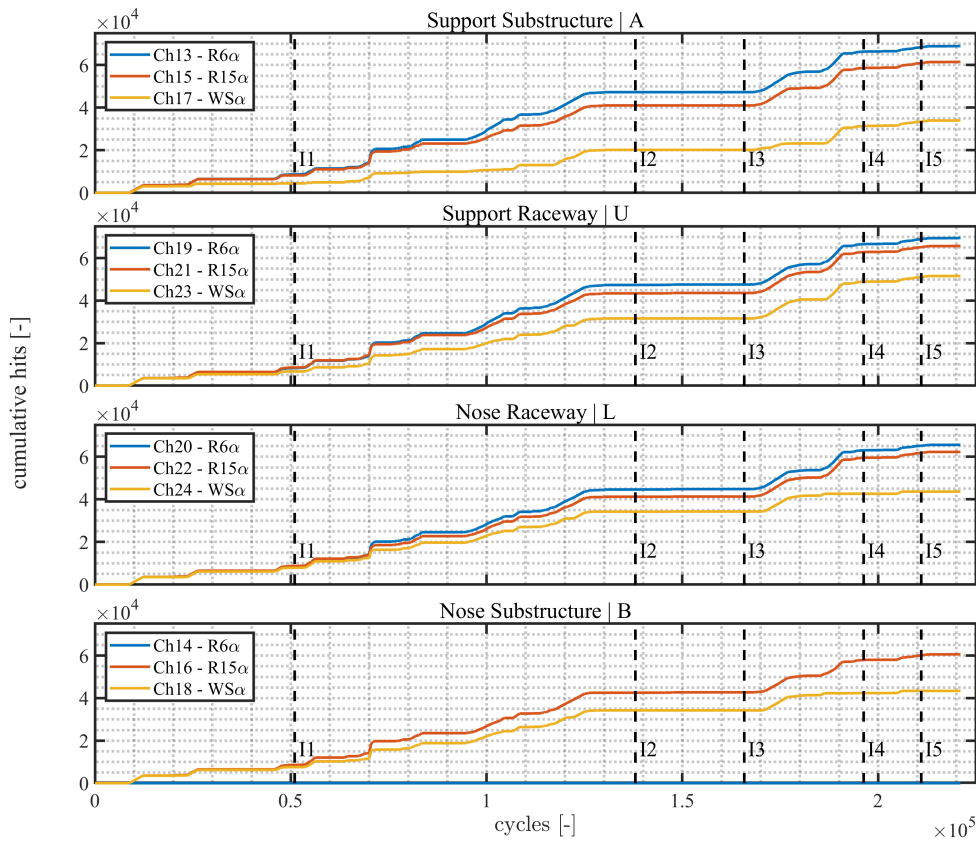

Figure 3.12: Cumulative hit-count in the top chamber filtered for (i) the detectability of the event in both at least three frequency ranges and at least two measurement locations, and (ii) the association with a cluster comprising at least 100 elements. The dashed vertical lines (I1–I5) indicate the five performed inspections.

locations. Note that the prescribed association in the event building procedure does partly impose this similarity in the trends, however, this is limited to a fraction of the measurement channels. The overall similarity in the trends indicates the feasibility of condition monitoring on the basis of propagated signals.

The trends in all four graphs of Figure 3.12 show the major rises in the cluster-event filtered cumulative hit-count to be occurring between the first (I1) and second (I2) inspection, and between the third (I3) and fourth (I4) inspection. The monitoring results from both of periods comply with the observations of increased wear. Considering the structures of clusters shown in Figures 3.8 and 3.10, the two separately-identifiable increases in hit-count between I3 and I4 are associated with the structures presented in those respective figures. However, the continuation of the later of these increases till around 190,000 cycles indicates that a part of these clusters have gone unnoticed in the manual identification. The same limitation should be extended to the rise in hit-count between I1 and I2, of which none of the underlying structures was identified in the manual evaluation. Therefore, this implementation demonstrates the effectiveness of combined clustering and event-building in isolating potentially significant AE activity.

The presented methodology in this work has been supplemented with a complete and extensive data sample covering the entire degradation process of the rolling elements. If fewer data is available, the reliability of the identification approach may be reduced. In future research the minimum required data sample from which to reliably infer bearing condition is to be investigated. Furthermore, the reported experiments represented a moderately-noisy environment. It is recognised that higher-noise environments might exist in practical situations subject to harsh working conditions and thus may require more elaborate noise countering measures. In future work application of the proposed methodology on representative installations and possible associated challenges in the field will be investigated.

3.4 CONCLUSIONS

A methodology for identifying degradation in low-speed roller bearings based on similarity of AE source signals and a sequential clustering algorithm based on cross-correlation of recorded AE signals is proposed. The possibility of utilising propagated and transmitted signals instead of source signals is discussed and formulated analytically. To verify the methodology, a natural degradation test has been executed in a representative scale on a purpose-built linear bearing segment modelled after the support bearing of an FPSO turret. Over the course of approximately 225,000 cycles, wear – comprising erosion, pitting and surface roughening – and possible surface initiated fatigue – comprising larger pitting near the edge of the rolling surface – were developed. Acoustic emissions have been recorded at four locations both on the rolling elements and on the supporting structure by sensor arrays comprising of three AE transducers, each sensitive to a particular part of the covered 40–580 kHz frequency range. The recorded signals have been filtered and clustered, to identify consistent trends and structures that may indicate developing degradation. Analysis of the clustered signals shows an increase in similar emissions around 70,000 cycles that is likely indicative of an increase in the degradation rate. This increased wear development is supported by visual inspections of the rolling

elements. Additionally, around 175,000 cycles, two highly-consistent structures of clusters have been observed to originate from the nose raceway, which may be indicative of the development of a localised defect in that raceway. These results suggest that (i) clustering based on cross-correlation may be used to identify consistency in AE source mechanisms, (ii) combined clustering and event-building provides an effective method for isolating significant AE activity, (iii) for sufficiently low-speed, propagation and transmission of AE signals throughout the rolling elements, interfaces, and substructure is governed by (quasi-)static attenuation, and (iv) relative differences between clusters identified for different sensor locations may be used to identify the component the source signal originates from.

4

BEARING CONDITION & DEGRADATION RATE INDICES

This chapter is based on [125]:

B. Scheeren and L. Pahlavan, *Monitoring integrity of low-speed bearings using acoustic emission*, The Netherlands Patent N2032270, 2023. (pending)

ABSTRACT

This chapter presents the bearing condition index (BCI) as a warning indicator to judge the hit-rates of source mechanism identified AE signals. A run-to-failure experiment is conducted with a bogie wheel bearing to validate the proposed BCI. The results suggest the BCI is an effective and intuitive indicator of the bearing condition.

The repetitivity of acoustic emission signals forms the central pillar on which the proposed method of condition monitoring is built. Over the course of the degradation of a structure or material, the accumulation of slight progressions in the damaged state instigates an accumulations of acoustic emission generated by them. As such AE condition monitoring inherently involves trends and statistics, with the crux being the interpretation of these to differentiate between operable and early-stage-defect states.

In literature, common approaches of detecting these periodic damage-induced signals are known as cyclostationary techniques [13], [126]. These techniques specify unique damage frequencies for the specific components of a roller bearing. These typically include frequencies for faults in the inner and outer raceways, rollers, and cages, that are based on the bearing geometry and the speed of rotation. For detection of the frequencies in recorded AE time-series, usually (short-term) frequency or time-frequency transformations are used, wherein excessive energy nearby a fault frequency is used as an indication [12]. For the types of bearings considered in this work, two limitations of cyclostationary techniques exist. The first is that a variable speed of the bearing requires complicated correction in the detection procedure to mitigate the varying fault frequencies [127]. The second

is that at very-low speeds the spurious environmental noise signals are relatively more common due to the lower occurrence of the repetitive damage signals. For these reasons, an alternative indicator must be established. This indicator is to unify the identification approach presented by Chapter 3 and a normalisation principle founded on cyclostatonarity in roller bearings.

This chapter discusses the development of a bearing condition index (BCI), which constitutes a quantitative measure of the current condition of a bearing. First, normalisation of the AE hit-rate is discussed, followed by the proposal of the BCI and derived degradation rate index (DRI). Second, a test case is introduced in which a pre-damaged bearing is subjected to accelerated natural degradation. This test case is used to verify the applicability of the BCI. Results of this experimental study are presented and discussed. Finally, conclusions on the BCI and DRI are drawn.

4.1   AN INDICATOR FOR BEARING CONDITION

The recorded ultrasonic activity of a bearing, typically expressed as the hit-rate (i.e. the amount of acoustic emissions per unit-time), is highly dependent on the operational profile, the geometry of the bearing, and the details of the instrumentation. As such, a parameter must be introduced to normalise these dependencies and obtain a unitary quantity to evaluate the emission-rate due to degradation.

For correct normalisation the inherent repetitivity of the expected sources of AE signals must be considered. Herein defects are split in two groups; (i) material defects, and (ii) lubrication defects. Lubrication defects comprise lubrication contamination and loss of lubrication film. For both of these, the AE activity is expected to be more of a continuous type. Material defects comprise all degradation mechanisms of the rolling elements. For these, early-stage material defects are localised and confined surface or subsurface faults, while late-stage material defects are associated with the presence of (larger) patches of increased surface roughness or spalls. All of these are situated on specific rolling elements, and are expected to be sources of ultrasonic waves. The focus for detection is placed on obtaining the normalisation basis for identification of early-stage material defects, founded on the expectancy that late-stage material defects or lubrication defects will predominantly show up as more significant in this formulation.

Under the assumption that damage-induced signals are emitted when a stress peak passes through the damage zone, the normalisation should be based on the load-cycling of the component that is most likely to develop early-stage material damage. When differentiating between a static and a dynamic raceway, the static raceway experiences the most load cycles for nearly all operational conditions, therefore the formulation should focus on normalisation of the load-cycles on that static raceway. For a particular roller size combined with a continued operational condition involving solely partial rotation, another component than the static raceway may experience the most load cycles.

For a generalised static raceway, an angle of rotation of the dynamic raceway may be defined such that it induces a single load cycle in the static raceway, i.e.

$$\phi_R = \frac{2\left(d_R + d_C\right)}{r_I + r_O}.$$

(4.1)

This definition of the load-pass angle (in radians) is founded in basic trigonometry. The arc length ϕ_R describes the distance the dynamic raceway must travel for a roller to transition one position – in the equation defined by the roller diameter d_R and the clearance distance d_C, the latter of which may be imposed by a cage. The radius is the middle between the inner raceway radius r_I and the outer raceway radius r_O - also referred to as the pitch radius.

Utilising this angle, the link between bearing rotation and load cycles is given by

$$dN = \frac{2\pi dn}{\phi_R},$$ (4.2)

with dN denoting the change in load cycles associated with the change in bearing rotations dn.

In comparison to the earlier introduced component-specific cyclostatonary frequencies, this methodology prescribes a single relation between the expected hit-rate – assuming the hit-rate to be correlated to the load-pass rate – and the rotational speed of the bearing. This reduction in complication is warranted as the proposed load-pass rate is not used as a means of identification, as the return frequencies are in cyclostationary techniques, but is instead used as a normalisation of already identified hits, as a means to judge the severity.

The identification process starts with waveform-similarity-based clustering, as described in Chapter 3 of this work. Through use of those procedures the detected AE signals are grouped in meaningful clusters, which through the load cycle rate may be normalised to an identified hit-rate.

Subsequently, from the normalised identified hit-rate a condition indicator is derived. This bearing condition index is defined as

$$C_B = \frac{1}{1 + \sum\limits_{q=1}^{Q} \sum\limits_{k=1}^{K} \alpha_q \alpha_k \frac{dc_{k,q}}{dN}}.$$ (4.3)

Herein, C_B denotes the bearing condition index, which is determined from the sum of all source-identified AE signals $c_{k,q}$ that are present in dN load cycles. The indices k and q refer to the respective K considered source mechanisms and Q implemented sensor types. Parameters α_q and α_k denote specific scaling functions for the individual sensor types and identified source mechanisms respectively. The resulting value for C_B is contained within the half-open interval $(0, 1]$, where the extreme value $C_B = 1$ represents a pristine bearing, and the limit $C_B \rightarrow 0$ represents a severely worn bearing.

A secondary index is derived to indicate the degradation rate of the bearing. This degradation rate index is defined as

$$D_R = \frac{C_B|_{t-\Delta t}^{t} - C_B|_{t-2\Delta t}^{t-\Delta t}}{C_B|_{t-2\Delta t}^{t-\Delta t}}.$$ (4.4)

Herein, D_R denotes the degradation rate index, which represents the relative change in the bearing condition index (C_B) over the previous to the current time window. Note that through Equation (4.2) $\Delta t \sim dN$.

Tuning of the scaling functions for sensor types and source mechanisms requires a foundation of knowledge based on prior experiments involving various source

mechanisms and requires further investigation than described in this work. To account for the significance of different identified signals, the assumption is made in this chapter that larger cluster are more likely to relate to more significant degradation mechanisms than smaller clusters. Therefore, a shifted form of the generalised logistic function has been implemented to scale for source mechanism [128]:

$$\alpha_{k,GL} = \frac{\alpha_{k,\infty}}{1 + e^{\frac{-c + 0.5 C_{\min}}{0.1 C_{\min}}}}, \tag{4.5}$$

wherein $\alpha_{k,GL}$ represents the scaling factor based on the generalised logistic function, and $\alpha_{k,\infty}$ the target scaling for a fully developed cluster. Furthermore, c represents the number of signals allocated to a particular cluster, and $C_{\min}$ represents the target minimum cluster size. The function is set up so that $\alpha_{k,GL} \approx 0$ at $c = 0$ and $\alpha_{k,GL} \approx \alpha_{k,\infty}$ at $c = C_{\min}$, while attaining point symmetry about $\alpha_{k,GL} = \frac{\alpha_{k,\infty}}{2}$ and $c = \frac{C_{\min}}{2}$. For the pseudo-source mechanism scaling $C_{\min} = 50$ has been used.

Without implementing a-priori knowledge on the eventual size of the cluster, the implemented source mechanism tuning factor increases as the procedure encounters more hits allocated to the respective cluster.

The target scaling for a fully developed cluster ($\alpha_{k,\infty}$) is determined by the desired interpretation of BCI values. Two significant indicator levels have been selected, a first one separating 'no concern' from 'warning' at a BCI of 0.9, and a second one separating 'warning' from 'at-risk' at a BCI of 0.5. Through the selection of $\alpha_{k,\infty}$ these are linked to particular hit-rates. An inverse reduced version of Equation (4) is used to determine $\alpha_{k,\infty}$ for an idealised source mechanism of no particular concern, i.e.

$$\alpha_{k,\infty} = \frac{1 - C_B}{C_B \frac{dc}{dN}}, \tag{4.6}$$

wherein the hit-rate and bearing condition index represent the target couple of matched parameters. Without delving into details of the experimental foundation [129], a hit-rate of 1 hit per load cycle is considered as the border between 'no concern' and 'warning', as it is indicative of the presence of some form of progressive wear in an early stage. For this border, the earlier mentioned first indicator level at a BCI of 0.9 is used. This results in $\alpha_{k,\infty} = 1/9$. Disregarding sensor type scaling and assuming the logistic function is fully developed, this source mechanism scaling places the 'at-risk' limit at ~9 hits per load-cycle.

Regarding tuning the sensor type scaling factors, a layered system is proposed, that is an element-wise product of factors to account for the number of sensors, their relative sensitivities, and the placement of the sensor arrays. The implemented tuning is further discussed in the specification of the sensor system.

4.2   RUN-TO-FAILURE EXPERIMENT ON A BOGIE WHEEL BEARING

A run-to-failure experiment has been conducted to evaluate the proposed BCI and DRI, and to assess the tuning of the α-factors. The bearing used in this experiment originates from the industry, and has seen prior use that theoretically already consumed 40% of the basic rating life [130]. It is fixed in a test rig which pushes

the bearing against a larger rotating wheel using a hydraulic cylinder. A schematic overview of the set-up is shown in Figure 4.1.

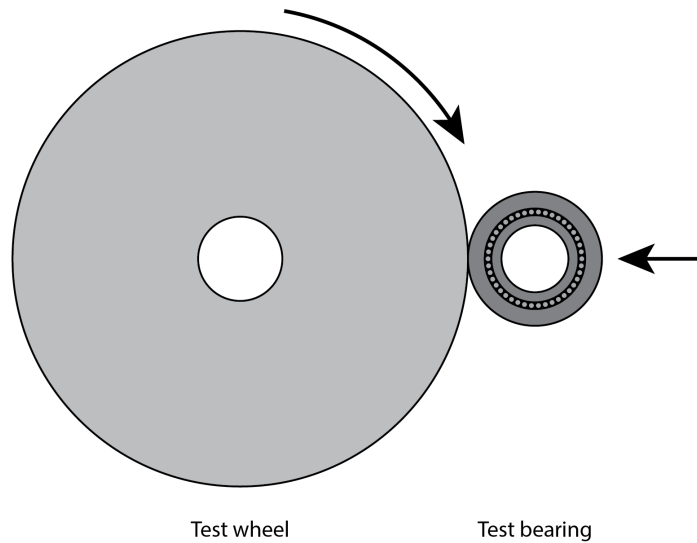Test wheel   Test bearing

Figure 4.1: Illustration of the bogie wheel bearing test set-up.

The test bearing is a bogie wheel that supports in-plane horizontal movement of a lifting beam on an offshore construction vessel. In the installation, two of these types of wheels are present in hydraulically actuated z-support towers. At the bottom of these towers two wheels allow for x-translation of the entire beam-and-support structure, at the top of the towers a single wheel allows for y translation of the beam. Through the hydraulic cylinder in the tower, pre-compression (80% of static capacity) of the entire rolling system is achieved to guarantee proper support of the lifting beam. In the experiment one of the lower wheels is used. As mentioned before, in prior operation on-board, 40% of the theoretical basic rating life had already been consumed. Pictures of a selection of the rolling elements before the start of the test are shown in Figure 4.2.

The wheel is a custom bearing with an outer diameter of 400 mm. It comprises a primary radial bearing split into four raceways, with two secondary axial bearings at the sides. Each of the four raceways of the radial bearing contains 42 rollers with a diameter of 20 mm and a length of 40 mm. The inner raceway itself has a diameter of 248 mm. Each axial bearings contain 58 rollers with a diameter of 12 mm and a length of 11 mm in a cage. All of the rolling surfaces are made out of quenched and tempered 42CrMo4 alloy steel. Both radial and axial rollers are made out of 100Cr6 through-hardened bearing steel, and the cages are made out of CuZn40Pb2 leaded brass.
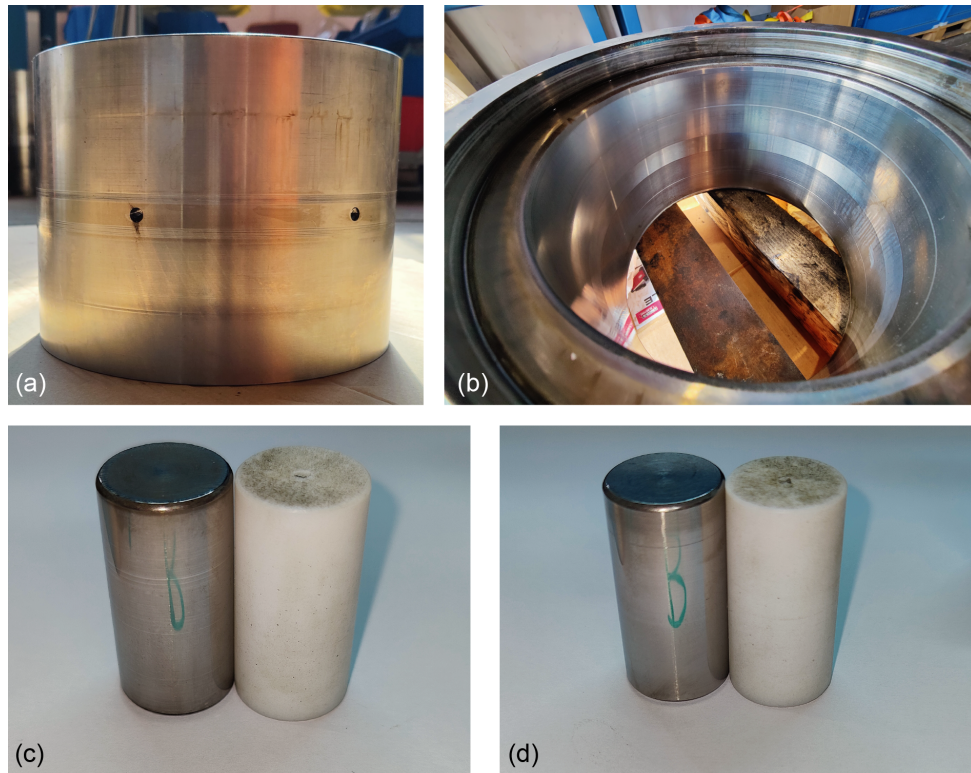
Figure 4.2: Pictures of the pre-test inspection of the bogie wheel bearing, showing: (a) the static inner raceway, (b) the dynamic outer raceway, and (c–d) two steel and PTFE rollers.

4.2.1   *Acoustic Emission Instrumentation*

The bearing is instrumented on the inner ring with four arrays of three sensors. All of the arrays are situated on the static raceway, positioned on either quarter of the circumference away from the contact point on both sides of the wheel. The positions and composition of the arrays are depicted in Figure 4.3. The three sensors in each array are individually sensitive to a particular frequency band. For low frequencies a 60 kHz resonant R6α is used, which is further isolated using a band-pass filter ranging from 40–100 kHz, for mid frequencies a 150 kHz resonant R15α, with a band-pass filter ranging from 95–180 kHz, and for high frequencies a broadband WSα, with a band pass filter ranging from 180–580 kHz, all sourced from Physical Acoustics Corporation. Pre-amplification is handled by external AEP5Hs set to a gain of 40 dB. For data acquisition, a 12 channel AMSY-6 acoustic emission measurement system comprising ASIP 2/A signal processing cards is used. All non-sensor components of the measurement system have been sourced from Vallen Systeme.

In pre-processing of the recorded signals a signal-to-noise ratio (SNR) filter is implemented, imposing a minimum SNR of 10 (20 dB). This filter compares the peak amplitude of the signal to the peak amplitude in a window of 100 μs prior to the initial threshold crossing.
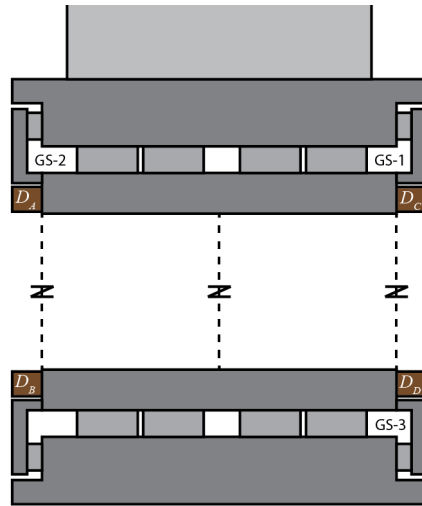
Figure 4.3: Lay-out of bogie wheel bearing instrumentation, with sensor node (D) representing an array of the three types of sensors. Also depicting the locations of grease sampling (GS-1, GS-2, and GS-3). Note that the cover plates have been machined to allow for sensor placement on the inner ring.

The implemented sensor type scaling function α_q is composed solely of a sensor number factor. Considering each array is composed of three sensors, and the BCI calculates a sum of the hit-rates of the different sensors in an array, a proportional scaling of $\alpha_q = [1/3 \ 1/3 \ 1/3]$ is used for the respective low-, mid- and high-frequency sensors. This implementation of an effective average hit-rate over a sensor array is founded on the observation that AE signals generated by significant degradation could be present in all frequency ranges simultaneously, as shown in Chapter 3 and other experiments [129].

4.2.2 *Experimental Procedure*

To impose accelerated natural degradation on the test bearing, it is installed in a roller testing machine. Herein, a hydraulic cylinder pushes the shaft with the test bearing onto a mechanically driven support wheel. The rig is capable of exerting a maximum force of 490 kN onto the shaft, while the support wheel rotates with up to 18 revolutions per minute, which given the size ration between the test bearing and support wheel results in a maximum speed of 61.2 rpm.

Given the load rating of the bearing, the capacity of the cylinder is insufficient to further consume the basic rating lifetime of the bearing in a reasonable timeframe. Therefore the contact stress is artificially increased by substituting part of the original rollers for non-load-bearing polytetrafluoroethylene (PTFE) rollers. The effects of this reduction of load-bearing rollers on both the basic load rating and basic rating lifetime have been studied using both numerical modelling and the standards prescribed by ISO-281 [130], [131]. A reduction to 8 load-bearing roller per raceway, and thus a replacement of 34 rollers for PTFE variants, reduces the basic

dynamic load rating to 504 kN. Alternatively, a reduction to only 6 load-bearing rollers would decrease the basic dynamic load rating to 406 kN.

The 8 roller configuration is selected, and is to be subjected to a load of 343 kN for a peak contact stress of 2800 MPa. These conditions are associated with a basic rating lifetime of 575,000 cycles. Considering the estimated prior lifetime consumption in the field, the remaining lifetime is expected to be approximately 345,000 cycles, which at a testing speed of 60 rpm would imply a total testing duration of 96 hours.

Testing is performed in two modes of operation. The bulk of the lifetime is consumed at a load of 343 kN with a speed of 60 rpm. Subdivided in blocks of 25 minutes, this operational mode consumes 1,500 cycles per block. Alternatively, the bearing is subjected to the same load of 343 kN with a reduced speed of 7.5 rpm – to investigate AE signal generation at low-speed. This mode of operation is used for 12 minute blocks that contain 94 cycles. All blocks are separated by 5 minutes of downtime. A typical testing day comprises 11 high-speed and 2 low-speed blocks in that respective order.

At around every ~60,000 cycles an extensive inspection of the bearing was scheduled. For this inspection, the bearing was disassembled and fully cleaned. Three grease samples were taken from locations indicated in Figure 4.3 and sent for analysis at Shell LubeAnalyst in accordance with industry standards. The rolling elements were visually inspected and pictured for reference. Following on the inspection the bearing was reassembled with clean grease.

4.3   BOGIE WHEEL RUN-TO-FAILURE RESULTS AND DISCUSSION

The present chapter presents and discusses the results of the experiment up to the second inspection. Over the course of approximately 122,000 cycles, the basic rating lifetime consumption has been increased from 40% to 62%. Significant wear has been observed on both raceway in the form of grooving and increased surface roughness. Several pictures of the rolling elements at this stage are shown in Figure 4.4. The dynamic outer raceway displays an evenly distributed wear pattern over the whole circumference, whereas the static inner raceway displays a localised peak in the wear severity at the loading zone that fades out in either direction along the circumference. Among all rolling elements, the wear of highest severity was present on the inner raceway near the loading zone. Prior to the final inspection an intermediate inspections has been performed. The observations will be discussed in parallel to the observed ultrasonic activity over the course of the experiment.

Leading up to the second inspection a total of ~15,900,000 AE signals have been recorded by the twelve measurement channels collectively that surpass initial filtering. The ultrasonic activity, represented as the load-cycle normalised hit-rate, is shown in Figure 4.5, in which each of the four sensor arrays is represented by an individual graph. The vertical dashed line indicates the inspection at ~64,000 cycles. An arbitrary selection of three waveforms from each measurement channel is depicted in Figure 4.6.
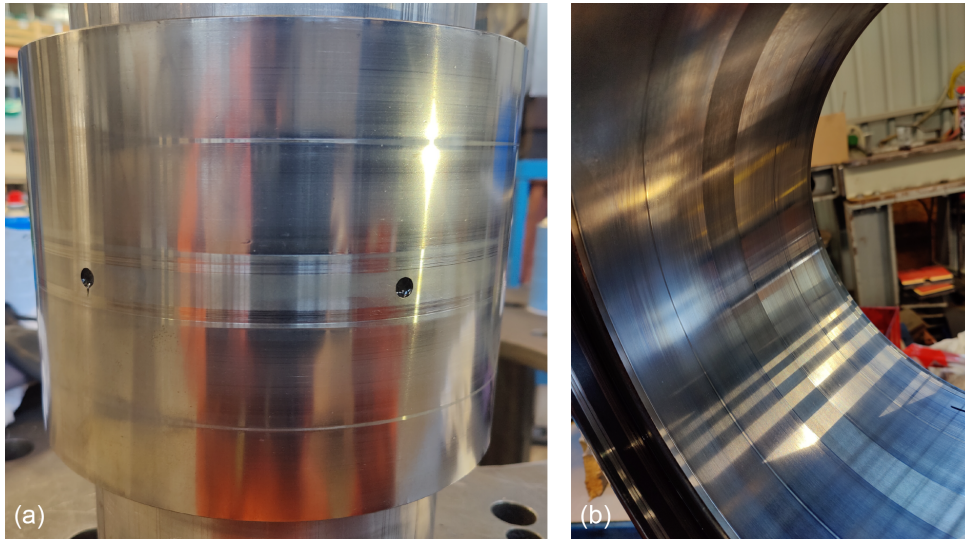
Figure 4.4: Pictures of the second inspection of the bogie wheel bearing, showing the wear pattern on: (a) the inner raceway comprising increased surface roughness (scratching) and major grooving, and (b) the wear patter on the outer raceway comprising increased surface roughness (scratching) and grooving.
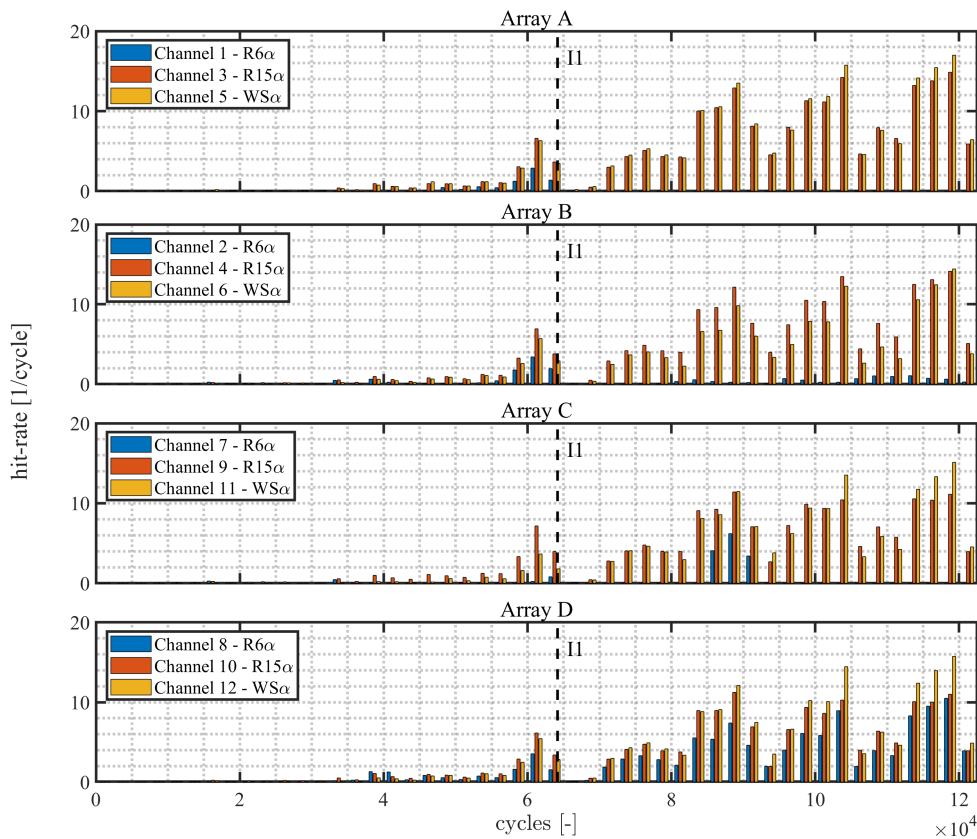

Figure 4.5: Ultrasonic activity represented as load-pass normalised hit-rate, showing separated graphs per sensor array. The dashed vertical line (I1) indicates the performed inspection.
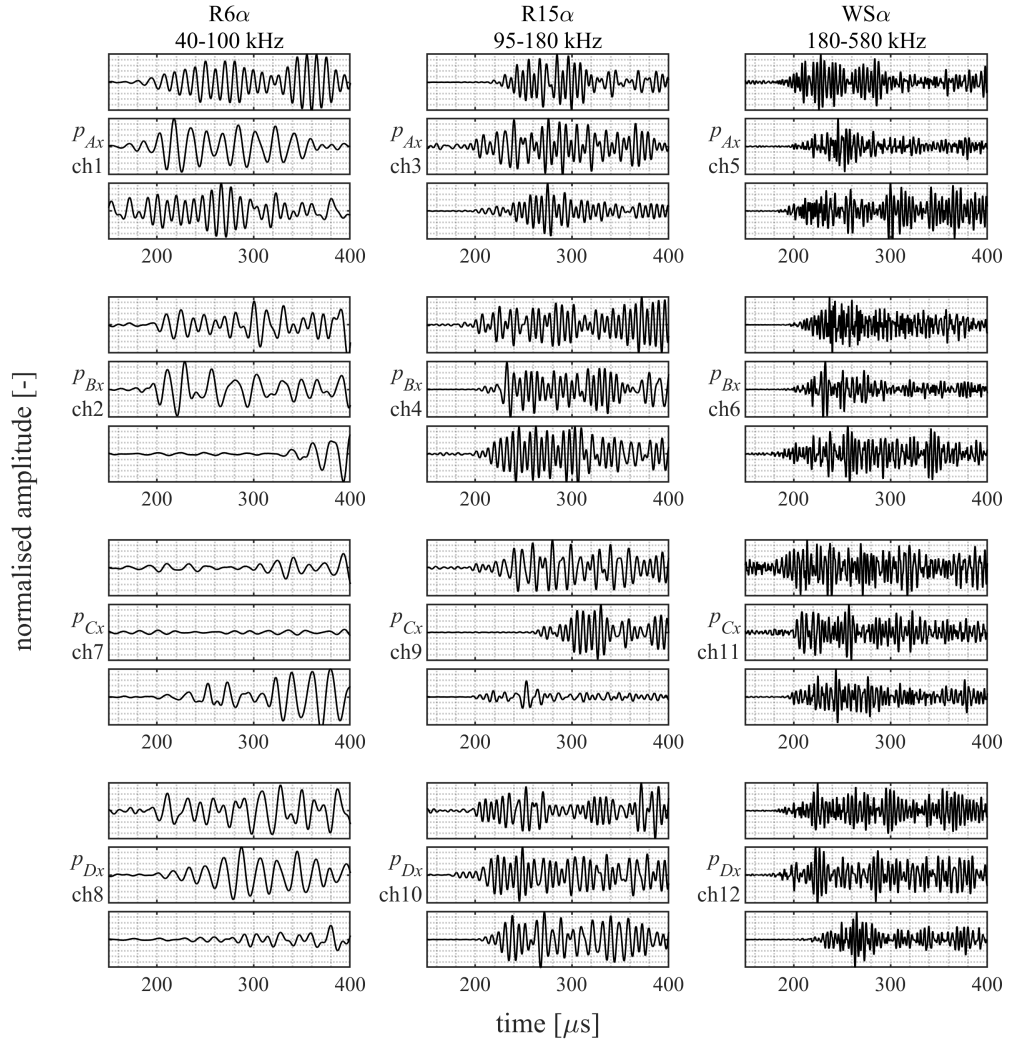
Figure 4.6: Overview of an arbitrary selection of waveforms recorded on the bogie wheel bearing.

Considering Figure 4.5, the block prior to the first inspection at ~64,000 cycles shows a gradually growing increase in hit-rate. This indicates the onset of a degradation mechanism that develops in severity. The peak in activity approaches 7 hits per load cycle, which is probably an indication of contamination particles in the grease. As such, significant wear development is expected. Most of the measurement channels display similar trends, with solely the low-frequency sensor of array C (channel 7) indicating differing sensitivity.

These observations in the hit-rate are supported by the first inspection and grease analysis. The inspection reports wear development in the form of increased surface roughness and minor grooving. Figure 4.7 shows some pictures of the raceway and rollers captured during this inspection. Additionally the lubrication analysis shows a wear particle index (WPI) of 2,036 as the average for the three sampling
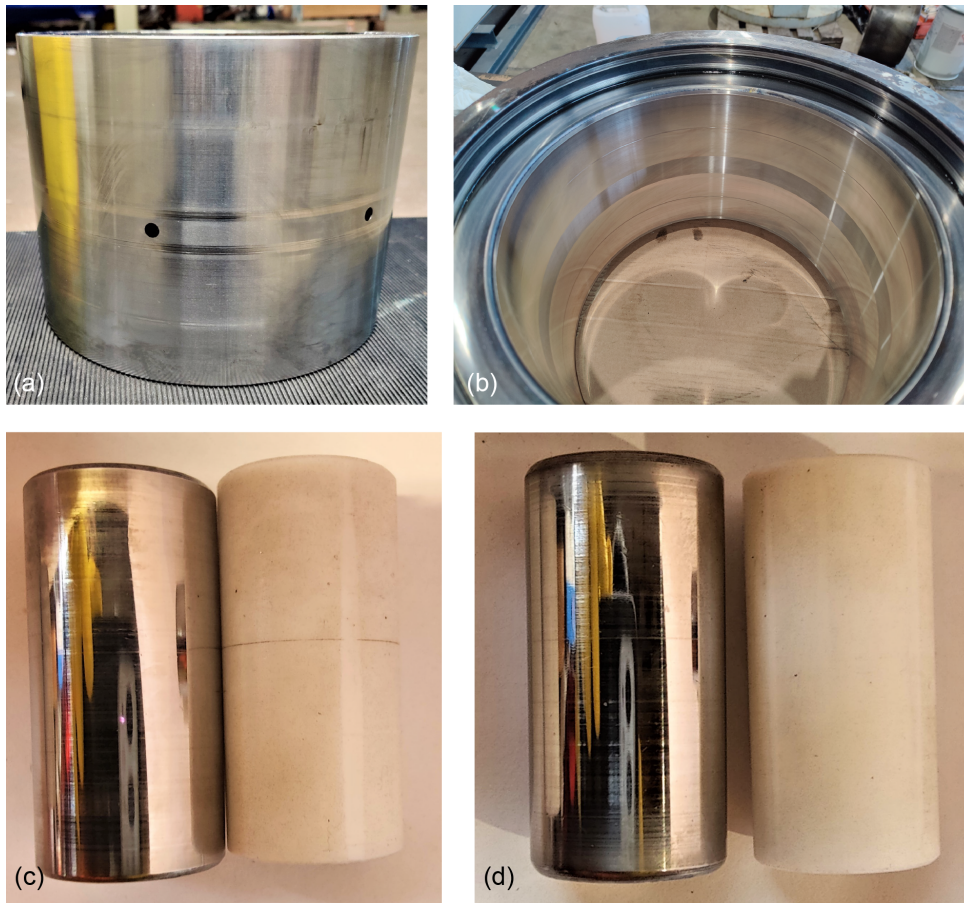
Figure 4.7: Pictures of the first inspection of the bogie wheel bearing, showing the wear pattern on: (a) the inner raceway comprising increased surface roughness (scratching) and minor grooving, (b) the outer raceway comprising increased surface roughness (scratching) and minor grooving, and (c-d) two steel and PTFE rollers comprising minor increased surface roughness (scratching).

locations. Considering a WPI below 500 is safe, and any value above 1500 is putting the bearing at risk[1], the sampled WPI is indicative of heavily contaminated grease.

Directly following on the first inspection, after reassembling the bearing with clean grease, the hit-rates reduce towards zero. This is an indication that the prior activity was primarily due to contamination and associated abrasive surface wear, since any initiating fatigue crack would be expected to develop further and thus emit stress waves.

After continuous cycling under load, the hit-rate rises again, and eventually surpasses the prior levels, peaking at 18 hits per load cycle, which is approximately two-and-a-half times the hit-rate peak prior to the first inspection. A wave-like pattern is visible within the increasing trend, which overlaps with the progression of measurement days. This could partly be related to variation in the viscosity of the grease as the bearing warms up during daily operation. Another notable feature is the omission a matching trend of low-frequency signals for arrays A, B and C

---

1 Personal correspondence, W. Fontenot, SOFEC, 21-06-2021

with reference to array D. This is likely a result of filtering, and an indication that arrays A,B, and C may have detected noisier signals.

The second inspection at ~122,000 cycles reports further wear development (depicted in Figure 4.4). Moreover, the lubrication analysis reports a WPI of 5,362 as the average for the three sampling locations. This is approximately two-and-a-half times the WPI during the first inspection, suggesting a possible direct correlation between WPI and hit-rate.

Following on the initial observations, the data is clustered using the approach described in Chapter 3. Event-building is used to establish connections between clusters. As an example, from a structure of event-built clusters present in all measurement channels three arbitrary waveforms from each measurement channel are depicted in Figure 4.8. The hits identified by the combined event-building and clustering approach are used for the calculation of the BCI and DRI.
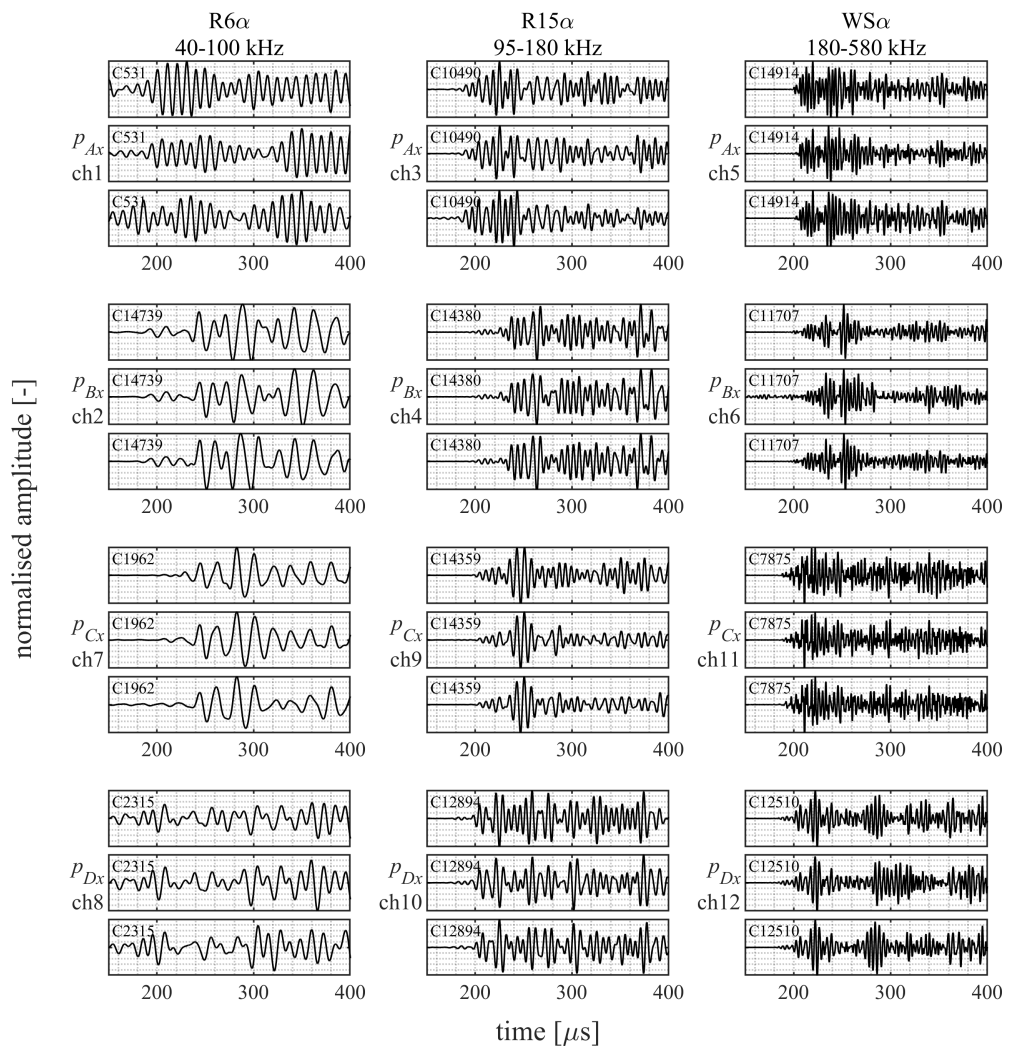
Figure 4.8: Overview of an arbitrary selection of waveforms associated with a structure of clusters identified through event building.
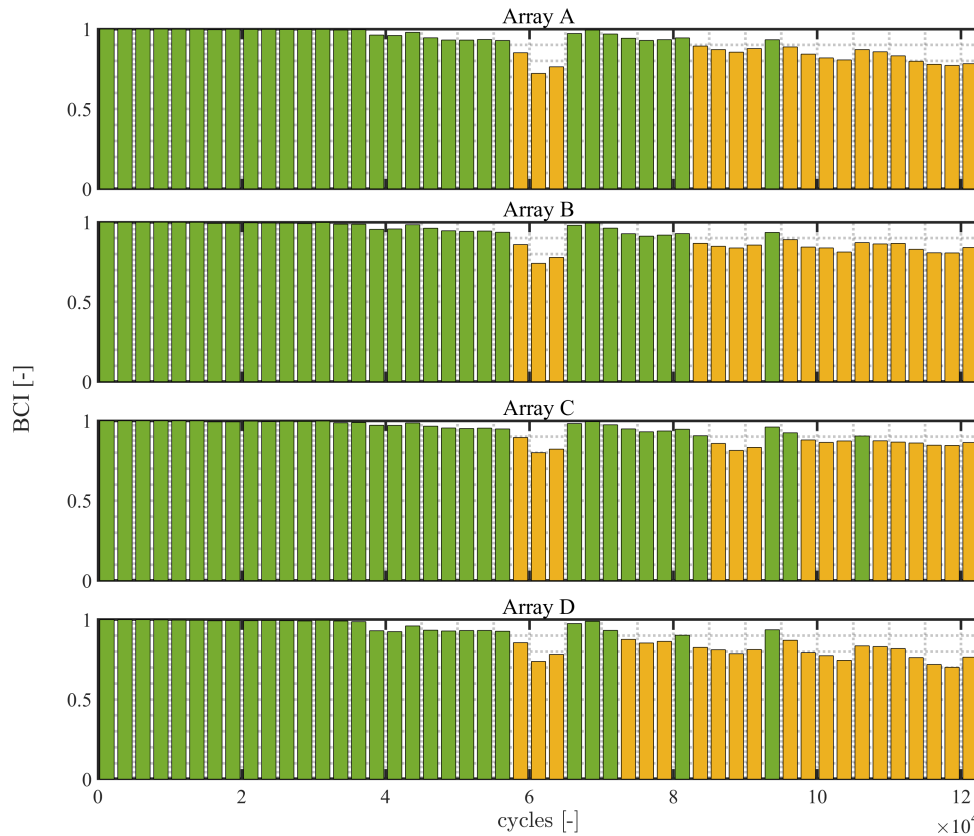
Figure 4.9: Bearing condition index (BCI) for the four sensor arrays, with colours indicating levels for 'no concern' (green), 'warning' (yellow), and 'at risk' (red).

Figure 4.9 shows four BCI graphs representing the four sensor arrays. The colour coding of the bars represents the three indicator levels; no concern (green), warning (yellow), and at risk (red). The subdivision in cycle-bins is equal to Figure 4.5. Initial observation shows small variation between the BCI values calculated for different sensor arrays towards the end of the test. This is mainly attributed to the differences in the detected low-frequency signals, as shown in Figure 4.5. Prior to the first inspection, more similar trends in all frequency-ranges are visible in Figure 4.5, which are also reflected in the similarity of the BCI up to 65,000 cycles. This result suggests sensor sensitivity correction is an important feature of the BCI.

The general trend of the graphs clearly highlights the inspection at ~64,000 cycles, where the BCI indicates a recovery of the condition. This recovery in condition is the direct result of cleaning the bearing and the application of pristine grease. Prior to this inspection the gradually increasing hit-rate triggers a warning at 57,500 cycles, some 7,500 cycles before the lubrication sampling was performed that indicated severe contamination which might put the bearing at risk. As lubrication sampling can only be performed incidentally, the gradual build-up of contamination, and thereby the exact point of exceedance of the warning level, is unknown. In

future work, a run-to-failure experiment may be conducted wherein inspections are triggered solely by the indication of the BCI to verify the warning and at-risk levels.

After the first inspection, the BCI remains at a level of no concern until 87,500 cycles. In contrast to the hit-rates shown in Figure 4.5, the activity some 17,500 cycles prior to this point is not indicated as a warning, even though the overall hit-rate seems comparable to just before to the inspection. This is an indication that the identification approach has not found sufficient similarity to generate larger clusters, and that the subsequent source mechanism scaling – through the implemented logistic function – limits the weight these hits have on influencing the BCI. Later on, sufficient structure in terms of clusters in the AE signals is identified to drop the BCI to the warning level.

Variation in the BCI is highlighted by the DRI, the latter is shown in Figure 4.10. Most notable in this graph is the recovery of the bearing condition after the inspection due to the cleaning of the bearing and the replacement of the contaminated grease for new grease. Indications of decreasing BCI show notable growth around 60,000 just before the first inspection. In contrast, between the first and second inspection, DRI values seem to imply a more gradual degradation stretched over a longer cycle-period. Herein the wavy pattern that has been observed in Figure 4.5 is also visible. Moreover, it seems that in between the instances of BCI recovery (at 80,000, 92,500, and 105,000 cycles) the degradation rate shows a decreasing trend, hinting towards a plateau that increases more gradually. This might be an indication of an operational effect influencing the detectability of a degradation mechanism, which for this case may be the interaction between particle contamination and grease viscosity.
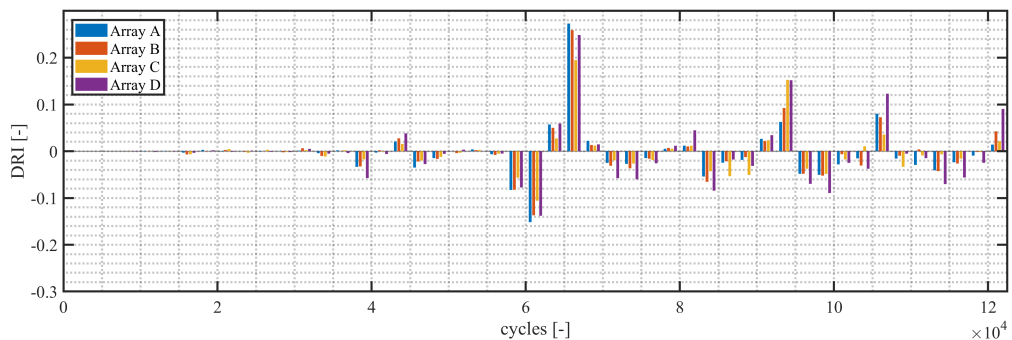

Figure 4.10: Degradation rate index (DRI) for the four sensor arrays.

Returning to the sensitivity of the tuning factors, in response to the reduced detection of low-frequency signals as indicated in Figure 4.5, an alternative sensor type scaling of $\alpha_q = [1/9 \ \ 4/9 \ \ 4/9]$ is proposed. Note that for this scaling the sum of the weighing factors remains one, while the weight of the low-frequency signals is one-fourth in comparison to the mid- and high-frequency signals. The resulting BCI is shown in Figure 4.11.

In comparison to Figure 4.9, this graph for the alternative scaling shows more similar trends for the four sensor arrays. Considering the first half of the experiment, up to the inspection at ~64,000 cycles, differences in the performance of the BCI are minor. In the second half of the experiment, more significant changes in the BCI are

visible. Array B displays an earlier indication of a 'warning' around 75,000 cycles, some 7,500 cycles prior to the originally proposed scaling. Herein, it approaches the warning indication by Array D, which for the alterative scaling is delayed by 2,500 cycles. For Array A and Array C, the alternative scaling increases the general agreement between the BCI with the other arrays, though warning indications remain to appear later.

The alternative scaling seems to improve the performance of the BCI, as similarity between the arrays is expected for a relatively small bearing. However, the reduced early warning indications for array D oppose general adoption. The change in the BCI for array D implies more consistent cluster identification in the low-frequency range in an earlier stage of possible degradation development, which might be overlooked if the influence of the low-frequency range is generally decreased. Though it must be noted that the exact condition of the bearing in between the inspections is unknown, and therefore the 'correctness' of the earlier detection in Figure 4.9 cannot be assessed.

The observed changes in the BCI, and associated indicator, demonstrate the importance of appropriate scaling. In cases where the measurement system may
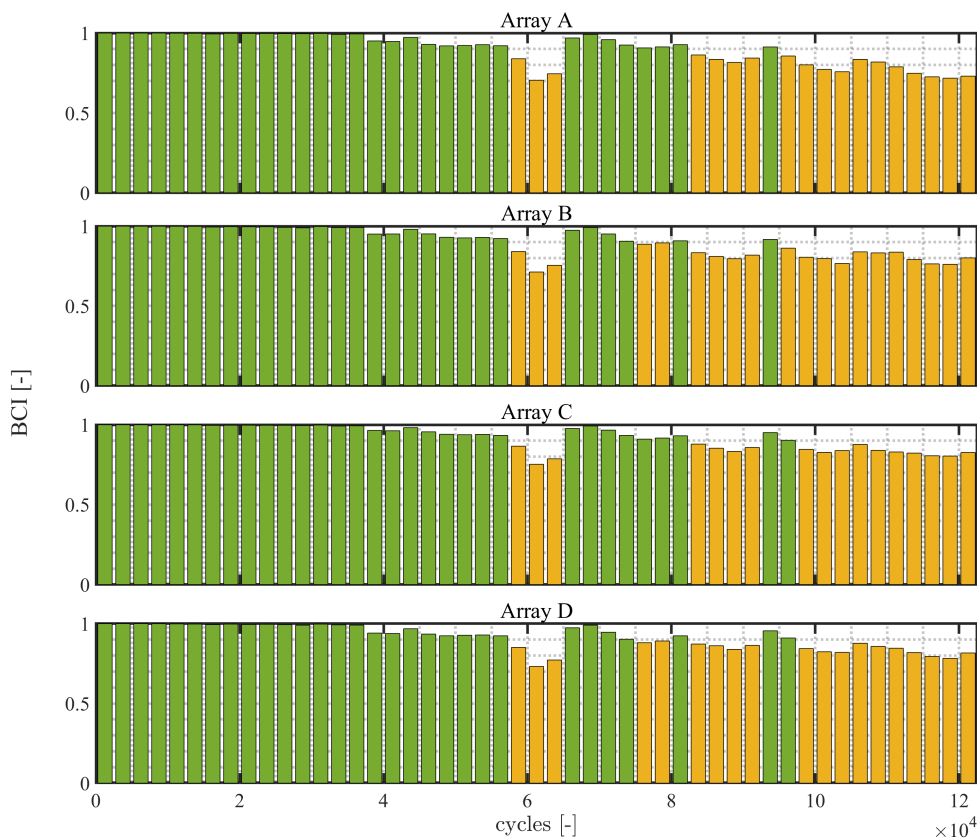

Figure 4.11: Bearing Condition Index (BCI) for alternative sensor type scaling, with colours indicating levels for 'no concern' (green), 'warning' (yellow), and 'at risk' (red).

be compromised and data may be lacking, adoption of appropriate sensor type scaling likely improves the general performance of the BCI. This alternative scaling could also be applied solely to the arrays wherefore irregularities are detected. The exact definition of appropriate scaling, both in design and off-design conditions are subject to further research, as well as what constitutes irregularities in the measurement performance.

4.4   CONCLUSIONS

An indicator for estimating roller bearing condition from AE signals is proposed. The proposed bearing condition index (BCI) consolidates the source mechanism-related hit-rates for a multi-frequency sensor array into a single value. A load-pass normalised BCI is defined which incorporates three indicator levels. The proposed indicator is verified in a run-to-failure experiment involving a bogie wheel bearing recovered from heavy-lifting equipment. Over the course of approximately 122,000 cycles, wear – comprising erosion and surface roughening – has been developed while AE signals have been recorded by four closely-spaced sensor arrays. At two instances a full inspection of the bearing has been performed and lubrication samples have been collected. The observed hit-rates prior to the inspections show a strong correlation to the WPI determined for the lubrication samples, both showing an increase or the second inspection of approximately two-and-a-half times the values for the first inspection. The calculated BCI indicated the first warning some 10,000 cycles before the first inspection. Following on the inspection and reassembly of the bearing with new grease, the BCI temporarily recovers to a level of no concern. For 20,000 cycles this BCI level is maintained, before the warning indication shows again. The results suggest that (i) there is a direct correlation between hit-rate and lubrication analysis WPI, (ii) renewal of the grease slows down the evolution of degradation in the bearing, (iii) the proposed source mechanism scaling reduces the influence of identified minor clusters, and (iv) the BCI provides a promising and intuitive indication of the bearing state. The primary challenge to address in future research is more quantitative assessment of the indicator levels.

5

REVIEW

This dissertation lays-out the foundation a quantitative methodology for condition monitoring of highly-loaded low-speed roller bearings. A review of the prior art has shown that particularly the intersection of slow and non-constant speed is not well understood and the associated uncertainties necessitate such a development in the field of bearing condition monitoring. Acoustic emission has been selected as the technique to be explored in this work for the reason that it allows for the detection of early stage degradation initiation and offers a promising trade-off between coverage and sensitivity.

On these considerations, a methodology for bearing condition monitoring is proposed, that aims at grouping acoustic emission signals to separate indications of probable damage mechanisms from background noise. It further includes an indicator function to differentiate between different levels of source identified hit-rates to issue warnings. The synthesis of this methodology leads to the definition of the bearing condition index (BCI).

Towards the development of proposed methodology, five research objectives had been defined in Chapter 1 which provided structure to the subsequent chapters. These were:

1. Development of a framework to describe and analyse the propagation and transmission of ultrasonic stress waves in bearing geometries.

2. Quantification of inter-component transmission of ultrasonic stress waves in low-speed roller bearings.

3. Development of a framework to identify similarity in acoustic emission source mechanisms.

4. Identification of probable degradation-induced acoustic emission signals in a low-speed run-to-failure experiments at representative scales.

5. Development of a robust condition indicator for low-speed roller bearings.

Chapter 2 addressed the adoption of the framework to describe and analyse the propagation and transmission of AE signals (Objective 1), and demonstrated an application of this framework to an experiment involving simulated AE signals in a representative roller bearing to quantify inter-component transmissibility of AE signals in a static bearing (Objective 2). The results of the experiment highlighted the effectiveness of the framework, and indicated transmission is feasible in quasi-static rolling contacts. The transmissibility seemed frequency dependent, and was most favourable in the mid-frequency range (80–180 kHz) with a reported amplitude drop of 10–13 dB. Lower- and higher-frequency ranges reported slightly higher amplitude drops in the ranges of 12–15 dB and 17–20 dB respectively.

In Chapter 3, the identification approach for AE source mechanisms was defined (Objective 3), and applied to data obtained in a low-speed run to failure experiment conducted with a densely instrumented turret bearing mock-up (Objective 4). In the experiment, wear was developed over the course of approximately 225,000 cycles, and in the recorded AE signals several structures of clusters had been identified. These structures were likely indicative of a consistent AE source mechanism in the nose raceway, which was the same raceway that was also reported as containing the most significant degradation in visual inspection. This insight demonstrated the possibility of identifying AE source components through relative signal amplitudes, and confirmed the applicability of the proposed methodology to identify degradation induced AE signals. Additionally the experiment affirmed inter-component transmissibility of AE signals for low-speed rolling contacts (Objective 2).

Finally, Chapter 4 introduced the definition of the bearing condition index (BCI – Objective 5), and demonstrated the BCI in a test case with data obtained in a run-to-failure experiment conducted with a bogie wheel bearing (Objective 4). In the experiment, over the course of approximately 122,000 cycles wear and significant contamination of the lubrication had been developed. Samples of contaminated lubrication were analysed, which seemed to indicate a direct correlation between wear particle index (WPI) and pre-processed hit-rates of the recorded AE signals. Even though potentially-contamination-induced hit-rates indicated significant AE activity, those did not dominate the behaviour of the BCI. This indicated the identification approach to be promising in separating highly consistent AE source mechanisms (e.g. cracking) from more varying mechanisms (e.g. contamination), which through source-mechanism scaling factors in the BCI prevented obfuscation of the condition indicator. This test case seemed to indicate the effectiveness of the BCI in representing AE data.

5.1   CONCLUSIONS

Distilled from the whole of this dissertation, the following findings are of note:

- Inter-component transmission of ultrasonic stress waves in low-speed rolling contacts is governed by quasi-static conditions, wherein the influence of load is implied to be minor. For two cases of significantly different geometry, speed, and loading, a comparable transmissibility was obtained.

- In a run-to-failure experiment, a combined approach of cross-correlation based clustering and event-building identified several highly-consistent multi-

channel structures of AE signals. For the different sensor arrays, equally good values for the internal similarity of these clusters have been identified, with an average similarity of 93%. This highlights the validity of the assumptions on consistency in AE signal generation and propagation.

- The relative amplitudes between different sensor arrays provides an indication of the component the AE sources are generated in, through the application of the obtained knowledge on AE signal transmission at the internal interfaces.

- A direct correlation between lubrication contamination in terms of a wear particle index (WPI) and pre-processed AE hit-rate prior to lubrication sampling has been observed. This correlation is subject to operational conditions, wherein the correlation seems associated with the underlying trend. The operational dependency shows a ramp-up in hit-rate to the limiting underlying trend, that is likely linked to grease conditions.

- The proposed BCI seems to be a meaningful indicator of bearing condition, as it combines the detailed information of recorded acoustic emissions in different frequency ranges and the subsequent processing of that data into a single parameter. The implemented scaling functions account for the probable significance of groups of AE signals that likely originate from the same source mechanism and may thus represent consistently evolving degradation, while also diminishing the influence of solitary signal that are likely indicative of noise.

5.2   RECOMMENDATIONS

In addressing the research objectives, some topics have not been fully explored, and several new questions have arisen. Of note are the following recommendations for future research:

- Inter-component transmission of ultrasonic stress waves in rolling elements has only been quantified for two sets of geometry, speed, and load. In future work the transmissibility should be quantified over an extended range.

- The identification of highly-similar clusters and multi-channel structures therein is of use for tracking consistent source mechanisms, however, the assumption of gradual change of the transfer path may not always hold, leading to the separation of a single source mechanism into several smaller clusters in extreme cases. In future work this aspect should be further investigated.

- The presented experiments all benefited from complete and extensive data samples covering the degradation process. The availability of only a limited data sample may reduce the reliability of the identification approach and indicator function. In future work the minimum required data sample from which the bearing condition may be reliably obtained should be investigated.

- The BCI seems to perform well in the presented case, however, the warning thresholds need to be assessed more critically in future work.

- The presented experiments have all been conducted in laboratory environments. Though the background noise in most cases was considered to be moderate, higher background noise levels may be present in the field. In future work, the performance of the presented methodology in a representative environment should be investigated.

A

NUMERICAL VALIDATION OF CORRELATION VARIATION

In Chapter 3, assumptions are made on the similarity of the transfer path for small variations in the location of the source mechanism. This appendix discusses a numerical investigation to support these assumptions. First, the spectral element method (SEM) is briefly introduced, followed by a description of the model. Next, the results are presented and shortly discussed. Finally, conclusions are drawn.

A.1 THE SPECTRAL ELEMENT METHOD

The basis for SEM has been outlined independently by Patera [132] and Young [133]. It is a Galerkin-based finite element formulation, while applying Legrange polynomial interpolants on a grid of Gauss-Lobatto-Legendre points as orthogonal higher-order trial functions at the element level. The method has the additional benefit of resulting in a diagonal mass matrix, allowing for a more efficient time integration for wave propagation problems – in this case, through a Newmark-β scheme. For further reading on the implementation of SEM for wave propagation the work of Komatitsch et al. [134]–[136] may be consulted. In the present appendix, the implementation of Pahlavan et al. [112] has been utilized.

A.2 MODEL DESCRIPTION

The defined spectral finite element model is shown in Figure A.1. It represents the geometry of the test set-up as described in Chapter 3. Two materials have been implemented, which are steel for the roller, raceways, and substructure, and bronze for the cage. Properties of the implemented materials are given in Table A.1. The inter-component transmissibility is replicated using a thin interface-layer between the connected components. These interface-layers use the same base properties as the implemented steel, while having their elasticity reduced to impose reflection on the interface. To attain the transmissibility as obtained in Chapter 2, the surface interface between the substructures and the raceways uses a Young's modulus of

20 GPa, and the line interface between the rollers and the raceways uses a Young's modulus of 700 MPa.

The element size and order have been refined in the context of mesh sensitivity analysis to obtain a converged solution. The final mesh uses an element size of 2 mm with a third-order basis function. For explicit time integration, a time-step size of 50 ns is used.

Four output nodes are defined to represent receivers. Their positions are indicated in Figure A.1, and approximate the sensor locations described in Chapter 3. The coordinates (x, y) in millimetres with the accuracy of 0.5 mm are: $(24, 93)$ for the support substructure receiver, $(24, 201)$ for the nose substructure receiver, $(358, 93)$ for the support raceway receiver, and $(358, 201)$ for the nose raceway receiver.

Grids of source nodes are defined for the nose raceway and the roller. For the nose raceway grid the range in x-direction is $296 \leq x \leq 313$ mm with approximately 1 mm spacing, and the range in y-direction is $186 \leq x \leq 200$ mm with the same spacing. For the roller grid the range in the x-direction is $296 \leq x \leq 313$ mm also with the same spacing, and the range in y-direction is $184 \leq x \leq 170$ mm again with the same spacing. The exact location of the source is subject to the node position. For each grid point the source signal is excited at the nearest node.

The sources signals are narrow-band pulses with frequency content representative of the measured AE signals in the experiments of Chapter 3. Figure A.2 shows the imposed source signature.
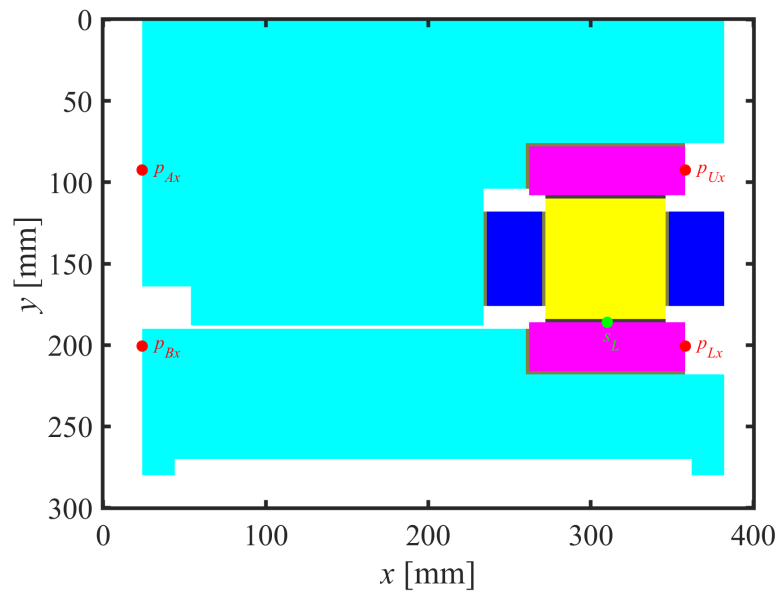
Figure A.1: Geometry of spectral finite element model.

Table A.1: Physical properties of numerically implemented materials.

Property	Steel (all, excl. cage)	Bronze (cage)
Young's modulus	210 GPa	97 GPa
Density	7,800 kg·m^{-3}	8,600 kg·m^{-3}
Poisson's ratio	0.3	0.3
Shear modulus	81 GPa	37 GPa
P-wave speed of sound	6,020 m·s^{-1}	3,897 m·s^{-1}
S-wave speed of sound	3,218 m·s^{-1}	2,083 m·s^{-1}
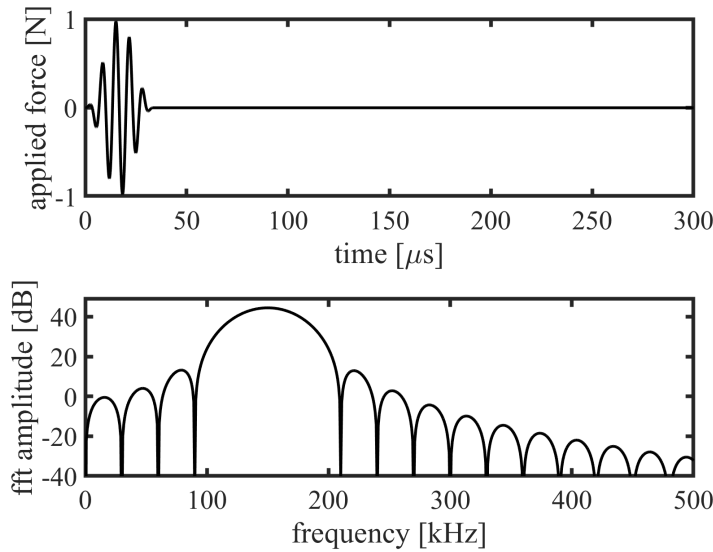
Figure A.2: Implemented source signature, showing a narrow-band five-pulse signal centred around 150 kHz.

A.3 SIMULATION RESULTS AND DISCUSSION

For the grids of source points in the nose raceway and roller, SEM simulations have been performed to extract the propagated waves at the virtual sensor locations. Presented results are based on the out-of-plane displacement. To illustrate the results, an overview of three regularly spaced propagated signals per source grid towards the virtual sensor locations is shown in Figure A.3. The figure displays the normalised waveforms relative to the imposition of the five-pulse source signal with a centre frequency of 150 kHz. Notable is the propagation of the wave front, as it sequentially arrives at the virtual measurement locations on the nose raceway (p_{Lx}), the support raceway (p_{Ux}), the nose substructure (p_{Bx}), and finally the support substructure (p_{Ax}). Between the three source locations for either component, significant changes between the waveforms can be observed, which imply reduced similarity. Considering the source signals in all of the simulated cases are identical, differences in the observed waveform are solely the result of the different transfer paths.

To evaluate how this variation might affect the identification of a consistent source mechanism, two cases are compared. One with a single reference, wherein the cross correlation is determined for each source grid point with a single reference point on the interface. For the raceway source grid this single reference is located at $(310, 186)$, while for the roller source grid it is located at $(310, 184)$. The other case uses a local reference, wherein the cross correlation is determined as the minimum cross correlation for each grid point with its direct rectilinear neighbours.

The calculated similarities of the recorded responses for the whole grid of source points relative to a single and a local reference are presented in Figure A.4 and Figure A.5, respectively for the nose raceway sources, and in Figure A.6 and Figure A.7 for the roller sources.
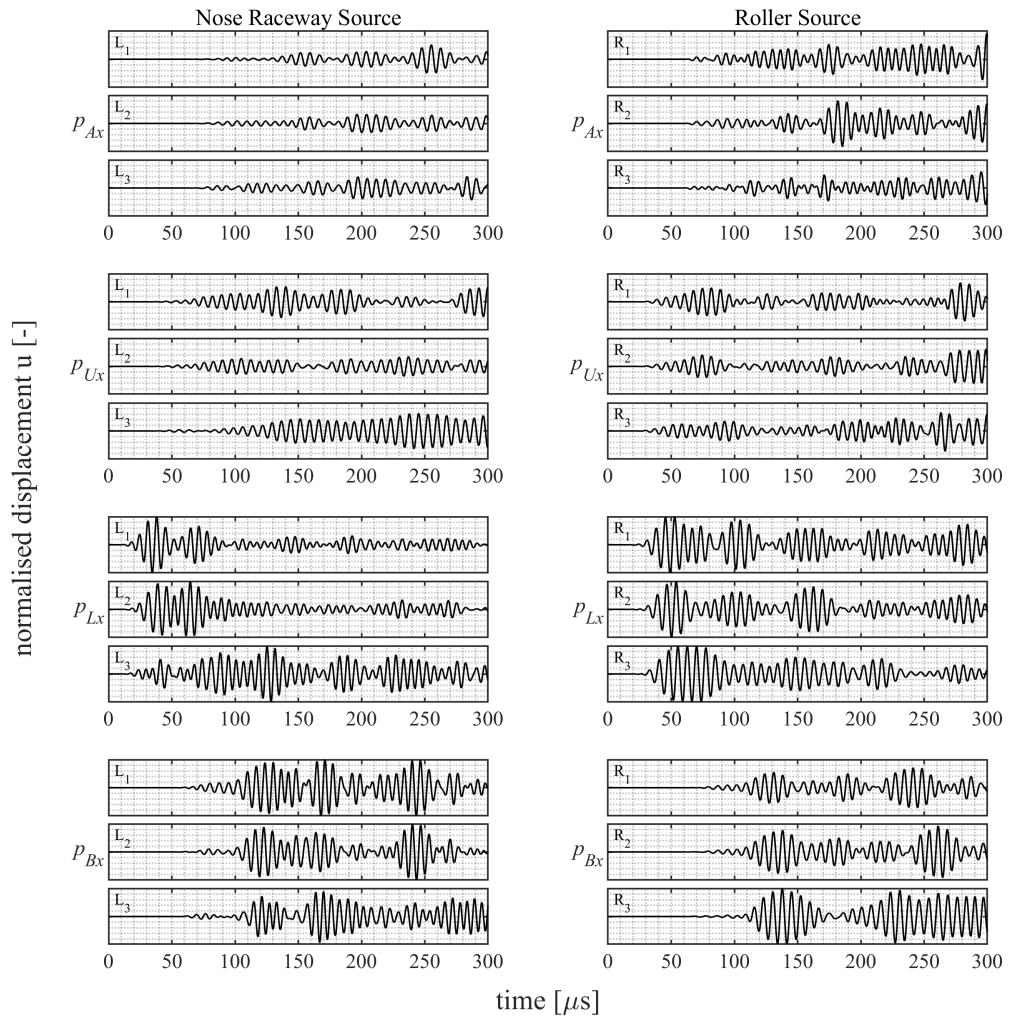
Figure A.3: Overview of three selected simulated waveforms at the virtual sensor locations for source signals in the nose raceway (left) and the roller (right). These source locations are also reflected in Figure A.4, Figure A.5, Figure A.6, and Figure A.7.

For the source grid in the nose raceway, the similarity contours relative to a single reference source at $(310, 186)$ of the propagated signals at the virtual sensor locations are shown in Figure A.4. In the graphs a bold isoline represents the similarity value of 0.7, that is used in the clustering approach as the border between similar and dissimilar signals. Smaller sensitivity to the source location in the vertical direction can be observed, which may partly relate to the thickness of the component directly subjected to the source signal being in the same size order as the dominant wavelength. Another observation is the presence of multiple pockets of higher similarity – though not yet identical signals – likely implying some repeated interaction with reflected waves. The smallest distance the source may displace to reach the (dis)similarity threshold is in the order of 3 mm. Overall, it can be concluded that there is significant variation the transfer path imposes on the source signal, reinforcing the notion that a recorded waveform at a certain location is uniquely defined by the combination of source signal, transfer path, and sensor transfer function.
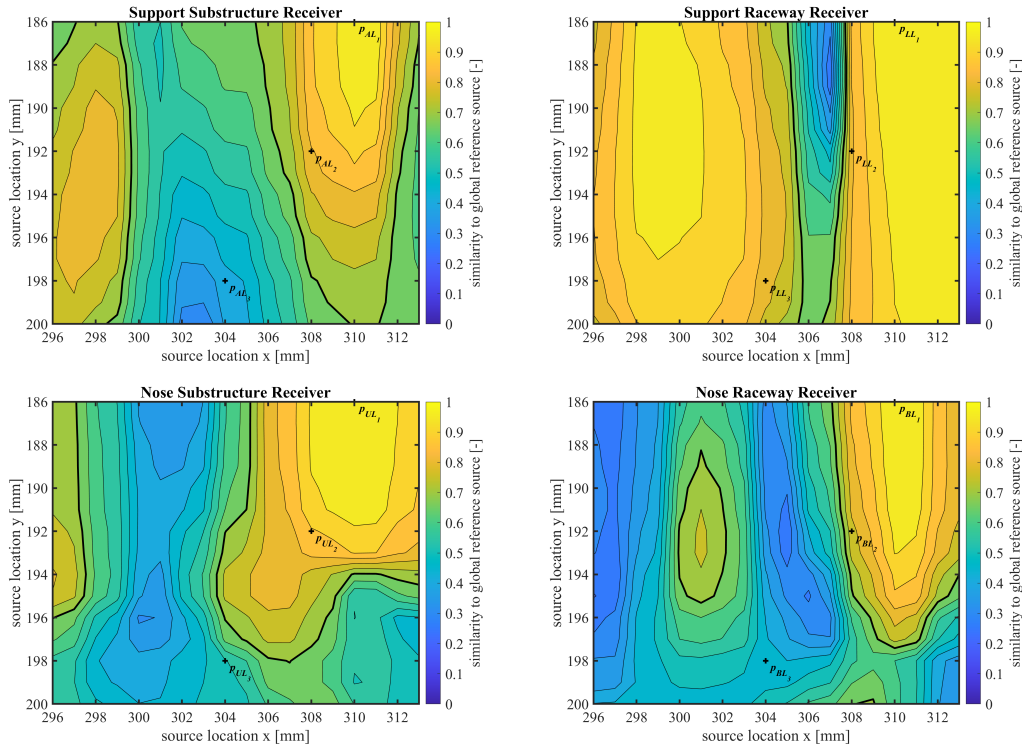
Figure A.4: Single reference similarity contour for the nose raceway source grid, with the reference source at $(310, 186)$. The four graphs display the similarities of the u-displacement signal as observed at the virtual sensor locations.

In contrast to the large variation observed in the similarity relative to a single reference, the similarity to a local reference as depicted in Figure A.5 is much more consistent. For nearly all of the virtual sensor locations the local similarity within the entire source grid is higher than the threshold of 0.7. Only for the path towards the virtual sensor on the support raceway there is a small zone of reduced similarity within the investigated grid, which, considering the steep descent in the single reference similarity observed for the same sensor location in Figure A.4, was

expected. Moreover, using this analysis, this local dissimilarity of the transfer path giving rise to separation of the evolving source mechanism in several clusters may be countered in sensor layout design.
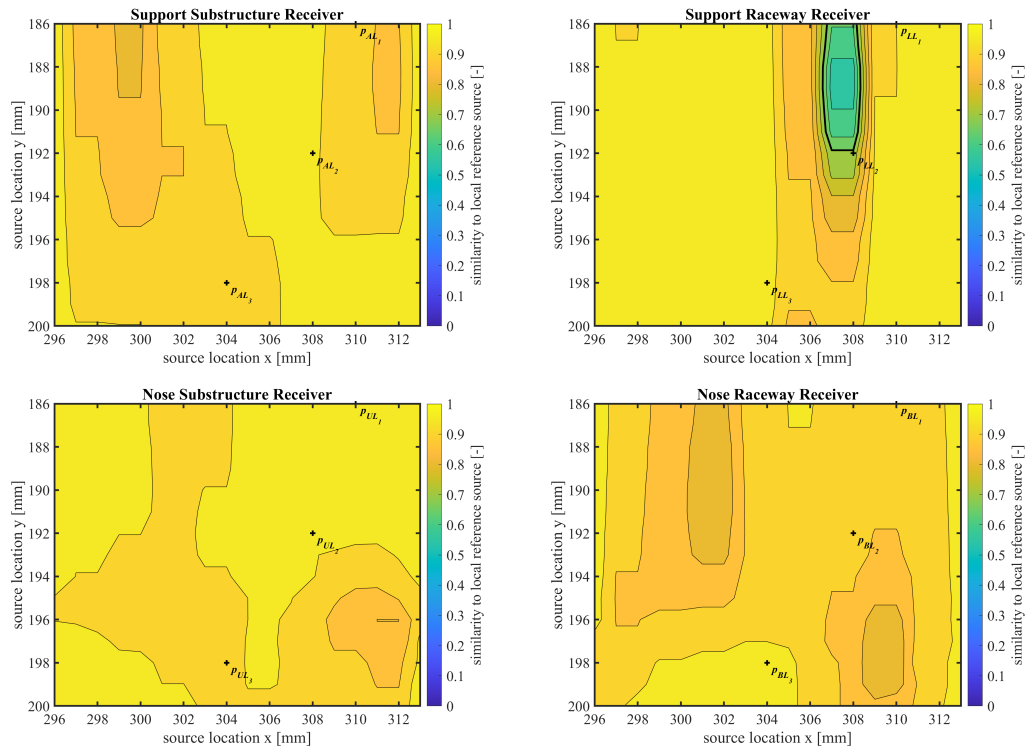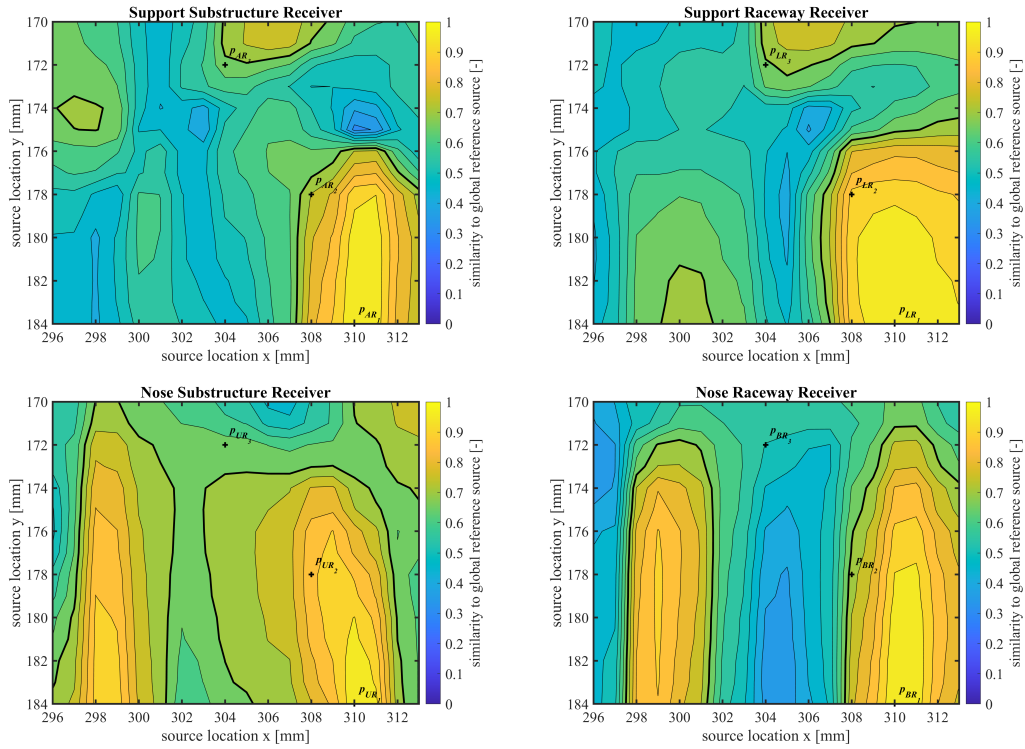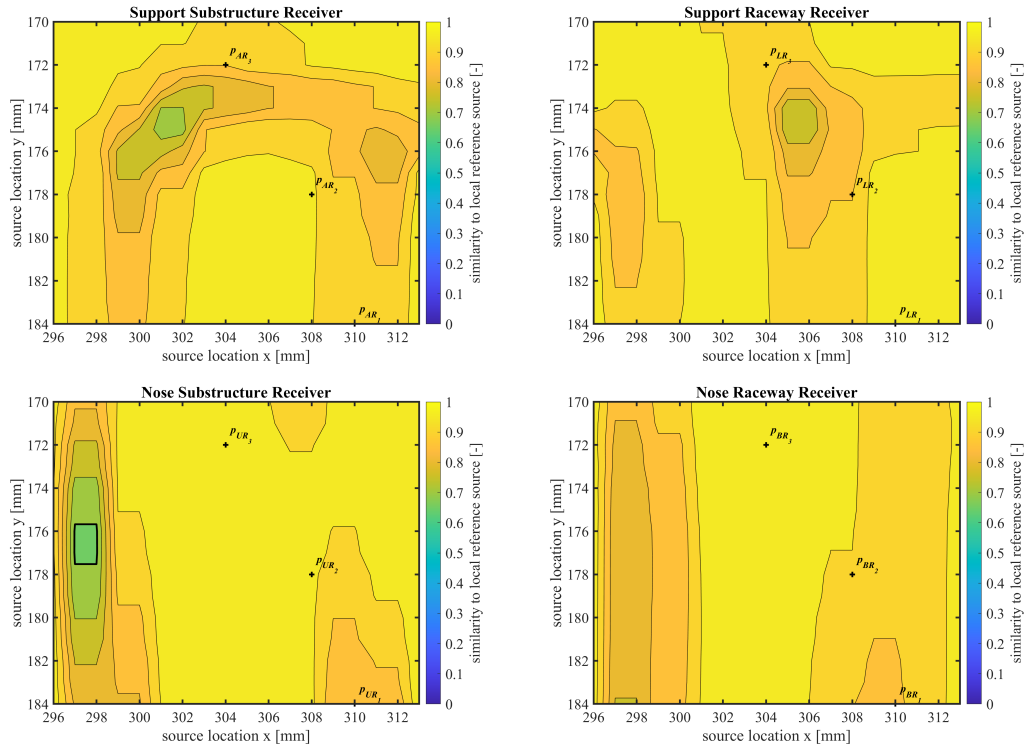

Figure A.5: Local reference similarity contour for the nose raceway source grid, presenting the lowest similarity relative to reference sources in a local rectilinear cross. The four graphs display the similarities of the u-displacement signal as observed at the virtual sensor locations.

The results for the source grid in the roller, as presented in Figure A.6, show comparable trends to the source grid in the nose raceway. Note that for this source grid, the reference source is located at $(310, 184)$, at the bottom of the graphs. Again a source displacement of 3 mm is observed as the minimal sufficient distance to pass the (dis)similarity threshold. Also visible are the more vertical pattern in the similarity, as well as the presence of several pockets of high similarity separated by regions of dissimilarity. The pattern can perhaps not be merely attributed to the ratio between wavelength and domain dimension. Other dependencies are to be explored in further research.

Figure A.6: Single reference similarity contour for the roller source grid, with the reference source at $(310, 184)$. The four graphs display the similarities of the u-displacement signal as observed at the virtual sensor locations.

In contrast again the local reference as shown in Figure A.7 shows consistently high similarity for nearly the entire source grid on the roller. Similarly to the raceway source grid, a small pocket of decreased similarity is observed for the paths towards a single sensor.

Figure A.7: Local reference similarity contour for the roller source grid, presenting the lowest similarity relative to reference sources in a local rectilinear cross. The four graphs display the similarities of the u-displacement signal as observed at the virtual sensor locations.

A.4   CONCLUSIONS

The similarity of the transfer path for small variations in the source location has been numerically studied using a higher-order finite element analysis, i.e. SEM. The geometric model represents a linear turret bearing mock-up. Results of global analysis show that variation of about 5 mm in the source location may already lead to a reduced similarity that surpasses the (dis)similarity threshold. The observed variation of the similarity with the displaced source signal reinforces the notion that a recorded waveform at a certain location is uniquely defined by the combination of source signal, transfer path, and sensor transfer function. Local analysis shows high similarity may be retained for nearly the entire investigated grid if the source displacement is small – investigated in the order of 1 mm. This may be achieved to a large extent if a moving time window is used for assessment of the AE signals from consistent damage mechanisms. The presented results support the assumptions used in Chapter 3.

B

ADDITIONAL TEST CASES UTILISING THE TURRET BEARING MOCK-UP

In addition to the run-to-failure test described in Chapter 3, several tests have been executed using the linear bearing mock-up. For the sake of brevity these tests had been omitted from that chapter. In this appendix, a summary of these test cases and highlights of the main findings are presented. The assessment concerns baseline, lubrication starvation, lubrication contamination, artificial damage, and corrosion test cases. In principle all tests cases follow the same methodology as the baseline cases, with the exemption of the particular conditions that relate to the investigated damage case.

The base set-up and instrumentation is the same as described in Chapter 3. For the modular components the situation differs. Raceways are composed of Hardox 600, with the exception of the Hardox 550 raceways used in the corrosion case. All tests use a configuration of three rollers with a diameter and with of 75 mm. The rollers are made of 100Cr6 through hardened bearing steel. A complementary cage is made of CuSn12C tin bronze.

B.1 METHODOLOGY & BASELINE

Baseline tests have been executed to form a foundation by which the detectability of other test cases may be assessed. Four different vertical loads and three horizontal speeds are applied to excite a spectrum of operational conditions, in order to assess their influence on the ultrasonic activity. The highest speed level matches the speed used in Chapter 3. At the highest load a significantly reduced contact pressure in comparison to Chapter 3 is obtained, due to the usage of more and larger rollers.

Data is collected over the course of approximately 340 cycles. Results are pre-processed as described in Chapter 3, and evaluated by clustering and hit-rate over different frequency bands.

During the baseline test low AE activity was measured. The channels on opposing sides of the rollers show the same behaviour. For all frequencies, on all locations, some activity was generally present, though remained below an average of 0.3 hits

per cycle for the whole case. As expected, clusters within this low level activity do not provide further insights.

B.2   LUBRICATION STARVATION

Tests with reduced lubrication have been executed to investigate ultrasonic signatures associated with a bearing operating in lubrication starved conditions. The starved condition was simulated by applying only a minimal layer of grease during installation.

For the lubrication starved condition, increased activity was detected, with low-frequency channels on both raceways and the support substructure detecting up to 2 hits per cycle. This increase has not been detected on the nose substructure, and seems less pronounced on the nose raceway. These observations suggest the starvation is more severe towards the support raceway, i.e. the top of the chamber. This may be related to the gravitational effect. Considering the final inspection, also depicted in Figure B.1, a broken film has been observed for the contact between the roller and the support raceway. Clustering analysis (not shown) indicated correlated AE signal recorded by the low-frequency sensors. These clusters correlated with the change in load level, however, no distinguishable correlation with the speed variation was observed.
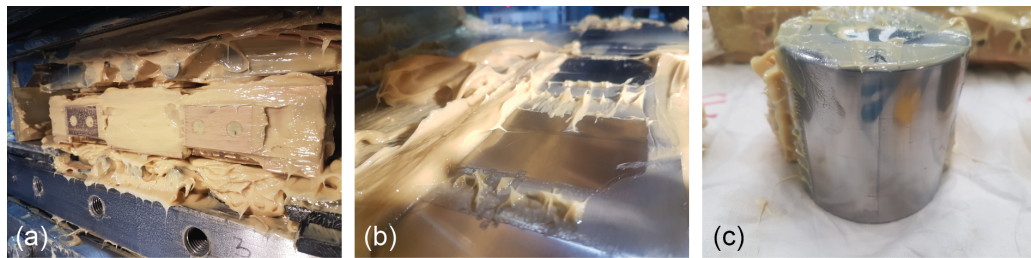
Figure B.1: Inspection of lubrication on rolling elements after the starvation test, showing; (a) Lubrication in the upper chamber directly after removing the cover plate, (b) the broken lubrication film around a roller on the upper nose raceway, and (c) the broken lubrication film on the upward facing segment of the centre roller in the upper chamber.

B.3   LUBRICATION CONTAMINATION

Tests with particle contaminated lubrication have been executed to investigate ultrasonic signatures associated with a bearing operating in contaminated conditions. Particle contamination by volume ratios (iron to grease) of; (i) 1:125000 (~16 mg Fe per kg of lubrication); (ii) 1:2500 (~800 mg Fe per kg of lubrication); and (iii) 1:50 (~40,000 mg Fe per kg of lubrication) were evaluated. These samples were introduced in the pockets between roller, cage and raceway at the bottom of the chamber, in order of increasing contamination. The set-up was not cleaned in-between different contamination levels. The used contamination particles have been collected from
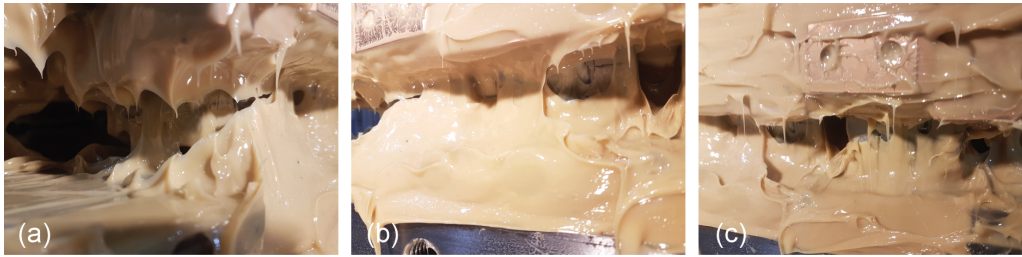
Figure B.2: Inspection of contaminated lubrication after the sample (i) test, showing; (a–c) The slight contamination of the lubrication between and around the rollers and the underside of the cage in the upper chamber.

abrasive work of primarily steel. As such the contamination is a mixture of steel and silicon-carbide particles, with sizes up to 500 μm.

For the first sample, increased hit-rate ranging between 1–2 hits per cycle was observed for low-frequency range on the raceways and support substructure. On the nose raceway, this increased activity was also observed for the mid-frequency range. In the clusters, no structure seemed to be present. Figure B.2 shows the grease condition at the end of the test case with the first sample, steel particles are visible – though barely noticeable.

For the second sample, a significant increase in AE activity was observed. In the low-frequency range, high hit-rates ranging 5–10 hits per cycle were detected on both raceways and the nose substructure, with amplitudes consistently reaching about 80 dB. A comparable level of activity was also observed in the mid-frequency range. Only on the nose raceway, the high-frequency range seemed to show slightly increased activity, up to 2 hits per cycle, with amplitudes mostly limited to about 60 dB.

For the third sample, again a significant increase in activity was detected. On the raceways, for all frequency ranges, extremely-high hit-rates in the order of 100 hits per cycle ware observed, with amplitudes reaching towards 100 dB. On the substructures, reduced amplitudes and hit-rates were observed, with another notable reduction for the support substructure compared to the nose substructure.

After the test with the third sample, metal particles were distributed throughout the lubricant, as clearly shown in Figure B.3. Furthermore, a layer of grey lubricant was notable at the base of the chamber. This could be due to the effect of gravity, and it may be the main reason for the significant higher ultrasonic activity observed on the nose-side of the set-up.

The reported sediments are likely the main cause of the generation of damage on both the rollers and the raceways. As shown in Figure B.4 and Figure B.5, pitting signatures were detected during the final inspection of the components of the chamber. Furthermore, comparing the damage on roller 2B to the other rollers, i.e. roller 1B and roller 3B, it was evident that the second roller is affected by more severe degradation. The same consideration can be made looking at the inspection results of the upper nose raceway, shown in Figure B.5.

Figure B.3: Inspection of contaminated lubrication after the sample (iii) test, showing; (a–b) The noticeable contamination in the lubrication around the rollers, and (c) around (primarily the bottom of) the cage.
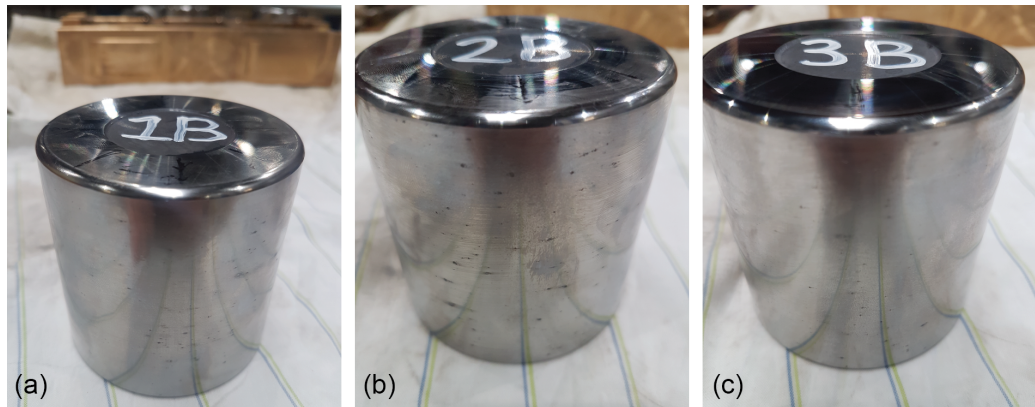

Figure B.4: Inspection of the upper chamber rollers after the sample (iii) test, showing; (a) The damage on roller 1B, (b) the damage on roller 2B, and (c) the damage on roller 3B.
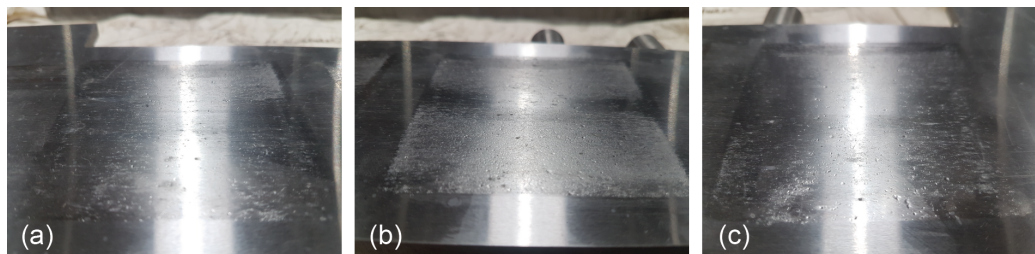

Figure B.5: Inspection of the upper nose raceway after the sample (iii) test, showing; (a) The damage on the contact area with roller 1B, (b) the damage on the contact area with roller 2B, and (c) the damage on the contact area with roller 3B.

B.4   ARTIFICIAL DAMAGE

Tests with artificially damaged rollers have been executed to investigate ultrasonic signatures associated with these. Four kinds of damages were introduced; (i) a point damage; (ii) a radial line damage; (iii) a transverse line damage; and (iii) a patch damage. Pictures of the four damages are shown in Figure B.6. All damage types were made using an angle grinder. In all tests, the damaged roller was situated
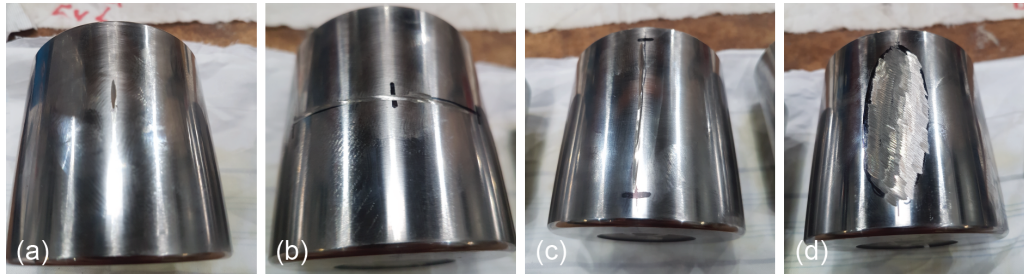
Figure B.6: Artificially damaged rollers; (a) Point damage, (b) Radial line damage, (c) Transverse line damage, (d) Patch damage.

in the centre position, with the damage pointing upwards towards the support raceway.

For the point damage, low levels of activity were detected for all frequency ranges. Hit-rates did not seem significantly higher than the baseline, though higher amplitude signals were present. For the radial line damage, indications were comparable. Levels of activity and amplitudes similar to the baseline were detected. For the transverse line damage and the patch damage, in all frequency ranges, levels of activity were also comparable to the baseline, while amplitudes seemed slightly increased.

In summary, the investigated artificial roller damage types seemed to be best characterised by a communal lack of distinctive features. No significant direct activity from the contact between the damaged roller and the raceway were detected. The artificially damaged cases show some difference to the baseline test case, though not in a sufficiently pronounced manner to warrant a basis for decision making.

B.5 CORROSION

Tests with a pre-corroded raceway have been executed to investigate ultrasonic signatures associated with a bearing operating with corrosion present. Figure B.7 shows the corrosion process applied on the sample raceway. To obtain a satisfactory level of corrosion the support raceway was naturally corroded over 14 days in a wet outside environment covered by pre-corroded metal particles. The resulting

Figure B.7: Several stages of the corrosion test raceway, showing; (a) Initiation of the corrosion process, (b) the corrosion coverage prior to testing, and (c) the resulting abrasion of corrosion in the contact area after the test.

damaged raceway is shown in Figure B.7b. During the final inspection of the setup, corrosion deposits removals were noted in correspondence of the rollers position, as shown in Figure B.7c.

For the corroded raceway, an increase in low-frequency low-amplitude signals on the raceways was detected, which was more prominent towards the beginning of the test. Clusters indicated correlation between these hits, though no particular consistency in repetitivity or amplitude was observed.

b.6   conclusions

In addition to the conclusions drawn in Chapter 3, test with the linear bearing mock-up have shown that lubrication-related problems, such as contamination and starvation, are relatively straight-forward to detect and identify, while artificial defects and corrosion are barely distinguishable from the baseline.

C

FIELD TEST CASES

To assess the feasibility of applying the knowledge developed in this dissertation in the offshore industry, two field tests have been performed. With reference to Chapter 2, the goal of the first study was to validate the detectability of the transmitted signals over the offshore ultrasonic background. With reference to Chapter 3, the goal of the second study was to investigate the possibility of inferring the bearing condition index (BCI) from a short term measurement. It is outside the scope of this dissertation to present details on the instrumentation and results, since this dissertation concerns the methodology rather than its practical application. Therefore, this appendix only briefly describes two field studies and gives the main conclusions drawn based on these studies.

c.1 "aegir" – investigation of background noise in offshore conditions

Measurements are performed on a sheave block in the 4,000 mT offshore mast crane of Heerema's "Aegir". The instrumented sheave block was the portside upper package of the boom hoist. This package consists of seven sheaves on a single shaft, split in three groups that are separated by the two supporting bulkheads. On either shaft-end and the surrounding structure, eight locations were selected for instrumentation with VS150-WIC-V01 type acoustic emission transducers.

Instrumentation were performed in December 2018 (Figure C.1b), and measurements were executed during two lifting operations in January 2019 (Figure C.1a). Both operations were executed in port at quayside – Vlissingen, The Netherlands. As such the results are not true offshore conditions, however, for the sake of assessing the conditions of representative lifting operations the results are valid. Analysis of the collected data indicated that; (i) the continuous ultrasonic background in a representative offshore environment is reasonably low, i.e. in the rage of 20–25 dB, (ii) during operations an increase in the range of 10 dB should be expected, and (iii) implementation of an AE condition monitoring system is feasible.

Figure C.1: Pictures of "Aegir" measurement, showing; (a) second lifting operation, and (b) sensor installed on shaft.

C.2   "PIONEERING SPIRIT" – INVESTIGATION OF VIABILITY OF INTERMITTENT SHORT-TERM MONITORING

To investigate the possibility of inferring the BCI from a short-term measurement in a representative condition, field tests have been executed on the outboard support of the topside lift system of Allseas' "Pioneering Spirit". The topside lift system comprises a series of movable beams, that can grab and lift an entire topside of an offshore platform. Each beam is vertically supported by two sets of wheels that allow it to move in the horizontal plane. Two beams were selected for evaluation, thereof for both x- and y-translation four wheels per beam were instrumented. Instrumentation and processing followed the principles described in Chapter 3 and Chapter 4.

Measurements were performed on two days in September 2022 (Figure C.2), while the vessel was anchored at Maasvlakte 2, The Netherlands. The conditions were representative for scheduled maintenance or inspection. A total of 16 conditions were assessed; slow and fast movement in x- and y-direction for a longer (A) and a shorter (B) lifting beam. The results of this field investigation indicated that; (i) the BCI can be determined in a representative field environment, and (ii) a short-term measurement may be sufficient to infer condition on specific degradation types.
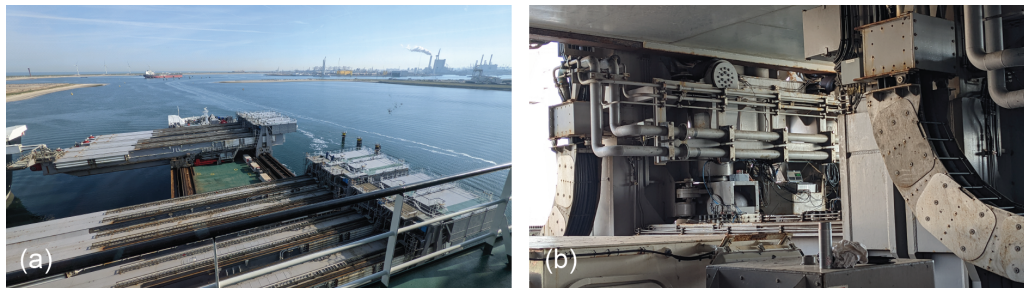
Figure C.2: Pictures of "Pioneering Spirit" measurement, showing; (a) an overview of several starboard beams of the topside lift system, and (b) instrumentation of the outboard support.

D

BEARING CONDITION INDEX FOR TURRET BEARING MOCK-UP

In an extension to the analysis of the experimental data discussed in Chapter 3, this appendix applies the bearing condition index (BCI) as defined in Chapter 4 to the data obtained from the turret bearing mock-up. For the normalisation of the hit-rate, the in the chapter defined cycle that comprises both extension and retraction of the horizontal cylinder is considered to be equivalent to two load cycles. The same scaling functions for sensor types and source mechanisms are used as in Chapter 4, i.e. defined by the parameters $\alpha_{k,\infty} = 1/9$, $C_{\min} = 50$, and $\alpha_q = [1/3 \; 1/3 \; 1/3]$.

The resulting BCI is presented in Figure D.1. This graph shows that the BCI indicates a state of "no concern" for most of the duration of the experiment. In three notable instances the BCI reduces to a "warning" level, these are around 70,000
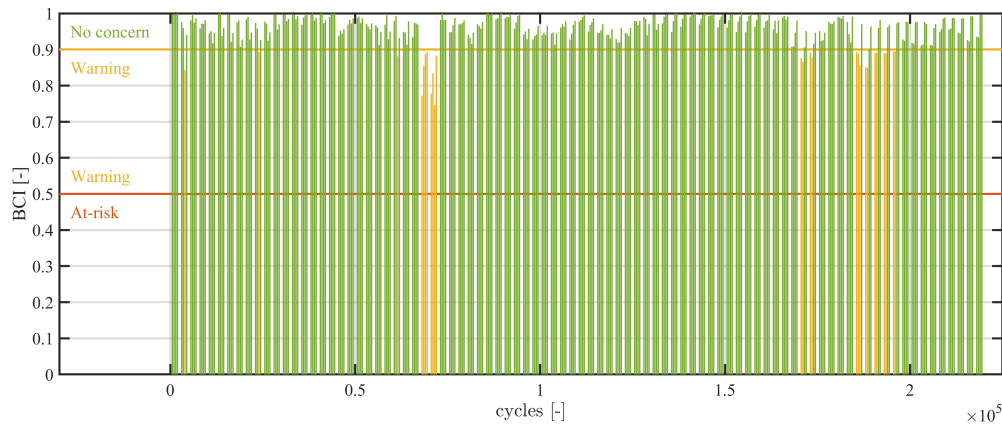
Figure D.1: Bearing condition index (BCI) for the top chamber of the turret bearing mock-up, with colours indicating levels for 'no concern' (green), 'warning' (yellow), and 'at risk' (red). The four bars in each group represent the sensor arrays on the support substructure, support raceway, nose raceway, and nose substructure respectively from left to right.

cycles, 170,000 cycles and 190,000 cycles. These match with the identified structures of clusters and the initial observation of increasing activity and expectancy of indication of degradation.

In short, the BCI calculated from the AE data recorded during the run-to-failure experiment with the linear bearing mock-up highlights periods of interest that are likely indicative of excessive wear or evolving localised damage. These indications have been verified through independent intrusive inspection, which has reported the most significant wear development around those highlighted periods as well.

BIBLIOGRAPHY

[1] ThyssenKrupp Rothe Erde, *Slewing bearings - installation, lubrication, maintenance, and bearing inspection*, 2021.

[2] SKF, *Slewing bearings*, 2019.

[3] I. El-Thalji and E. Jantunen, 'A descriptive model of wear evolution in rolling bearings', *Engineering Failure Analysis*, vol. 45, pp. 204–224, 2014. DOI: `10.1016/J.ENGFAILANAL.2014.06.004`.

[4] H. K. D. H. Bhadeshia, 'Steels for bearings', *Progress in Materials Science*, vol. 57, pp. 268–435, 2012. DOI: `10.1016/J.PMATSCI.2011.06.002`.

[5] B. Lu, Y. Li, X. Wu and Z. Yang, 'A review of recent advances in wind turbine condition monitoring and fault diagnosis', *2009 IEEE Power Electronics and Machines in Wind Applications, PEMWA 2009*, 2009. DOI: `10.1109/PEMWA.2009.5208325`.

[6] I. El-Thalji and E. Jantunen, 'A summary of fault modelling and predictive health monitoring of rolling element bearings', *Mechanical Systems and Signal Processing*, vol. 60, pp. 252–272, 2015. DOI: `10.1016/j.ymssp.2015.02.008`.

[7] H. D. M. de Azevedo, A. M. Araújo and N. Bouchonneau, 'A review of wind turbine bearing condition monitoring: State of the art and challenges', *Renewable and Sustainable Energy Reviews*, vol. 56, pp. 368–379, 2016. DOI: `10.1016/j.rser.2015.11.032`.

[8] A. Rai and S. H. Upadhyay, 'A review on signal processing techniques utilized in the fault diagnosis of rolling element bearings', *Tribology International*, vol. 96, pp. 289–306, 2016. DOI: `10.1016/j.triboint.2015.12.037`.

[9] W. Moustafa, O. Cousinard, F. Bolaers, K. Sghir and J. P. Dron, 'Low speed bearings fault detection and size estimation using instantaneous angular speed', *Journal of Vibration and Control*, vol. 22, pp. 3413–3425, 2016. DOI: `10.1177/1077546314560600`.

[10] J. D. Smith, 'Vibration monitoring of bearings at low speeds', *Tribology International*, vol. 15, pp. 139–144, 1982. DOI: `10.1016/0301-679X(82)90130-X`.

[11] C. K. Mechefske and J. Mathew, 'Fault detection and diagnosis in low speed rolling element bearings part i: The use of parametric spectra', *Mechanical Systems and Signal Processing*, vol. 6, pp. 297–307, 1992. DOI: `10.1016/0888-3270(92)90032-E`.

[12]   J. Antoni, 'Cyclostationarity by examples', *Mechanical Systems and Signal Processing*, vol. 23, pp. 987–1036, 2009. DOI: `10.1016/j.ymssp.2008.10.010`.

[13]   J. Antoni, 'Cyclic spectral analysis of rolling-element bearing signals: Facts and fictions', *Journal of Sound and Vibration*, vol. 304, pp. 497–529, 2007. DOI: `10.1016/j.jsv.2007.02.029`.

[14]   J. Antoni, 'Fast computation of the kurtogram for the detection of transient faults', *Mechanical Systems and Signal Processing*, vol. 21, pp. 108–124, 2007. DOI: `10.1016/j.ymssp.2005.12.002`.

[15]   J. Zhu, J. M. Yoon, D. He and E. Bechhoefer, 'Online particle-contaminated lubrication oil condition monitoring and remaining useful life prediction for wind turbines', *Wind Energy*, vol. 18, pp. 1131–1149, 2015. DOI: `10.1002/we.1746`.

[16]   R. Dupuis, 'Application of oil debris monitoring for wind turbine gearbox prognostics and health management', *Annual Conference of the PHM Society*, vol. 2, 2010. DOI: `10.36001/PHMCONF.2010.V2I1.1867`.

[17]   E. Bechhoefer, R. Schlanbusch and T. I. Waag, 'Techniques for large, slow bearing fault detection', *International Journal of Prognostics and Health Management*, vol. 7, 2016. DOI: `10.36001/ijphm.2016.v7i1.2358`.

[18]   X. Q. Bai, H. L. Xiao and L. Zhang, 'The condition monitoring of large slewing bearing based on oil analysis method', *Key Engineering Materials*, vol. 474-476, pp. 716–719, 2011. DOI: `10.4028/www.scientific.net/KEM.474-476.716`.

[19]   J. Sun, R. J. K. Wood, L. Wang, I. Care and H. E. G. Powrie, 'Wear monitoring of bearing steel using electrostatic and acoustic emission techniques', *Wear*, vol. 259, pp. 1482–1489, 2005. DOI: `10.1016/J.WEAR.2005.02.021`.

[20]   M. Craig, T. J. Harvey, R. J. K. Wood, K. Masuda, M. Kawabata and H. E. G. Powrie, 'Advanced condition monitoring of tapered roller bearings, part 1', *Tribology International*, vol. 42, pp. 1846–1856, 2009. DOI: `10.1016/j.triboint.2009.04.033`.

[21]   T. J. Harvey, R. J. K. Wood and H. E. G. Powrie, 'Electrostatic wear monitoring of rolling element bearings', *Wear*, vol. 263, pp. 1492–1501, 2007. DOI: `10.1016/J.WEAR.2006.12.073`.

[22]   S. Morris, R. J. K. Wood, T. J. Harvey and H. E. G. Powrie, 'Electrostatic charge monitoring of unlubricated sliding wear of a bearing steel', *Wear*, vol. 255, pp. 430–443, 2003. DOI: `10.1016/S0043-1648(03)00089-9`.

[23]   W. Yang, R. Court and J. Jiang, 'Wind turbine condition monitoring by the approach of scada data analysis', *Renewable Energy*, vol. 53, pp. 365–376, 2013. DOI: `10.1016/J.RENENE.2012.11.030`.

[24]   O. Janssens, R. Schulz, V. Slavkovikj, K. Stockman, M. Loccufier, R. V. D. Walle and S. V. Hoecke, 'Thermal image based fault diagnosis for rotating machinery', *Infrared Physics & Technology*, vol. 73, pp. 78–87, 2015. DOI: `10.1016/J.INFRARED.2015.09.004`.

[25]   A. Nair and C. S. Cai, 'Acoustic emission monitoring of bridges: Review and case studies', *Engineering Structures*, vol. 32, pp. 1704–1714, 2010. DOI: `10.1016/j.engstruct.2010.02.020`.

[26] J. Yu, P. Ziehl, B. Zrate and J. Caicedo, 'Prediction of fatigue crack growth in steel bridge components using acoustic emission', *Journal of Constructional Steel Research*, vol. 67, pp. 1254–1260, 2011. DOI: 10.1016/j.jcsr.2011.03.005.

[27] K. M. Holford, A. W. Davies, R. Pullin and D. C. Carter, 'Damage location in steel bridges by acoustic emission', *Journal of Intelligent Material Systems and Structures*, vol. 12, pp. 567–576, 2001. DOI: 10.1106/KDNY-AJ0U-KP2B-P52R.

[28] K. Ohno and M. Ohtsu, 'Crack classification in concrete based on acoustic emission', *Construction and Building Materials*, vol. 24, pp. 2339–2346, 2010. DOI: 10.1016/j.conbuildmat.2010.05.004.

[29] C. V. Steen, L. Pahlavan, M. Wevers and E. Verstrynge, 'Localisation and characterisation of corrosion damage in reinforced concrete by means of acoustic emission and x-ray computed tomography', *Construction and Building Materials*, vol. 197, pp. 21–29, 2019. DOI: 10.1016/J.CONBUILDMAT.2018.11.159.

[30] F. Zhang, L. Pahlavan and Y. Yang, 'Evaluation of acoustic emission source localization accuracy in concrete structures', *Structural Health Monitoring*, vol. 19, pp. 2063–2074, 2020. DOI: 10.1177/1475921720915625.

[31] D. G. Aggelis, 'Classification of cracking mode in concrete by acoustic emission parameters', *Mechanics Research Communications*, vol. 38, pp. 153–157, 2011. DOI: 10.1016/j.mechrescom.2011.03.007.

[32] V. Giurgiutiu, A. Zagrai and J. Bao, 'Damage identification in aging aircraft structures with piezoelectric wafer active sensors', *Journal of Intelligent Material Systems and Structures*, vol. 15, pp. 673–687, 2004. DOI: 10.1177/1045389X04038051.

[33] T. Loutas, N. Eleftheroglou and D. Zarouchas, 'A data-driven probabilistic framework towards the in-situ prognostics of fatigue life of composites based on acoustic emission data', *Composite Structures*, vol. 161, pp. 522–529, 2017. DOI: 10.1016/j.compstruct.2016.10.109.

[34] A. Huijer, C. Kassapoglou and L. Pahlavan, 'Acoustic emission monitoring of carbon fibre reinforced composites with embedded sensors for in-situ damage identification', *Sensors*, vol. 21, 2021. DOI: 10.3390/s21206926.

[35] J. Z. Sikorska and D. Mba, 'Challenges and obstacles in the application of acoustic emission to process machinery', *Proceedings of the Institution of Mechanical Engineers, Part E: Journal of Process Mechanical Engineering*, vol. 222, pp. 1–19, 2008. DOI: 10.1243/09544089JPME111.

[36] H. L. Balderston, 'The detection of incipient failure in bearings', *Materials Evaluation*, vol. 27, pp. 121–128, 1969.

[37] L. M. Rogers, 'The application of vibration signature analysis and acoustic emission source location to on-line condition monitoring of anti-friction bearings', *Tribology International*, vol. 12, pp. 51–58, 1979. DOI: 10.1016/0301-679X(79)90001-X.

[38]   D. Mba, R. H. Bannister and G. E. Findlay, 'Condition monitoring of low-speed rotating machinery using stress waves part 2', *Proceedings of the Institution of Mechanical Engineers, Part E: Journal of Process Mechanical Engineering*, vol. 213, pp. 171–185, 1999. DOI: 10.1243/0954408991529915.

[39]   J. Miettinen and P. Pataniitty, 'Acoustic emission in monitoring extremely slowly rotating rolling bearing', Coxmoore Publishing Company, 1999, pp. 289–297.

[40]   T. Sako and O. Yoshie, 'Diagnostic method of low speed rolling element bearing using ae envelope waveform', *IEEE Region 10 Annual International Conference, Proceedings/TENCON*, pp. 724–729, 2010. DOI: 10.1109/TENCON.2010.5686610.

[41]   Z. Liu, X. Wang and L. Zhang, 'Fault diagnosis of industrial wind turbine blade bearing using acoustic emission analysis', *IEEE Transactions on Instrumentation and Measurement*, vol. 69, pp. 6630–6639, 2020. DOI: 10.1109/TIM.2020.2969062.

[42]   W. Caesarendra, B. Kosasih, A. K. Tieu, H. Zhu, C. A. S. Moodie and Q. Zhu, 'Acoustic emission-based condition monitoring methods: Review and application for low speed slew bearing', *Mechanical Systems and Signal Processing*, vol. 72-73, pp. 134–159, 2016. DOI: 10.1016/j.ymssp.2015.10.020.

[43]   M. Li, J. H. Yang and J. W. Xu, 'Trend analysis of the slow-speed and heavy-load equipment with acoustic emission', *Advanced Materials Research*, vol. 201-203, pp. 2578–2582, 2011. DOI: 10.4028/WWW.SCIENTIFIC.NET/AMR.201-203.2578.

[44]   M. Elforjani and D. Mba, 'Observations and location of acoustic emissions for a naturally degrading rolling element thrust bearing', *Journal of Failure Analysis and Prevention*, vol. 8, pp. 370–385, 2008. DOI: 10.1007/s11668-008-9141-x.

[45]   M. Elforjani and D. Mba, 'Monitoring the onset and propagation of natural degradation process in a slow speed rolling element bearing with acoustic emission', *Journal of Vibration and Acoustics, Transactions of the ASME*, vol. 130, pp. 1–14, 2008. DOI: 10.1115/1.2948413.

[46]   M. Elforjani and D. Mba, 'Detecting the onset, propagation and location of non-artificial defects in a slow rotating thrust bearing with acoustic emission', *Insight: Non-Destructive Testing and Condition Monitoring*, vol. 50, pp. 264–268, 2008. DOI: 10.1784/insi.2008.50.5.264.

[47]   M. Elforjani and D. Mba, 'Natural mechanical degradation measurements in slow speed bearings', *Engineering Failure Analysis*, vol. 16, pp. 521–532, 2009. DOI: 10.1016/J.ENGFAILANAL.2008.06.005.

[48]   M. Elforjani and D. Mba, 'Assessment of natural crack initiation and its propagation in slow speed bearings', *Nondestructive Testing and Evaluation*, vol. 24, pp. 261–275, 2009. DOI: 10.1080/10589750802339687.

[49]   M. Elforjani and D. Mba, 'Condition monitoring of slow-speed shafts and bearings with acoustic emission', *Strain*, vol. 47, pp. 350–363, 2011. DOI: 10.1111/j.1475-1305.2010.00776.x.

[50] M. Elforjani and D. Mba, 'Accelerated natural fault diagnosis in slow speed bearings with acoustic emission', *Engineering Fracture Mechanics*, vol. 77, pp. 112–127, 2010. DOI: `10.1016/j.engfracmech.2009.09.016`.

[51] M. Elforjani, 'Diagnosis and prognosis of slow speed bearing behavior under grease starvation condition', *Structural Health Monitoring*, vol. 17, pp. 532–548, 2018. DOI: `10.1177/1475921717704620`.

[52] T. Yoshioka and T. Fujiwara, 'A new acoustic emission source locating system for the study of rolling contact fatigue', *Wear*, vol. 81, pp. 183–186, 1982. DOI: `10.1016/0043-1648(82)90314-3`.

[53] T. Yoshioka, A. Korenaga, H. Mano and T. Yamamoto, 'Diagnosis of rolling bearing by measuring time interval of ae generation', *Journal of Tribology*, vol. 121, pp. 468–472, 1999. DOI: `10.1115/1.2834091`.

[54] T. Williams, X. Ribadeneira, S. Billington and T. Kurfess, 'Rolling element bearing diagnostics in run-to-failure lifetime testing', *Mechanical Systems and Signal Processing*, vol. 15, pp. 979–993, 2001. DOI: `10.1006/mssp.2001.1418`.

[55] B. Eftekharnejad, M. R. Carrasco, B. Charnley and D. Mba, 'The application of spectral kurtosis on acoustic emission and vibrations from a defective bearing', *Mechanical Systems and Signal Processing*, vol. 25, pp. 266–284, 2011. DOI: `10.1016/j.ymssp.2010.06.010`.

[56] T. R. Lin, E. Kim and A. C. C. Tan, 'A practical signal processing approach for condition monitoring of low speed machinery using peak-hold-down-sample algorithm', *Mechanical Systems and Signal Processing*, vol. 36, pp. 256–270, 2013. DOI: `10.1016/J.YMSSP.2012.11.003`.

[57] A. Cockerill, A. Clarke, R. Pullin, T. Bradshaw, P. Cole and K. M. Holford, 'Determination of rolling element bearing condition via acoustic emission', *Proceedings of the Institution of Mechanical Engineers, Part J: Journal of Engineering Tribology*, vol. 230, pp. 1377–1388, 2016. DOI: `10.1177/1350650116638612`.

[58] D. Hou, H. Qi, D. Li, C. Wang, D. Han, H. Luo and C. Peng, 'High-speed train wheel set bearing fault diagnosis and prognostics: Research on acoustic emission detection mechanism', *Mechanical Systems and Signal Processing*, vol. 179, 2022. DOI: `10.1016/J.YMSSP.2022.109325`.

[59] E. L. Hidle, R. H. Hestmo, O. S. Adsen, H. Lange and A. Vinogradov, 'Early detection of subsurface fatigue cracks in rolling element bearings by the knowledge-based analysis of acoustic emission', *Sensors*, vol. 22, 2022. DOI: `10.3390/S22145187`.

[60] D. Cornel, F. G. Guzmán, G. Jacobs and S. Neumann, 'Condition monitoring of roller bearings using acoustic emission', *Wind Energy Science*, vol. 6, pp. 367–376, 2021. DOI: `10.5194/WES-6-367-2021`.

[61] J. Antoni, 'The spectral kurtosis: A useful tool for characterising non-stationary signals', *Mechanical Systems and Signal Processing*, vol. 20, pp. 282–307, 2006. DOI: `10.1016/j.ymssp.2004.09.001`.

[62]   T. Yoshioka and S. Shimizu, 'Monitoring of ball bearing operation under grease lubrication using a new compound diagnostic system detecting vibration and acoustic emission', *Tribology Transactions*, vol. 52, pp. 725–730, 2009. DOI: 10.1080/10402000902913345.

[63]   B. L. Feirer, P. Ziehl, R. N. Anay, M. Bayat, B. Zhang and E. M. Golda, 'Acoustic emission damage evaluation of rolling element bearings for shipboard machinery', vol. 11380, SPIE, 2020, pp. 249–259. DOI: 10.1117/12.2563819.

[64]   J. Couturier and D. Mba, 'Operational bearing parameters and acoustic emission generation', *Journal of Vibration and Acoustics, Transactions of the ASME*, vol. 130, pp. 1–5, 2008. DOI: 10.1115/1.2776339.

[65]   D. Cornel, F. G. Guzmán, G. J. and S. Neumann, 'Acoustic response of roller bearings under critical operating conditions', *Lecture Notes in Mechanical Engineering*, pp. 740–749, 2020. DOI: 10.1007/978-3-030-48021-9_82.

[66]   Z. Rahman, H. Ohba, T. Yoshioka and T. Yamamoto, 'Incipient damage detection and its propagation monitoring of rolling contact fatigue by acoustic emission', *Tribology International*, vol. 42, pp. 807–815, 2009. DOI: 10.1016/j.triboint.2008.10.014.

[67]   P. D. McFadden and J. D. Smith, 'Acoustic emission transducers for the vibration monitoring of bearings at low speeds', *Proceedings of the Institution of Mechanical Engineers, Part C: Journal of Mechanical Engineering Science*, vol. 198, pp. 127–130, 1984. DOI: 10.1243/PIME_PROC_1984_198_097_02.

[68]   N. Jamaludin, D. Mba and R. H. Bannister, 'Condition monitoring of slow-speed rolling element bearings using stress waves', *Proceedings of the Institution of Mechanical Engineers, Part E: Journal of Process Mechanical Engineering*, vol. 215, pp. 245–271, 2001. DOI: 10.1243/0954408011530488.

[69]   M. Žvokelj, S. Zupan and I. Prebil, 'Multivariate and multiscale monitoring of large-size low-speed bearings using ensemble empirical mode decomposition method combined with principal component analysis', *Mechanical Systems and Signal Processing*, vol. 24, pp. 1049–1067, 2010. DOI: 10.1016/j.ymssp.2009.09.002.

[70]   G. Li, Y. Jiao and Z. Wu, 'Defect diagnosis of low-speed heavy-duty bearings using acoustic emission', *Springer Proceedings in Physics*, vol. 218, pp. 249–257, 2017. DOI: 10.1007/978-3-030-12111-2_23.

[71]   C. Chen, C. Sun, Y. Zhang and N. Wang, 'Fault diagnosis for large-scale wind turbine rolling bearing using stress wave and wavelet analysis', vol. 3, 2005, pp. 2239–2244. DOI: 10.1109/icems.2005.202966.

[72]   A. Widodo, E. Y. Kim, J. D. Son, B. S. Yang, A. C. C. Tan, D. S. Gu, B. K. Choi and J. Mathew, 'Fault diagnosis of low speed bearing based on relevance vector machine and support vector machine', *Expert Systems with Applications*, vol. 36, pp. 7252–7261, 2009. DOI: 10.1016/J.ESWA.2008.09.033.

[73]   A. Widodo, B. Yang, E. Y. Kim, A. C. C. Tan and J. Mathew, 'Fault diagnosis of low speed bearing based on acoustic emission signal and multi-class relevance vector machine', *Nondestructive Testing and Evaluation*, vol. 24, pp. 313–328, 2009. DOI: 10.1080/10589750802378974.

[74] R. Fuentes, R. S. Dwyer-Joyce, M. B. Marshall, J. Wheals and E. J. Cross, 'Detection of sub-surface damage in wind turbine bearings using acoustic emissions and probabilistic modelling', *Renewable Energy*, vol. 147, pp. 776–797, 2020. DOI: 10.1016/J.RENENE.2019.08.019.

[75] M. W. Hawman and W. S. Galinaitis, 'Acoustic emission monitoring of rolling element bearings', *Ultrasonics Symposium Proceedings*, vol. 2, pp. 885–889, 1988. DOI: 10.1109/ultsym.1988.49503.

[76] J. Shiroishi, Y. Li, S. Liang, T. Kurfess and S. Danyluk, 'Bearing condition diagnostics via vibration and acoustic emission measurements', *Mechanical Systems and Signal Processing*, vol. 11, pp. 693–705, 1997. DOI: 10.1006/mssp.1997.0113.

[77] N. W. Nirwan and H. B. Ramani, 'Condition monitoring and fault detection in roller bearing used in rolling mill by acoustic emission and vibration analysis', *Materials Today: Proceedings*, vol. 51, pp. 344–354, 2022. DOI: 10.1016/J.MATPR.2021.05.447.

[78] C. J. Li and S. Y. Li, 'Acoustic emission analysis for bearing condition monitoring', *Wear*, vol. 185, pp. 67–74, 1995. DOI: 10.1016/0043-1648(95)06591-1.

[79] K. R. Al-Balushi, A. Addali, B. Charnley and D. Mba, 'Energy index technique for detection of acoustic emissions associated with incipient bearing failures', *Applied Acoustics*, vol. 71, pp. 812–821, 2010. DOI: 10.1016/j.apacoust.2010.04.006.

[80] B. Kilundu, X. Chiementin, J. Duez and D. Mba, 'Cyclostationarity of acoustic emissions (ae) for monitoring bearing defects', *Mechanical Systems and Signal Processing*, vol. 25, pp. 2061–2072, 2011. DOI: 10.1016/j.ymssp.2011.01.020.

[81] C. Ruiz-Cárcel, E. Hernani-Ros, Y. Cao and D. Mba, 'Use of spectral kurtosis for improving signal to noise ratio of acoustic emission signal from defective bearings', *Journal of Failure Analysis and Prevention*, vol. 14, pp. 363–371, 2014. DOI: 10.1007/s11668-014-9805-7.

[82] X. Chiementin, D. Mba, B. Charnley, S. Lignon and J. P. Dron, 'Effect of the denoising on acoustic emission signals', *Journal of Vibration and Acoustics, Transactions of the ASME*, vol. 132, pp. 0 310 091–0 310 099, 2010. DOI: 10.1115/1.4000789.

[83] F. Elasha, C. Ruiz-Carcel, D. Mba and P. Chandra, 'A comparative study of the effectiveness of adaptive filter algorithms, spectral kurtosis and linear prediction in detection of a naturally degraded bearing in a gearbox', *Journal of Failure Analysis and Prevention*, vol. 14, pp. 623–636, 2014. DOI: 10.1007/s11668-014-9857-8.

[84] F. Elasha, M. Greaves, D. Mba and A. Addali, 'Application of acoustic emission in diagnostic of bearing faults within a helicopter gearbox', vol. 38, 2015, pp. 30–36. DOI: 10.1016/j.procir.2015.08.042.

[85] F. Elasha, D. Mba and C. Ruiz-Carcel, 'A comparative study of adaptive filters in detecting a naturally degraded bearing within a gearbox', *Case Studies in Mechanical Systems and Signal Processing*, vol. 3, pp. 1–8, 2016. DOI: 10.1016/j.csmssp.2015.11.001.

[86]   J. L. F. Chacon, V. Kappatos, W. Balachandran and T. H. Gan, 'A novel approach for incipient defect detection in rolling bearings using acoustic emission technique', *Applied Acoustics*, vol. 89, pp. 88–100, 2015. DOI: `10.1016/j.apacoust.2014.09.002`.

[87]   F. Hemmati, W. Orfali and M. S. Gadala, 'Roller bearing acoustic signature extraction by wavelet packet transform, applications in fault detection and size estimation', *Applied Acoustics*, vol. 104, pp. 101–118, 2016. DOI: `10.1016/j.apacoust.2015.11.003`.

[88]   A. A. Azeez, M. Alkhedher, M. S. Gadala and O. A. Mohamad, 'Fault detection of rolling element bearings using advanced signal processing technique', *2020 Advances in Science and Engineering Technology International Conferences, ASET 2020*, 2020. DOI: `10.1109/ASET48392.2020.9118398`.

[89]   M. T. Pham, J. Kim and C. H. Kim, 'Efficient fault diagnosis of rolling bearings using neural network architecture search and sharing weights', *IEEE Access*, vol. 9, pp. 98 800–98 811, 2021. DOI: `10.1109/ACCESS.2021.3096036`.

[90]   M. T. Pham, J. M. Kim and C. H. Kim, 'Intelligent fault diagnosis method using acoustic emission signals for bearings under complex working conditions', *Applied Sciences 2020, Vol. 10, Page 7068*, vol. 10, p. 7068, 2020. DOI: `10.3390/APP10207068`.

[91]   L. Tang, X. Liu, X. Wu, Z. Wang and K. Hou, 'Defect localization on rolling element bearing stationary outer race with acoustic emission technology', *Applied Acoustics*, vol. 182, p. 108 207, 2021. DOI: `10.1016/J.APACOUST.2021.108207`.

[92]   C. W. Fei, Y. S. Choy, G. C. Bai and W. Z. Tang, 'Multi-feature entropy distance approach with vibration and acoustic emission signals for process feature recognition of rolling element bearing faults', *Structural Health Monitoring*, vol. 17, pp. 156–168, 2018. DOI: `10.1177/1475921716687167`.

[93]   N. Tandon and B. C. Nakra, 'Defect detection in rolling element bearings by acoustic emission method', *Journal of acoustic emission*, vol. 9, pp. 25–28, 1990.

[94]   N. Tandon and B. C. Nakra, 'Comparison of vibration and acoustic measurement techniques for the condition monitoring of rolling element bearings', *Tribology International*, vol. 25, pp. 205–212, 1992. DOI: `10.1016/0301-679X(92)90050-W`.

[95]   A. Morhain and D. Mba, 'Bearing defect diagnosis and acoustic emission', *Proceedings of the Institution of Mechanical Engineers, Part J: Journal of Engineering Tribology*, vol. 217, pp. 257–272, 2003. DOI: `10.1243/135065003768618614`.

[96]   Y. He, X. Zhang and M. I. Friswell, 'Defect diagnosis for rolling element bearings using acoustic emission', *Journal of Vibration and Acoustics, Transactions of the ASME*, vol. 131, pp. 0 610 121–06 101 210, 2009. DOI: `10.1115/1.4000480`.

[97]   A. M. Al-Ghamdi, P. Cole, R. Such and D. Mba, 'Estimation of bearing defect size with acoustic emission', *Insight - Non-Destructive Testing and Condition Monitoring*, vol. 46, pp. 758–761, 2004. DOI: `10.1784/insi.46.12.758.54491`.

[98] N. Tandon, G. S. Yadava and K. M. Ramakrishna, 'A comparison of some condition monitoring techniques for the detection of defect in induction motor ball bearings', *Mechanical Systems and Signal Processing*, vol. 21, pp. 244–256, 2007. DOI: `10.1016/J.YMSSP.2005.08.005`.

[99] D. Mba, 'The use of acoustic emission for estimation of bearing defect size', *Journal of Failure Analysis and Prevention*, vol. 8, pp. 188–192, 2008. DOI: `10.1007/s11668-008-9119-8`.

[100] S. Al-Dossary, R. I. R. Hamzah and D. Mba, 'Observations of changes in acoustic emission waveform for varying seeded defect sizes in a rolling element bearing', *Applied Acoustics*, vol. 70, pp. 58–81, 2009. DOI: `10.1016/j.apacoust.2008.01.005`.

[101] A. Choudhury and N. Tandon, 'Application of acoustic emission technique for the detection of defects in rolling element bearings', *Tribology International*, vol. 33, pp. 39–45, 2000. DOI: `10.1016/S0301-679X(00)00012-8`.

[102] F. Hemmati, M. Miraskari and M. S. Gadala, 'Application of wavelet packet transform in roller bearing fault detection and life estimation', *Journal of Physics: Conference Series*, vol. 1074, p. 012 142, 2018. DOI: `10.1088/1742-6596/1074/1/012142`.

[103] A. M. Al-Ghamd and D. Mba, 'A comparative experimental study on the use of acoustic emission and vibration analysis for bearing defect identification and estimation of defect size', *Mechanical Systems and Signal Processing*, vol. 20, pp. 1537–1571, 2006. DOI: `10.1016/j.ymssp.2004.10.013`.

[104] J. Miettinen and P. Andersson, 'Acoustic emission of rolling bearings lubricated with contaminated grease', *Tribology International*, vol. 33, pp. 777–787, 2000. DOI: `10.1016/S0301-679X(00)00124-9`.

[105] K. A. I. Sheriff, V. Hariharan and T. Kannan, 'Analysis of solid contamination in ball bearing through acoustic emission signals', *Archives of Metallurgy and Materials*, vol. 62, pp. 1871–1874, 2017. DOI: `10.1515/amm-2017-0283`.

[106] S. Poddar and N. Tandon, 'Detection of particle contamination in journal bearing using acoustic emission and vibration monitoring techniques', *Tribology International*, vol. 134, pp. 154–164, 2019. DOI: `10.1016/j.triboint.2019.01.050`.

[107] K. Jiang, L. Han and Y. Zhou, 'Quantitative evaluation of the impurity content of grease for low-speed heavy-duty bearing using an acoustic emission technique', *Measurement and Control (United Kingdom)*, vol. 52, pp. 1159–1166, 2019. DOI: `10.1177/0020294019858214`.

[108] S. M. del Campo, S. Schnabel, F. Sandin and P. Marklund, 'Detection of particle contaminants in rolling element bearings with unsupervised acoustic emission feature learning', *Tribology International*, vol. 132, pp. 30–38, 2019. DOI: `10.1016/J.TRIBOINT.2018.12.007`.

[109] F. König, C. Sous, A. O. Chaib and G. Jacobs, 'Machine learning based anomaly detection and classification of acoustic emission events for wear monitoring in sliding bearing systems', *Tribology International*, vol. 155, 2021. DOI: `10.1016/j.triboint.2020.106811`.

[110] B. Scheeren, M. L. Kaminski and L. Pahlavan, 'Evaluation of ultrasonic stress wave transmission in cylindrical roller bearings for acoustic emission condition monitoring', *Sensors*, vol. 22, p. 1500, 2022. DOI: `10.3390/S22041500`.

[111] A. J. Berkhout, *Seismic migration: Imaging of acoustic energy by wave field extrapolation / A., Theoretical aspects*. Elsevier Scientific Pub. Co., 1980.

[112] L. Pahlavan, M. M. Mota and G. Blacquière, 'Influence of asphalt on fatigue crack monitoring in steel bridge decks using guided waves', *Construction and Building Materials*, vol. 120, pp. 593–604, 2016. DOI: `10.1016/j.conbuildmat.2016.05.138`.

[113] L. Pahlavan and G. Blacquière, 'Fatigue crack sizing in steel bridge decks using ultrasonic guided waves', *NDT and E International*, vol. 77, pp. 49–62, 2016. DOI: `10.1016/j.ndteint.2015.09.006`.

[114] ASTM International, *Standard guide for determining the reproducibility of acoustic emission sensor response*, E976-15, West Conshohocken, PA, USA, 2015. DOI: `10.1520/E0976-15`.

[115] J. M. Lilly and S. C. Olhede, 'Higher-order properties of analytic wavelets', *IEEE Transactions on Signal Processing*, vol. 57, pp. 146–160, 2009. DOI: `10.1109/TSP.2008.2007607`.

[116] J. M. Lilly and S. C. Olhede, 'On the analytic wavelet transform', *IEEE Transactions on Information Theory*, vol. 56, pp. 4135–4156, 2010. DOI: `10.1109/TIT.2010.2050935`.

[117] J. M. Lilly and S. C. Olhede, 'Generalized morse wavelets as a superfamily of analytic wavelets', *IEEE Transactions on Signal Processing*, vol. 60, pp. 6036–6041, 2012. DOI: `10.1109/TSP.2012.2210890`.

[118] J. M. Lilly, 'Element analysis: A wavelet-based method for analysing time-localized events in noisy time series', *Proceedings of the Royal Society A: Mathematical, Physical and Engineering Sciences*, vol. 473, p. 20160776, 2017. DOI: `10.1098/rspa.2016.0776`.

[119] B. Scheeren, M. L. Kaminski and L. Pahlavan, 'Acoustic emission monitoring of naturally developed damage in large-scale low-speed roller bearings', *Structural Health Monitoring*, vol. OnlineFirst, 2023. DOI: `10.1177/14759217231164912`.

[120] A. K. Jain, M. N. Murty and P. J. Flynn, 'Data clustering', *ACM Computing Surveys (CSUR)*, vol. 31, pp. 264–323, 1999. DOI: `10.1145/331499.331504`.

[121] E. Pomponi and A. Vinogradov, 'A real-time approach to acoustic emission clustering', *Mechanical Systems and Signal Processing*, vol. 40, pp. 791–804, 2013. DOI: `10.1016/J.YMSSP.2013.03.017`.

[122] Z. Li, J. G. Lee, X. Li and J. Han, 'Incremental clustering for trajectories', *Lecture Notes in Computer Science (including subseries Lecture Notes in Artificial Intelligence and Lecture Notes in Bioinformatics)*, vol. 5982 LNCS, pp. 32–46, 2010. DOI: `10.1007/978-3-642-12098-5_3`.

[123] J. Allan, R. Papka and V. Lavrenko, 'On-line new event detection and tracking', *SIGIR Forum (ACM Special Interest Group on Information Retrieval)*, pp. 37–45, 1998. DOI: `10.1145/290941.290954`.

[124] B. Scheeren and L. Pahlavan, 'Condition assessment of low-speed slew bearings in offshore applications using acoustic emission monitoring', P. Rizzo and A. Milazzo, Eds., ser. European Workshop on Structural Health Monitoring. EWSHM 2022. Lecture Notes in Civil Engineering, vol 270. Springer, Cham, 2023, pp. 892–901. DOI: 10.1007/978-3-031-07322-9_90.

[125] B. Scheeren and L. Pahlavan, *Monitoring integrity of low-speed bearings using acoustic emission*, The Netherlands Patent N2032270, 2023. (pending).

[126] R. B. Randall and J. Antoni, 'Rolling element bearing diagnostics—a tutorial', *Mechanical Systems and Signal Processing*, vol. 25, pp. 485–520, 2011. DOI: 10.1016/j.ymssp.2010.07.017.

[127] R. B. Randall, J. Antoni and S. Chobsaard, 'The relationship between spectral correlation and envelope analysis in the diagnostics of bearing faults and other cyclostationary machine signals', *Mechanical Systems and Signal Processing*, vol. 15, pp. 945–962, 2001. DOI: 10.1006/mssp.2001.1415.

[128] F. J. Richards, 'A flexible growth function for empirical use', *Journal of Experimental Botany*, vol. 10, pp. 290–301, 1959. DOI: 10.1093/JXB/10.2.290.

[129] B. Scheeren, A. Huijer, F. Riccioli, N. Thakoerdajal and L. Pahlavan, 'Hiteam - report phase 2', Delft University of Technology, 2021.

[130] N. Thakoerdajal, *Damage assessment of highly-loaded low-speed roller bearings with acoustic emission monitoring*, Master Thesis, Delft University of Technology, 2022.

[131] International Organization for Standardization, *Rolling bearings — dynamic load ratings and rating life*, ISO 281:2007, Geneva, CH, 2007.

[132] A. T. Patera, 'A spectral element method for fluid dynamics: Laminar flow in a channel expansion', *Journal of Computational Physics*, vol. 54, pp. 468–488, 1984. DOI: 10.1016/0021-9991(84)90128-1.

[133] L. C. Young, 'A finite-element method for reservoir simulation', *Society of Petroleum Engineers Journal*, vol. 21, pp. 115–128, 1981. DOI: 10.2118/7413-PA.

[134] D. Komatitsch and J. Tromp, 'Introduction to the spectral element method for three-dimensional seismic wave propagation', *Geophysical Journal International*, vol. 139, pp. 806–822, 1999. DOI: 10.1046/J.1365-246X.1999.00967.X.

[135] D. Komatitsch, C. Barnes and J. Tromp, 'Simulation of anisotropic wave propagation based upon a spectral element method', *Geophysics*, vol. 65, pp. 1251–1260, 2000. DOI: 10.1190/1.1444816.

[136] D. Komatitsch, C. Barnes and J. Tromp, 'Wave propagation near a fluid-solid interface: A spectral-element approach', *GEOPHYSICS*, vol. 65, pp. 623–631, 2012. DOI: 10.1190/1.1444758.

[137] B. Scheeren, L. Pahlavan and M. L. Kaminski, 'Condition assessment of highly-loaded low-speed bearings using acoustic emission monitoring: A feasibility study', T. Shiotani, Y. Mizutani and H. Yuki, Eds., ser. Progress in Acoustic Emission XIX, The Japanese Society for Non-Destructive Inspection, 2018, pp. 239–244.

PUBLICATIONS

Journal articles
• *As part of this thesis:*

(1). B. Scheeren, M. L. Kaminski and L. Pahlavan, 'Evaluation of ultrasonic stress wave transmission in cylindrical roller bearings for acoustic emission condition monitoring', *Sensors*, vol. 22, p. 1500, 2022. DOI: 10.3390/S22041500

(2). B. Scheeren, M. L. Kaminski and L. Pahlavan, 'Acoustic emission monitoring of naturally developed damage in large-scale low-speed roller bearings', *Structural Health Monitoring*, vol. OnlineFirst, 2023. DOI: 10.1177/14759217231164912

Patents
• *As part of this thesis:*

(1). B. Scheeren and L. Pahlavan, *Monitoring integrity of low-speed bearings using acoustic emission*, The Netherlands Patent N2032270, 2023. (pending)

Conferences attended with papers

(1). B. Scheeren, L. Pahlavan and M. L. Kaminski, 'Condition assessment of highly-loaded low-speed bearings using acoustic emission monitoring: A feasibility study', T. Shiotani, Y. Mizutani and H. Yuki, Eds., ser. Progress in Acoustic Emission XIX, The Japanese Society for Non-Destructive Inspection, 2018, pp. 239–244

(2). B. Scheeren and L. Pahlavan, 'Condition assessment of low-speed slew bearings in offshore applications using acoustic emission monitoring', P. Rizzo and A. Milazzo, Eds., ser. European Workshop on Structural Health Monitoring. EWSHM 2022. Lecture Notes in Civil Engineering, vol 270. Springer, Cham, 2023, pp. 892–901. DOI: 10.1007/978-3-031-07322-9_90

ACKNOWLEDGMENTS

This book marks the completion of a voyage that I started over six years ago, five of which as a PhD candidate. All of these years I benefited from the support of those around me, for that I extend my greatest gratitude.

To my promotor, Mirek Kaminski, who started it all by just asking me whether I wanted to do a PhD. For his trust in my ability, for defining this programme together, and for continuing in his retirement to get me to this defence.

To my copromotor, Pooria Pahlavan, who supervised my development in these five years. For our agreements and disagreements, for his advice and critique, and for setting up our structural health monitoring group wherein we thrive.

To my paranymph, Sepideh Zarrinkelk, who was and is always available. For letting me sit the cats, for cooking, and for an octopus.

To my project partners, all those who were involved from Allseas Engineering, Bluewater Energy Services, Heerema Marine Contractors, Huisman Equipment, SBM Offshore, SOFEC, and TotalEnergies, who made this programme possible. For sharing your expertise, for the opportunities to run experiments, and for continuing in the further development of our ideas.

To my dearest friends. For the trips we went on, for the food and drinks we shared, and for keeping me sane.

To my family. For their love, and for their interest.

To my colleagues, both current and former, in particular those that may be called friends. For the endless discussions whether they made sense or not, for understanding, and for eating cake.

To those that stood against me in fencing, or besides me in bouldering. For pushing me towards challenges, for clearing my mind, and for strengthening my body.

I thank all of you.

Bart Scheeren
Voorburg, May 2023

CURRICULUM VITAE

Bart Scheeren was born in Wijchen on October 25, 1992. He attended Maaswaal College in Wijchen from 2005 until 2011. He obtained his Bachelor (with honours) and Master of Science (with distinction) in Marine Technology at Delft University of Technology in 2014 and 2017 respectively. His Master's program included a four-month research visit to Vallen Systeme in Munich, Germany. He performed his master thesis research jointly at Vallen Systeme in Munich and at Delft University of Technology, resulting in the thesis entitled "On the Development of a Volumetric Acoustic Emission Fatigue Crack Monitoring System."

From 2018 to 2023 he performed his PhD research under the supervision of Pooria Pahlavan and Mirek Kaminski on acoustic emission condition monitoring of highly-loaded low-speed roller bearings. The results of his PhD research are included in this dissertation.